DYNAMICS OF MILLING FLEXIBLE STRUCTURES

By

Marc Lorenzo Campomanes

B.Sc. The University of Manitoba, 1993

A THESIS SUBMITTED IN PARTIAL FULFILLMENT OF
THE REQUIREMENTS FOR THE DEGREE OF

MASTER OF APPLIED SCIENCE

in

The Faculty of Graduate Studies

Department of Mechanical Engineering

We accept this thesis as conforming
to the required standard

THE UNIVERSITY OF BRITISH COLUMBIA

September, 1998

In presenting this thesis in partial fulfilment of the requirements for an advanced degree at the University of British Columbia, I agree that the Library shall make it freely available for reference and study. I further agree that permission for extensive copying of this thesis for scholarly purposes may be granted by the head of my department or by his or her representatives. It is understood that copying or publication of this thesis for financial gain shall not be allowed without my written permission.

Department of Mechanical Engineering

The University of British Columbia
Vancouver, Canada

Date 21 Sept. /98

DE-6 (2/88)

Abstract

Peripheral milling of aerospace parts takes a considerable amount of manufacturing time on production floors. Recently, due to fatigue constraints and advances in high speed machining, aircraft components are machined as monolithic parts from solid blanks. This thesis focuses on the mathematical modeling of peripheral milling of aerospace parts with thin walls.

The varying dynamics along the contact length of both the part and the cutter are considered. The structural dynamics of a flexible thin web and of the end mill are modelled as discrete models, whose modal parameters are identified experimentally. The kinematics of peripheral milling is modelled in the time domain. The chip removed at any point along the workpiece/cutter contact length is predicted, including the influence of structural dynamic displacements of both the cutter and the workpiece at present and previous tooth passing intervals. The cutting forces are predicted as being proportional to the time varying dynamic chip loads. The time domain model of the process includes various non-linearities in the process such as the separation of the tool from the workpiece due to excessive vibrations. The time domain algorithm can predict the cutting load distribution on both cutter and thin web structures, dimensional surface finish of the part, vibrations, torque, power and bending load experienced by the lower spindle bearing of the machine tool. The predictions are verified experimentally by conducting numerous cutting tests.

The accurate time domain simulations of dynamic milling have shown that large feed rates affect the chatter stability at low cutting speeds. This phenomenon has not been previously reported in the literature. An analytical model of the dynamic milling system with the influence of feed on the regenerative phase shift has been developed, and the stability of the system is solved analytically in the frequency domain. The developed time domain simulations of the process support the linear analytical solution.

The mathematical models and algorithms developed in this thesis have been experimentally verified and have been used in peripheral milling of aircraft wing components in industry.

Table of Contents

List of Figures

List of Tables

Acknowledgements

I wish to express my sincere appreciation to my research advisor, Dr. Yusuf Altintas, for his support, guidance, and encouragement throughout my studies at the University of British Columbia. I would like to thank my colleagues in the Manufacturing Automation Laboratory at UBC for their assistance and patience.

I also wish to thank Jan Jeppsson and David Bernhard from the Boeing Commercial Airplane Group and Richard Hom from the Boeing Defense & Space Group for their valuable feedback and for providing practical applications for this research.

This research has been funded by the Natural Sciences and Engineering Research Council and the British Columbia Advanced Systems Institute.

Finally, I wish to extend a special thanks to my friends, family, and colleagues who have made my two years at UBC most memorable. I dedicate this work to them.

CHAPTER 1 *Introduction*

Peripheral milling, being one of the most versatile manufacturing processes, is a very common operation in manufacturing aircraft components. The geometrical complexity and high quality requirements of structures such as wings, fuselage sections, and jet engine components often requires that parts be machined from a single workpiece, resulting in large amounts of excess material removal. Many of these structures have deep pockets and flexible webs which must be machined with long slender endmills. Furthermore, these components usually have tight dimensional tolerances which must be met during machining. These factors have motivated research in milling for decades, in order to optimize metal removal rates, while maintaining strict dimensional tolerances.

This thesis outlines the theory and mathematical models used in the development of a computer algorithm which can be a useful tool in determining optimum milling conditions. In industry, power restrictions, cutting force limits, and strict surface tolerances often lead to machining using very conservative metal removal rates. With the milling models developed in this thesis, cutting forces, finished surface profiles, spindle power requirements, bending moment on spindle bearings, and axial depth of cut limits can be predicted to help select the cutting conditions which result in highest productivity, while keeping within required tolerances and within physical limitations of the machine tool. More specifically, this thesis

focuses on milling of flexible workpiece structures with flexible helical endmills, emphasizing on cuts with large depths of cut and small widths of cut. Under these conditions, the modelling of exact milling kinematics and of varying dynamics along the axial depth of cut become of increasing importance.

First, a review of existing research in the milling of flexible structures is given in Chapter 2. An overview of milling kinematics, modelling of cutting forces, chatter stability limits, and time domain simulations are discussed, which provide the basis for some of the approaches used in the milling model used in this thesis.

In Chapter 3, the dynamic model used to simulate the vibratory motion of the cutting tool and of the flexible workpiece is discussed. Many existing simulations use simplified lumped dynamics, which may not provide accurate enough results when machining at large depths of cut with flexible workpieces and/or flexible cutters. Alternatively, more complicated models have usually been derived from finite element methods, which can often require a significant effort for more complex workpieces. The more practical approach taken in this thesis relies on experimental transfer function measurements at multiple points on the workpiece and on the cutter. A modal analysis model and computer program are developed to efficiently identify dynamic parameters of the workpiece and cutting tool for use in the milling simulation.

Milling mechanics are described in Chapter 4. Material removal, uncut chip thickness calculations, and predicted cutting forces are discussed. Most existing models use approximations for uncut chip thickness. This thesis uses a discretized cutter and workpiece model to more accurately simulate the milling process. This is particularly significant under conditions of large forced and self-excited vibrations. This digitized model also allows prediction of surface error profile and surface roughness. Experimental cutting tests verify the validity of the model.

In machining, self-excited vibrations can cause poor surface finish and excessively large cutting forces which can damage the workpiece, the cutting tool, and in extreme cases, the machine spindle. This unstable condition, known as *chatter*, is discussed in Chapter 5.

Chatter stability is often presented in the form of *stability lobes*. Two approaches to calculating stability lobes are described here. The first uses time domain simulations to predict cutting forces. Maximum predicted dynamic chip thickness is used for determining stability. The simulations are repeated for various cutting conditions until the stability limit is found.

In practice, there is a general trend for stability to increase with decreasing spindle speed. Traditionally, this trend has been attributed to *process damping*, which is caused by flank edge contact with the workpiece. Modelling of process damping is not in the scope of this thesis since it typically requires extensive experimentation and sophisticated equipment. However, even without including process damping effects, similar trends were noticed in the stability lobes from time domain simulations. This motivated the development of a second, frequency domain model, to support the findings. This newly reported phenomenon results from including the effect of feed rate in the *regeneration effect* which causes chatter. This claim is supported by results showing close agreement between the time domain and frequency domain chatter stability lobe models.

In Chapter 6, the results of some experimental cutting tests are presented and discussed. Cutting forces, workpiece vibrations, and stability limit models described in this thesis are well verified. Some predicted trends, such as the increased stability at low spindle speeds due to feed were difficult to support with experimental cutting tests due to the absence of process damping in the simulation model. Generally, there was excellent agreement between predicted and measured results.

The thesis is concluded with a brief summary of contributions and of recommendations for future research.

CHAPTER 2

Literature Review

2.1 Overview

In this chapter, a literature review is presented of research in milling which pertains to this thesis. Kinematics of milling is first discussed, which includes models of cutter motion and chip thickness. Next, a brief summary of milling force models is given, followed by the development of chatter theory and chatter stability borders in milling. Finally, previous milling simulation research is presented which focused on milling of flexible structures.

2.2 Kinematics of Milling

Unlike the steady state turning operation in which chip thickness is constant, milling is an intermittent multi-point cutting operation which involves feeding the workpiece into a rotating cutter. The milling operation can generally be divided into two categories: peripheral and face milling. In peripheral milling, which is the focus of this thesis, the cut surface is parallel to the axis of the cutting tool. In face milling, the working surface is perpendicular to the cutting tool.

Milling can also be categorized into two main orientations, shown in Figure (2-1). Milling in which the cutter rotates in a direction against the feed of the workpiece is known as con-

ventional or up-milling. The orientation in which the workpiece is fed in the direction of the cutter rotation is known as climb milling or down milling. Mathematical and practical differences between these two orientations are discussed by Martellotti in [1].

FIGURE 2-1: Upmilling and Downmilling

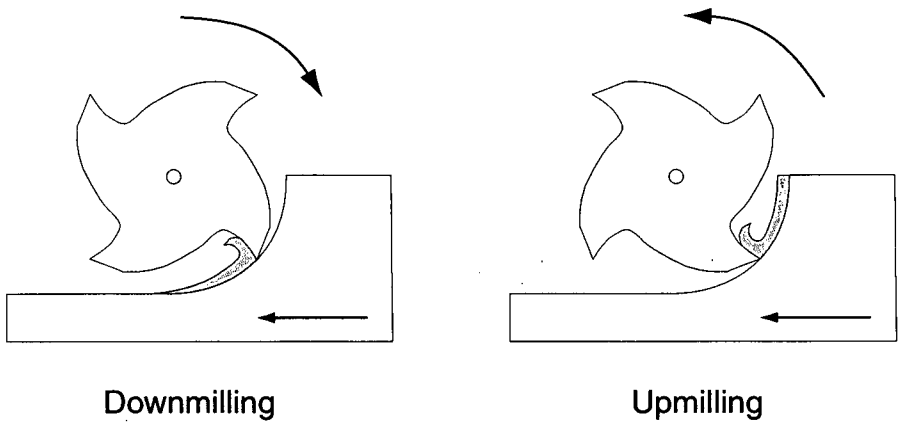

The milling cutter can consist of multiple either integrated or inserted teeth, uniformly or non-uniformly distributed, with various geometries and configurations. The complex motion of the rotating cutting tooth relative to a translating workpiece is well described by Martellotti [2]. He gives precise mathematical formulations of the tooth path, described as trochoidal, instantaneous chip thickness, and feed marks left on the finished surface. Martellotti also confirms that in most practical applications, in which the radius of the cutter is much greater that the feed per tooth, instantaneous chip thickness, $h(\phi)$ can be approximated as the traditionally used relation:

$$h(\phi) = s_t \sin\phi \tag{2-1}$$

where ϕ is the immersion angle of the tooth and s_t is the feed per tooth.

This sinusoidal approximation of chip load is almost exclusively used in the literature in the calculation of cutting forces. Montgomery, Altintas, and Lee [3] [4] use computer simulations which digitize the cutter edge and workpiece surface to trace the exact trochoidal motion of each discretized cutting point. Under many practical conditions, exact chip thickness calculations offer little improvement over the sinusoidal approximation in predicting static cutting forces. The advantages of the digitized surface approach lies in the prediction of chatter during vibratory milling, discussed in later sections.

2.3 Modelling of Milling Forces

Due to the complexity of milling mechanics and the large number of variables involved in modelling the milling process, numerous force models have been developed. These models can be classified into two categories: *mechanistic* and *mechanics of milling*. In *mechanistic* models, force coefficients are experimentally estimated for a specific cutter geometry and workpiece material, relating force to uncut chip thickness, chip width, and other variables. In the *mechanics of milling* approach, the milling coefficients are calculated as a function of shear stress, shear angle, friction angle, and cutter geometry from orthogonal cutting tests. The mechanistic model is presented below, while the mechanics of milling force model is not used in this thesis and will not be discussed.

The most primitive, yet still popular models are based on the relationship between metal removal rate and average consumed power, through which average tangential force may be estimated [5]. Expressions for the pulsating cutting forces in milling were first developed by Sawin [6] and Salomon [7]. Through purely geometrical considerations, a relationship is formed between work done with a straight tooth cutter, based on an assumption that specific cutting pressure varies as an exponential function of chip thickness. Tangential force is calculated as:

$$F_t = K_s a h \tag{2-2}$$

where a is the chip width, h is the instantaneous chip thickness, and K_s is the cutting pressure as a function of chip thickness and two experimentally determined coefficients C and x:

$$K_s = Ch^x \tag{2-3}$$

Sabberwal [8] and Koenigsberger [9] extend this model to predict cutting forces with non-zero helix cutters.

Another approach, which has become widely used, involves use of an average cutting pressure coefficient and a constant edge force coefficient [10]. With further contributions from Tlusty and McNeil [11], Kline et al. [12] [13], Sutherland and DeVor [14], and Montgomery and Altintas [3], this model is fully developed into a practical formulation by Budak et al. [15] to model tangential, radial, and axial forces, F_t, F_r, and F_a in the form:

$$\begin{aligned} F_t &= K_{te}a + K_{tc}ah \\ F_r &= K_{re}a + K_{rc}ah \\ F_a &= K_{ae}a + K_{ac}ah \end{aligned} \tag{2-4}$$

where K_{te}, K_{tc}, K_{re}, K_{rc}, K_{ae}, and K_{ac} are force coefficients determined from measured average cutting forces in X, Y, and Z directions at varying feed rates. This model is used in this thesis for evaluation of cutting forces due to the minimal measurements required and proven accuracy. It is discussed in detail in Chapter 4.

2.4 Chatter and Stability Analysis

Due to the periodic nature of cutting forces in milling, vibrations in the machine tool and workpiece structures are unavoidable. If some of the harmonic components of cutting forces are in resonance with natural frequencies of the cutter-workpiece system, forced vibrations can become significant in determining the quality of surface finish. In most circumstances, however, it is not the forced vibrations which are most significant. Rather, it is an unstable condition, known as chatter, that frequently arises in metal cutting, which dominates cutting forces and vibrations. Under these self-excited conditions, energy builds in the system with vibrations and cutting forces growing to unacceptable levels, until the tool separates from the workpiece.

Many factors contribute to determining whether or not chatter will occur, including the structural characteristics of the machine and cutter, structural characteristics of the workpiece, workpiece material properties, feed rate (chip thickness), cutting speed (spindle speed), axial depth of cut (chip width), radial width of cut (immersion), and cutter geometry. With the dynamic characteristics of the machine and workpiece often fixed, the depth of cut, or chip width, has the most significant influence. At sufficiently small chip width, there is no chatter, while there is a sufficiently large chip width at which chatter will always occur. The chip width limit where chatter begins to occur is often plotted against spindle speed to give the *chatter stability lobes*, a well known representation of the boundary between stable and unstable cutting. Models for determining this stability limit are discussed in a later section.

2.4.1 Theory of Self-Excited Chatter Vibrations

2.4.1.1 Regeneration of Waviness

The theory of chatter in metal cutting was well developed through the 1950's and 1960's. Tobias [16] and Tlusty [17] were among the few early researchers in the area of dynamic cutting. It is well documented that the primary cause of chatter under most machining conditions is a phenomenon known as the *regeneration effect* [18] [19]. Even when forced vibrations are extremely small, the slightest waviness left on the cutting surface cause periodic variations in chip thickness for following teeth. Pass after pass, the vibrations may be sustained through this "regeneration of waviness" on the surface. In a "stable" case, initial vibrations diminish in subsequent passes, in an "unstable" case (chatter), vibrations increase, and in the critically stable case, the magnitude of vibration remains constant.

Consider the milling operation in Figure (2-2). The combination of the waviness on the surface left by the previous tooth and the vibration of the currently cutting tooth create the perodically changing chip thickness. Figure (2-3) shows how the severity of variation in the chip thickness depends on the phase shift ε between the undulations of successive tooth paths. Figure (2-3a) shows that a zero phase shift produces a constant chip thickness despite any disturbances in the system. Figures (2-3b) and (2-3c) demonstrate the varying chip load

FIGURE 2-2: Regeneration of Waviness in Milling

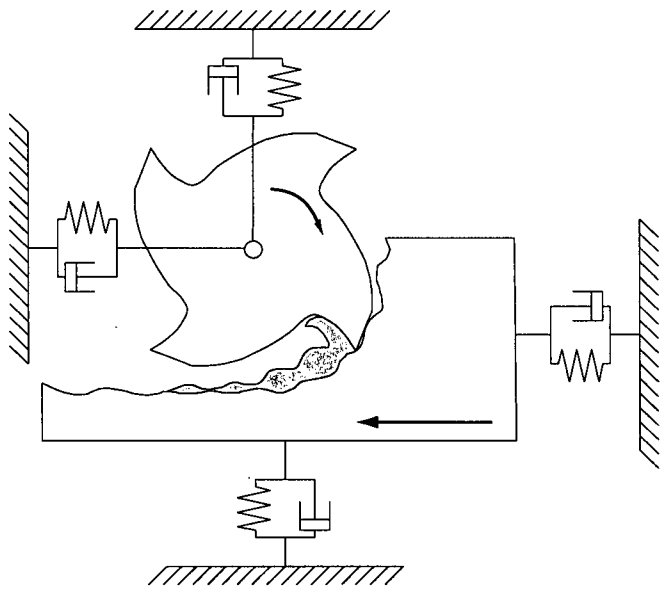

with a phase shift $\pi/2$ and the extreme case of a π phase shift, both of which can lead to unstable conditions. This oscillating chip thickness causes varying forces, which in turn adds more vibrations into the system. This feedback in the process is the regeneration effect which may cause instability.

The phase shift, ε in radians, can be calculated as a function of tooth period, T, and chatter frequency, ω_c:

$$2\pi k + \varepsilon = T\omega_c \tag{2-5}$$

where k is the number of complete wave marks on the surface during each tooth period. $\frac{\varepsilon}{2\pi}$ is the remaining fraction of a cycle between subsequent tooth passes.

FIGURE 2-3: Chip regeneration with various phase shifts

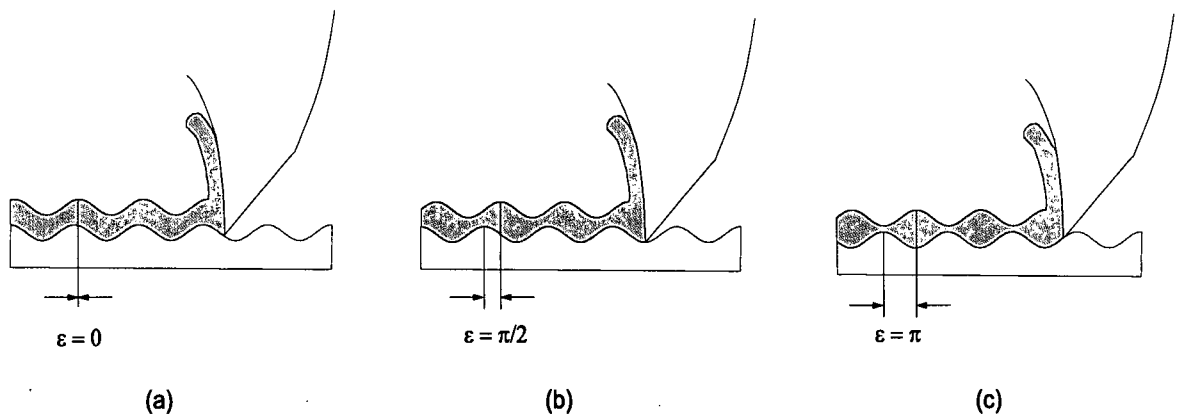

It can be seen that the most stable conditions, insofar as the regenerative effect is concerned, are when the tooth passing frequency is at an integer fraction of the chatter frequency, which results in a zero phase shift. This corresponds to spindle speeds, n [RPM], of:

$$n = \frac{60k\omega_c}{2\pi}, \qquad k = 1, 2, 3, \ldots \tag{2-6}$$

The non-linearity which occurs when the tool separates from the workpiece is described in [20], and Yoshitaka et al. [21].

The regeneration effect can be reduced significantly by using cutters with non-uniform pitch, which causes the phase shift, ε, to change successively for each tooth. The increased stability in milling with variable pitch cutters was first explained by Slavicek, [22]. Shortly following, Opitz et al. [23] and Vanherck [24] used computer simulations to predict the increased chatter stability with these cutters.

2.4.1.2 Other Effects Contributing to Self-Excited Vibrations

Two other principles causing self-excited vibrations are *mode-coupling*, introduced by Gurney [25], and the possible existence of a phase shift between the change in chip thickness

and the change in force. The latter has been ignored in most literature due to the lack of reliable quantitative data on the phase shift values, and on the questionable significance of the phase shift in practical calculations of chatter stability [26].

The theory of mode coupling is well detailed in [16] and [17]. Consider a hypothetical cutting process in which the regeneration effect could be excluded. Further, assume that the system contains a minimum of two modes in different directions and of different stiffnesses. The oscillating chip thickness from vibrations in the direction of one of the modes can cause a changing cutting force component in the direction of the other mode(s). It is possible under certain circumstances based on the orientation, natural frequency, and phase of the modes, and on the cutting conditions, that energy can accumulate in the system. If this surplus of energy is able to overcome damping losses in the system, the process may become unstable.

Investigations to decrease the effect of mode coupling in milling operations were done by Ismail et al. [27] [28] by using cutters with an increased flexibility in one direction. By optimizing the orientation and the flexibility of the more compliant mode, the decreased mode coupling effect was found to increase the chatter stability limit slightly under certain conditions.

2.4.1.3 Increased Stability Against Chatter at Lower Spindle Speeds

The causes of chatter discussed above make no mention to the increased stability consistently noticed at lower spindle speeds in practice and in carefully controlled cutting tests. There have been several proposed mechanisms responsible for this stability increase.

Tobias [16] attributed this to the *velocity principle* caused by the so called *penetration rate*. A penetration rate represented the damping supposedly contributed by the feed velocity and the oscillating velocity component perpendicular to the cutting direction due to vibrations. Penetration coefficients were determined experimentally for each mode of vibration and were used to model the increasing stability with decreasing cutting speed.

A more comprehensive explanation for this damping effect was provided by Sisson and Kegg [29], who describe the *process damping* in terms of physical quantities such as tool edge roundness, tool clearance angles, and chatter frequency. Due to the sharpness rounding of the cutting tool, part of the chip is forced under the tool and causes interference on the tool clearance flank. Sisson estimates an effective viscous damping coefficient based on elastic deformation of the workpiece material and friction at the flank face in terms of yield strength of the material, tool sharpness radius, clearance angle, cutting velocity, and coefficient of friction.

Later works [30] [31] [32] describe process damping as being primarily caused by the varying relief angle of the cutting tool due to vibrations. In Figure (2-4), a cutting tool is shown as it moves from left to right at the cutting speed and vibrates up and down. Moving over the crest from A to B, the actual relief angle, γ, closes down. Going through the trough from B to D, γ opens up. The cutting force consists of a steady component, F_{ave}, and a component, labelled F_1, which is proportional to the chip thickness and is 180° out of phase with the cutter vibration. There is an additional force component, labelled F_2, which depends on the relief angle, increasing as γ decreases sometimes to a negative value, when an interference and rubbing on the flank occurs. This component is maximum at point B and minimum at point D. Hence, there is a 90° degree phase shift between the vibrations and the resulting force component which creates a positive damping effect.

Sisson [29] is one of the few to attempt to predict the effective damping coefficients analytically. Typically, *Dynamic Cutting Force Coefficients* (DCFC's) are determined experimentally through a series of controlled dynamic cutting tests over a range of vibration amplitudes and frequencies, cutting speeds, and tool geometries [33] [34] [35]. The DCFC was expressed as a complex quantity such that the real part would determine the cutting force component in phase with the chip thickness, while the imaginary part would account for the process damping. Methods used for measuring the DCFC's are summarized by Tlusty in [30], who also presented the effect of tool wear on the DCFC's. Other work in process damping is presented in [36] and [37]

FIGURE 2-4: Origin of Process Damping

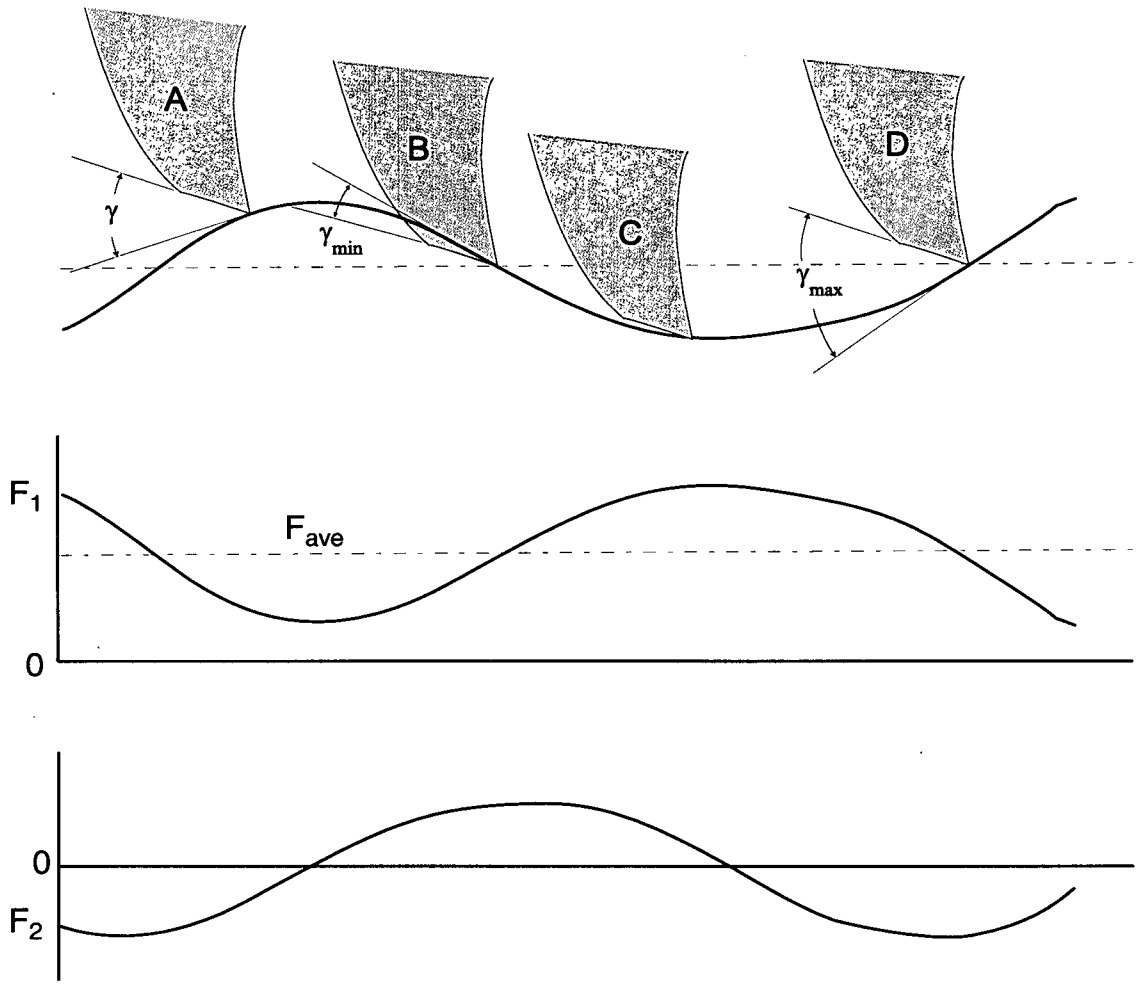

The process damping effect is not included in the time domain milling model used in this thesis. The majority of the focus will be on at cutting speeds above those affected by process damping. However, a newly reported phenomenon is discussed which was found to also contribute to low speed stability in milling. This phenomenon is based on an apparent decrease in the wave regeneration effect with increasing feed rate.

2.4.2 Chatter Stability Models

Chatter stability has been most commonly expressed by *stability lobe diagrams*, which plot the boundary that separates stable and unstable machining in the form of axial depth of cut limit versus spindle speed for a specific radial width of cut and workpiece-cutting tool combination. Referring to Figure (2-5), three borderlines of stability can be identified, called *lobed*, *tangent*, and *asymptotic*. The lobed borderline of stability is the exact borderline. The asymptotic borderline represents the principal borderline defining the maximum depth of cut for all spindle speeds. The tangential borderline follows the profile of the lobe tips, which for lower cutting speeds accounts for the increased stability due to process damping and other speed dependant effects.

FIGURE 2-5: Chatter stability borders: asymptotic, tangential, and lobed

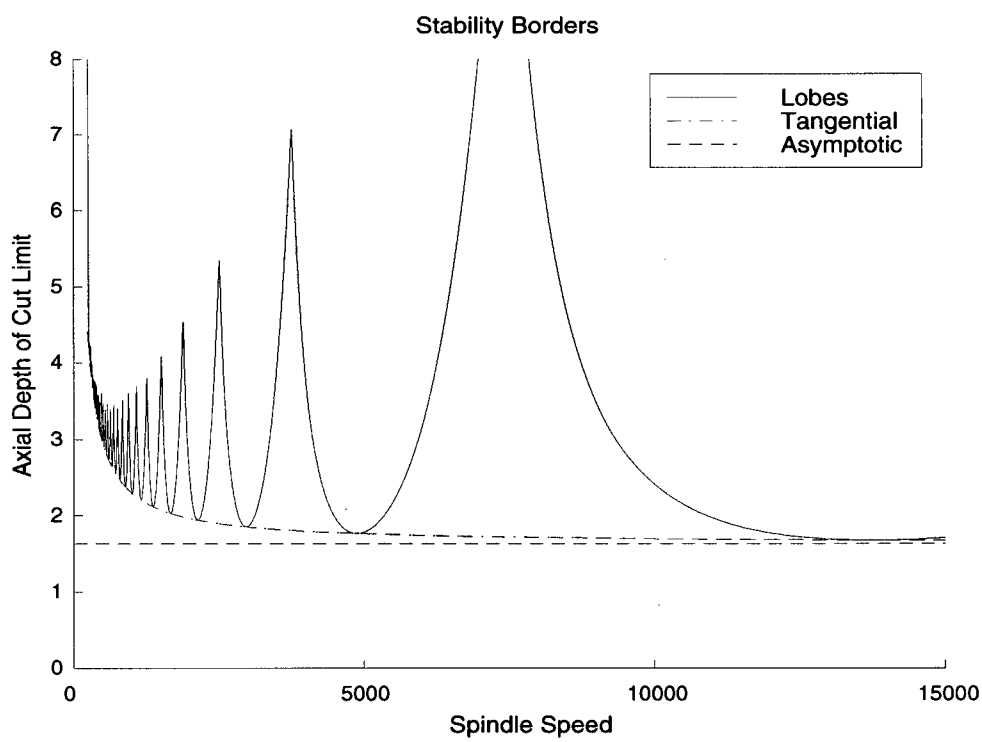

Predicting these stability borders has been the focus of much machining research since the 1950s. Tlusty and Polacek [38] [26] predicted the asymptotic borderline by considering positional mode coupling and regeneration effects, modelling the machine tool as a multi degree-of-freedom structure. The critical axial depth of cut limit, a_{lim}, was expressed by the classical equation:

$$a_{lim} = \frac{1}{2K_s \Re[G]_{min}} \tag{2-7}$$

where K_s is the specific cutting force coefficient, and $\Re[G]_{min}$ is the minimum value of the real component of the machine tool's transfer function, oriented with respect to the cutting surface and to the cutting force. Research by Tobias and Fishwick [39] and Merrit [40] provided methods of predicting the lobing effect of the stability limit. Merrit predicts the stability lobes by using feedback control theory to model the self-excited chatter effect. Tobias used the proposed "penetration effect" to account for increased stability at lower cutting speeds. However, alternate explanations for this effect, as discussed above, were later proposed [29] which gained more general acceptance. Process damping is often not included in predicting stability lobes due to the difficulty in accurately modelling its effects. The resulting stability diagram, in which the asymptotic borderline is coincident to the tangential borderline, becomes applicable only at higher spindle speeds.

These early works were developed using orthogonal cutting models in turning processes. In milling, prediction of chatter stability is further complicated by the rotating cutter, time varying cutting forces, direction of chip load, and multi degree-of-freedom structural dynamics. Sridhar et al. provided a comprehensive theoretical analysis of the milling process [41]. First, a model for a straight tooth cutter was derived with three basic assumptions: (a) the cutting force is represented as being proportional to the chip thickness, (b) the angle of the cutting force relative to the radial direction is constant, and (c) regeneration of waviness is limited to the surface left only by the tooth immediately preceding the current one. In [42] and [43] this was eventually extended to a generalized model for evaluating stability lobes in milling. The process is described by a linear differential-difference equation with periodic coefficients. Stability is determined by a numerical algorithm based on the mapping tech-

niques similar to the one used in the established Nyquist criterion. Opitz and Bernardi [44] simplified this model by taking average values of the time varying coefficients and the reduced stability equation is solved to give the stability lobes. Methods of stability analysis in milling are also discussed in [16] and [17].

Opitz et al. [23] and Vanherck [24] evaluated stability lobes for milling with variable pitch cutters. A stability gain of over 400% has been reported by using milling cutters with non-uniform pitch.

Due to the rapid development of computer processing power over the past twenty years, many proposed methods for determining stability limits in milling, following those just mentioned, rely on time domain simulations. In [20] Tlusty presented stability lobes evaluated by a series of time domain simulations in which the non-linearity of the cutting tool-workpiece separation during chatter is considered. Numerous models for time domain stability lobes have since been proposed. In [31], [18], and [19], Tlusty applied his model to high speed machining where process damping effects are negligible. In [45], Smith and Tlusty used time domain simulations to present dynamic cutting limits in the form of constant peak-to-peak force plots. This considers forced vibrations in addition to the vibrations caused by self-excitation mechanisms. Weck and Altintas [46] incorporated the simulated stability lobes to a CAD/CAM system for chatter free process planning.

Altintas and Montgomery [3] used a time domain simulation featuring a digitized workpiece and cutting tool model. The effect of process damping is included by considering cutting forces in five distinct regions where the cutting edge travels during dynamic cutting. Lee [4] extended the simulation to milling with ballend cutters. He used a peak-to-peak vibration amplitude criterion to determine the stability border through multiple time domain simulations.

Despite the heavy focus on time domain simulations for determining chatter stability limits, there have recently been significant contributions to analytical frequency domain prediction of stability lobes. Minis and Yanushevsky [47] [48] presented an analytical method for solving the dynamic milling model proposed by Sridhar et al. [43]. The dynamics of the milling

process were described by a set of differential-difference equations with time varying periodic coefficients. The stability of the system was examined using Fourier analysis and basic properties of the parametric transfer functions of linear periodic systems. Altintas and Budak [49] [50] solved the chatter stability lobes by an alternate method, relying on a stability model similar to those detailed by Tlusty [17] and Tobias [16]. The dynamic milling process was modelled by considering the Fourier series expansion of the time varying milling coefficients. Using the eigenvalue solution to the dynamic milling expression, analytical expressions were formulated for chatter-free axial depth of cut limits and spindle speeds as a function of the machine structure's transfer function at the tool-workpiece contact zone, static cutting force coefficients, number of flutes, and the radial width of cut. This analytical solution provides the same results as other frequency and time domain solutions, but by a more practical and direct method. In [51] a more generalized formulation was derived which accounts for varying cutter and workpiece dynamics along the axial depth of cut.

The stability model of Altintas and Budak [49] is expanded in this thesis to include the effects of feed rate. It will be shown that even without the effect of process damping, the tangential borderline of stability increases at lower spindle speeds due to the feed rate. The tangential stability borderline may follow a second lobing pattern with varying spindle speed, depending on the cutting conditions.

2.4.3 Time Domain Simulation of Milling Flexible Structures

The time domain simulations discussed above are mainly for the purpose of determining the stability border of dynamic milling. Other useful predictions can be obtained by the use of time domain simulations, such as cutting forces and bending moment acting on the machine tool, machining torque and power requirements, surface error profile from static and dynamic deflection and surface roughness due to chatter. Furthermore, time domain simulations are extremely useful for detailed examination of non-linear effects such as tool-workpiece separation during chatter, cutting tool runout, exact kinematics of milling which considers workpiece feed, and complex cutting tool geometries. The simulations of concern in this study are those modelling the milling process which consider a flexible workpiece and flexible machine tool/cutter.

Kline, DeVor, and Shareef [52] developed a computer simulation to predict the surface finish as a result of static deflection of the cutting tool and of the workpiece during milling. The endmill cutter was modelled using the equation of a slender cantilever beam, while the workpiece was modelled by finite elements as a plate clamped at three edges with one edge free to deflect. The machined surface profile along the axial depth of cut was determined by tracing the relative static cutter-workpiece deflection as the point of contact move upwards along the cutting tool during cutting due to the helix angle. In [53] Kline and DeVor studied in detail the effects of runout on milling forces using time domain simulations. However, Kline did not include the regeneration effect of chatter, validating the model only for the case of static milling.

Montgomery and Altintas [3] [32] provided an improved time domain milling model of thin plates in which the cutter and workpiece were represented by digitized surfaces. A computer program maintained a cutting surface array which allows the exact kinematics of milling to be modelled, including the trochoidal tooth path, regeneration of waviness, changing tool immersion due to static and dynamic deflection. The model predicted dynamic cutting forces, surface finish including the effects of chatter, and workpiece vibrations. The plate was modelled using an off-line finite element package, while the cutter was assumed to be rigid.

Lee [4] used a model similar to that of Montgomery and Altintas for prediction of cutting forces, surface finish, and chatter stability limits for ballend milling. The model is restricted to half and full immersion cutting.

Sagherian and Elbestawi [54] [55] improved on Kline's simulation by adding the regeneration effect, a dynamic cutter deflection model, and a dynamic workpiece deflection model. The cutter was modelled by a measured transfer functions in the X and Y directions at the cutter tip. The identified modal parameters at the tip were extrapolated using cantilever theory to obtain mass and stiffness at points along the axial length of the cutter. The workpiece was modelled using the finite element method. The dynamics of the workpiece was updated throughout the simulation as material was removed during milling. Sinusoidal approximation of static chip thickness was used and the changing radial immersion with cutter and

workpiece deflection was not considered. The axial surface profile was predicted, but surface roughness in the feed direction due to vibrations was not obtained.

The comprehensive milling model proposed in this thesis combines methods used by several of the above works. Dynamic structural characteristics of the machine tool, cutter, and workpiece will be determined through experimental modal analysis. The cutting surface is modelled using an algorithm combining that used by Montgomery and that used by Lee. Exact milling kinematics are used, uniform or non-uniform pitch cutter geometry, and cutter runout are all included in the model. Dynamic cutting forces, cutter and workpiece vibrations, surface finish, bending moment on the spindle, power, and chatter stability borders are all predicted. The stability lobes predicted by time domain simulations are explained and supported by an improved analytical model based on that of Budak and Altintas [49]. Where possible, experimental cutting tests are performed to validate results.

CHAPTER 3

Dynamic Modelling of the Workpiece and Machine Tool

3.1 Introduction

Many different models and numerical techniques may be used for simulating structural dynamics of a machine tool and workpiece. Simplified models consisting of a single dominant mode in each direction are very commonly used, which can lead to accurate enough results for smaller depths of cut, provided other modes are relatively stiff. For larger depths of cut, where the dynamics may change at different points along the length of the cutter, multiple degrees of freedom must be considered in each direction. In the past, some authors have used the finite element method to derive mode shapes and other dynamic parameters for modelling dynamics of the workpiece when machining flexible plates [3][54]. For more complicated geometry workpieces, however, the initial work involved in modelling the structure for the finite element method may be impractical. Modal analysis provides a more practical alternative, which relies on experimentally measured transfer functions at various points on a structure. In this chapter, the procedures for acquiring and processing measured transfer functions to identify structural dynamic parameters are discussed.

The workpiece and machine/cutting tool structural dynamics are modelled as two independent entities. Each structure is divided into N fixed number of measurement points, or degrees-of-freedom, as shown in Figure (3-1).

FIGURE 3-1: Discretized dynamic model of cutting tool and workpiece

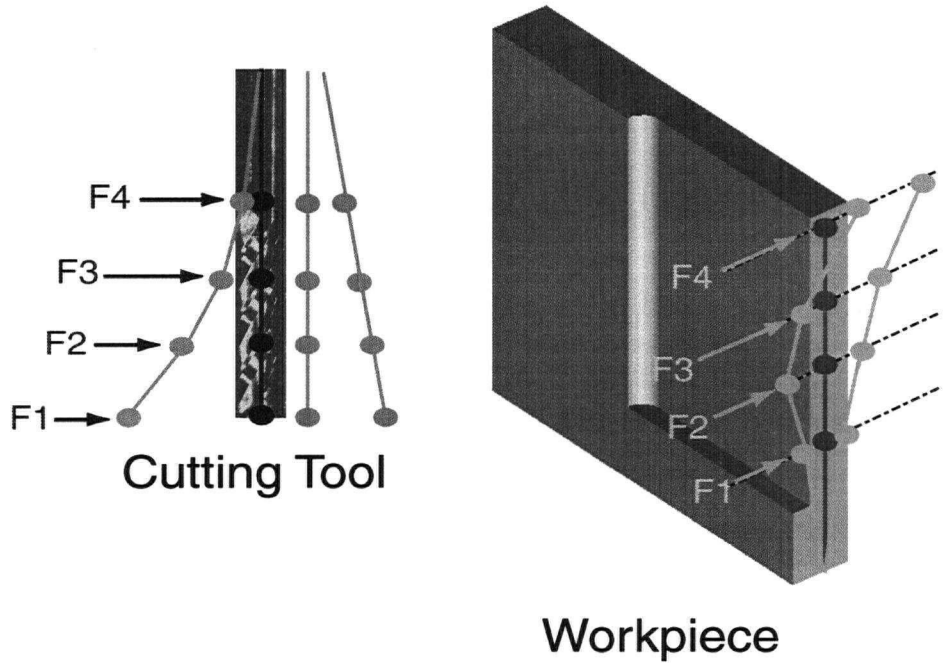

3.2 Dynamic Model of Workpiece and Machine Tool

The most general second order linear dynamic model is one which uses the elements of mass, damping, and stiffness matrices *[M]*, *[C]*, and *[K]* in the differential equation shown below in time, frequency, and Laplace domains.

Time Domain:

$$[M]\{\ddot{x}(t)\} + [C]\{\dot{x}(t)\} + [K]\{x(t)\} = \{f(t)\} \tag{3-1}$$

Frequency Domain:

$$-\omega^2[M]\{X(i\omega)\} + j\omega[C]\{X(i\omega)\} + [K]\{X(i\omega)\} = \{F(i\omega)\} \tag{3-2}$$

Laplace Domain:

$$s^2[M]\{X(s)\} + s[C]\{X(s)\} + [K]\{X(s)\} = \{F(s)\} \tag{3-3}$$

In analytical methods of solving the differential equation, the matrices are estimated from material properties, geometry, and/or measured forces and responses. The modal parameters of N modes with N degrees-of-freedom are then found by the solution of the classic eigen-value-eigenvector problem, and the differential equation is solved in modal coordinates.

The alternative approach is to directly fit modal parameters of M modes to experimental data in the form of input-output relationships at N measurement points on the structure. In the frequency domain, for general viscous damping, a common form of the frequency response function is the *pole/residue* or *rational fraction expansion* form:

$$H_{pq}(\omega) = \sum_{k=1}^{M} \frac{A_{pqk}}{j\omega - \lambda_k} + \frac{A_{pqk}^*}{j\omega - \lambda_k^*} \tag{3-4}$$

where,

k is the mode number,

p is the response measured degree-of-freedom,

q is the input or reference measured degree-of-freedom,

A_{pqk} is the complex residue for input q, response p, and mode k,

λ_k is the system pole for mode k: $\lambda_k = -\zeta_k\omega_{nk} + j\omega_{dk}$,

ζ_k is known as the damping ratio for mode k,

ω_{nk} is the natural frequency of mode k in [rad],

ω_{dk} is the damped natural frequency for mode k: $\omega_{dk} = \omega_{nk}\sqrt{1-\zeta_k^2}$,

and the operator * indicates complex conjugate.

This model assumes *linearity* and *diagonalizability*, which implies the modes are orthogonal and can be decoupled [56]. Further assumptions of *reciprocity* and *proportional damping* are also made, which greatly simplify modal analysis.

Proportional damping is a simplification which assumes that the viscous damping matrix, *[C]*, is a linear combination of the mass, *[M]*, and stiffness matrix, *[K]*; i.e.: $[C] = \alpha[M] + \beta[K]$. This leads to real component of the residue equalling zero [56]. The frequency response function for mode k can now be written in a simplified matrix polynomial form in which the contribution of complex conjugate poles are combined.

$$[H_k(\omega)] = \frac{\{u_{Lk}\}^T\{u_{Rk}\}}{-\omega^2 + 2\zeta\omega_{nk}j\omega + \omega_{nk}^2} \tag{3-5}$$

where $\{u_{Lk}\}$ and $\{u_{Rk}\}$ are the response and reference mode shape vectors, also known as the left and right mode shape vectors, which, for the case of proportional damping, are real.

Models with the reciprocity property can be written in symmetrical form where the system matrices *[M]*, *[C]*, and *[K]* are symmetrical and the left and right mode shape vectors, $\{u_{Lk}\}$ and $\{u_{Rk}\}$, are equal. It follows from Maxwell's reciprocity theorem that the transfer function at response p and reference q equals the transfer function at response q and reference p.

The parameters defining the dynamic model are now N mode shape coefficients, a damping ratio and a natural frequency for each mode. The $M(N+2)$ parameters are fit to experimental measurements as discussed in the next section. The validity of the above assumptions are ultimately verified if an acceptable fit is achieved using the estimated parameters.

3.3 Identification of Structural Dynamic Parameters

Having defined a dynamic model for the workpiece and cutting tool motion, it is necessary to experimentally evaluate the modal parameters ω_n, ζ, and $\{u\}$ for each mode. These parameters may be fit to measured transfer function data in various ways.

Although there are numerous commercial modal analysis packages already available, new software was created which could be tailored specifically for more efficient and more flexible parameter fitting of simple cutter and workpiece structures. Furthermore, since the

modal analysis software uses the same dynamic model as in the milling simulation, the estimated parameters are directly useable by the milling analysis software.

3.3.1 Transfer Function Measurements

Transfer function measurements of the cutting tool and of the workpiece structures can be obtained using a Fourier analyzer from hammer impact testing. A total of N^2 frequency response functions could be measured taking each N response degrees of freedom with N reference degrees of freedom. From the reciprocity assumption, theoretically only N measurements are required to fully define the modal matrix. Either the reference measurement or the response measurement may be kept at any fixed point. The following discussion assumes a fixed response point p and N reference points denoted by subscript q.

With an accelerometer measuring motion at point p on the structure, a measured impact force is applied at point q of the structure to excite its natural frequencies. The Fourier analyzer provides the frequency response function:

$$H''_{pq}(\omega) = \frac{X''_p(\omega)}{F_q(\omega)} \tag{3-6}$$

in [acceleration]/[force] units for discrete values of ω. The frequency response function is converted to [displacement]/[force] units by dividing the transfer function at each frequency by $-\omega^2$.

$$\frac{X_p(\omega)}{F_q(\omega)} = H_{pq}(\omega) = -\frac{H''_{pq}(\omega)}{\omega^2} \tag{3-7}$$

With the accelerometer fixed at point p on the structure, frequency response functions are measured from impact loads at all N points on the structure.

3.3.2 Modal Parameter Estimation Model

The generalized model used for parameter estimation, from equation (3-4), is:

$$H_{pq}(\omega) = \sum_{k=1}^{M} \frac{A_{pqk}}{j\omega - \lambda_k} + \frac{A_{pqk}^*}{j\omega - \lambda_k^*} \tag{3-8}$$

although it will be used in various forms throughout different stages of the estimation algorithm. A polynomial form of the model will be used for linear least squares fitting, while the non-linear optimization and synthesis will be in terms of variables most meaningful and most workable for the user (natural frequency, ω_{nk}, damping ratio, ζ_k, and residues, A_{pqk}).

Although the real component of the residue can be ignored from the proportional damping assumption made above, it is included in parts of the estimation model for completeness. The main purpose of this assumption was to simplify modal analysis of multiple reference or multiple response measurements. In the case where the parameters of only one transfer function need to be estimated, the more general model of equation (3-8) should be used.

Different parameter estimation methods are well summarized in [57], [58], [59], and [60]. Since the combined response function of multiple modes being fitted is non-linear, the parameters are typically fit in multiple stages. One approach is to break up the problem into multiple linear problems, first estimating the system poles, then estimating modal coefficients in a second stage. Alternatively, an iterative solution procedure may be used allowing all modal parameters to vary until an error criterion reaches an acceptable level. In this case, a set of starting values must be selected, which can greatly influence the final solution.

The method adopted below is one which first uses a two stage linear least squares solution for initial estimation of the parameters of each mode individually. Next, a non-linear steepest descent search algorithm with a least squares error function is used to optimize the parameters in a global sense.

3.3.3 Residual Modes

When estimating the parameters of a single mode, a limited frequency range of the measured data, R, must be selected which contains the mode. However, since the measured frequency response function within R may consist of multiple superimposed modes, modes outside the

range, termed *residual modes*, need to be considered. Two additional terms are required to include the effect of residual modes below the frequency range, often called residual inertia, and the effect of residual modes above the frequency range, termed residual flexibility.

$$H_R(\omega) = H_{low}(\omega) + \frac{A_k}{j\omega - \lambda_k} + \frac{A_k^*}{j\omega - \lambda_k^*} + H_{hi}(\omega) \tag{3-9}$$

where,

$H_{low}(\omega)$ is the residual effect of lower frequency modes

$H_{hi}(\omega)$ is the residual effect of higher frequency modes

In this thesis, the residual modes are modelled as undamped second order linear systems of two arbitrarily selected frequencies, $\omega_{n,\,low}$ to account for lower frequency modes and $\omega_{n,\,hi}$ to account for higher frequency modes. The frequency response function within frequency range R can be written in polynomial form as:

$$H_R(\omega) = \frac{\alpha_{low} + \beta_{low}(j\omega)}{-\omega^2 + \omega_{n,\,low}^2} + \frac{\alpha_k + \beta_k(j\omega)}{-\omega^2 + 2\zeta_k\omega_{n,\,k}(j\omega) + \omega_{n,\,k}^2} + \frac{\alpha_{hi} + \beta_{hi}(j\omega)}{-\omega^2 + \omega_{n,\,hi}^2} \tag{3-10}$$

3.3.4 Linear Least Squares Estimation of Natural Frequency and Damping Ratio

The first stage of the fitting algorithm is to estimate the poles (in the form of natural frequencies and damping ratios) of a single mode. A user selected range, R, of the frequency response spectrum is used for each fit. For the purpose of fitting the unknown α and β parameters, equation (3-10) becomes non-linear.

By multiplying both sides of the equation by $(-\omega^2 + 2\zeta_k\omega_{n,\,k}(j\omega) + \omega_{n,\,k}^2)$ and ignoring higher order terms of the residual modes, the model may be approximated as:

$$H_R(\omega)(-\omega^2 + 2\zeta_k\omega_{n,\,k}(j\omega) + \omega_{n,\,k}^2) = \alpha_k + (j\omega)\beta_k + \frac{C_1}{-\omega^2 + \omega_{n,\,low}^2} + \frac{C_2}{-\omega^2 + \omega_{n,\,hi}^2} \tag{3-11}$$

where C_1, and C_2 are complex residual constants. As long as the residual terms account for the effects of out-of-band modes, they can take on any convenient mathematical model [57]. The lack of physical significance of these terms should be noted, however. The estimated residual terms are meaningless, but provide a model sufficient for estimating the natural frequency and damping coefficients of the mode of interest.

Equation (3-11) may be divided into real and imaginary components and written as:

$$\begin{aligned} -\omega^2\Re[H_R(\omega)] + d\Re[H_R(\omega)] - \omega c\Im[H_R(\omega)] &= \alpha_k + \left.\frac{\mu_1}{-\omega^2+\omega_{n,\,low}^2} + \frac{\mu_2}{-\omega^2+\omega_{n,\,hi}^2}\right\} \Re \\ \omega c\Re[H_R(\omega)] - \omega^2\Im[H_R(\omega)] + d\Im[H_R(\omega)] &= \omega\beta_k + \left.\frac{\mu_3}{-\omega^2+\omega_{n,\,low}^2} + \frac{\mu_4}{-\omega^2+\omega_{n,\,hi}^2}\right\} \Im \end{aligned} \tag{3-12}$$

where,

$$c = 2\zeta_k\omega_{n,\,k}$$

$$d = \omega_{n,\,k}^2$$

$$\mu_1 = \Re[C_1]$$

$$\mu_2 = \Re[C_2]$$

$$\mu_3 = \Im[C_1]$$

$$\mu_4 = \Im[C_2]$$

Equation (3-12) can be written in the matrix form $[A(\omega)]\{P\} = \{B(\omega)\}$ as:

$$\begin{bmatrix} -\omega\Im[H_R(\omega)] & \Re[H_R(\omega)] & -1 & 0 & \dfrac{-1}{-\omega^2+\omega_{n,\,low}^2} & \dfrac{-1}{-\omega^2+\omega_{n,\,hi}^2} & 0 & 0 \\ \omega\Re[H_R(\omega)] & \Im[H_R(\omega)] & 0 & -\omega & 0 & 0 & \dfrac{-1}{-\omega^2+\omega_{n,\,low}^2} & \dfrac{-1}{-\omega^2+\omega_{n,\,hi}^2} \end{bmatrix} \begin{Bmatrix} c \\ d \\ \alpha_k \\ \beta_k \\ \mu_1 \\ \mu_2 \\ \mu_3 \\ \mu_4 \end{Bmatrix} = \begin{Bmatrix} \omega^2\Re[H_R(\omega)] \\ \omega^2\Im[H_R(\omega)] \end{Bmatrix} \tag{3-13}$$

With multiple data samples at different frequencies ω_1, ω_2,..., ω_n, equation (3-13) may be written in the form $[A]\{P\} = \{B\}$:

$$\begin{bmatrix} A(\omega_1) \\ A(\omega_2) \\ \cdots \\ A(\omega_n) \end{bmatrix} \{P\} = \begin{Bmatrix} B(\omega_1) \\ B(\omega_2) \\ \cdots \\ B(\omega_n) \end{Bmatrix} \tag{3-14}$$

In this linear matrix form, the unknowns, *{P}*, may easily be estimated using the linear least squares solution:

$$\{P\} = ([A]^T[A])^{-1}[A]^T\{B\} \tag{3-15}$$

The natural frequency and damping ratio, $\omega_{n,k}$, and ζ_k, are retained here, while the remaining residue variables are discarded.

Only data from a single measurement needs to be used here to estimate the system poles. Although, it should be noted that the poles are treated as global parameters. A later stage will ensure that the parameters provide the best fit for all measured transfer functions.

3.3.5 Linear Least Squares Estimation of Residues

Having estimated unknowns *c* and *d*, the original form of the SDOF model with residual modes (equation (3-10)) can be written as a real and imaginary pair of linear equations in terms of the six remaining unknowns α_k, β_k, α_{low}, β_{low}, α_{hi}, β_{hi}.

$$\begin{aligned} &\Re[H_R(\omega)]D_1D_2D_4 - \Im[H_R(\omega)]D_1D_3D_4 \\ &= \alpha_{low}D_2D_4 - \beta_{low}\omega D_3D_4 + \alpha_k D_1D_4 + \alpha_{hi}D_1D_2 - \beta_{hi}\omega D_1D_3 \\ &\Re[H_R(\omega)]D_1D_3D_4 + \Im[H_R(\omega)]D_1D_2D_4 \\ &= \alpha_{low}D_3D_4 + \beta_{low}\omega D_2D_4 + \beta_k\omega D_1D_4 + \alpha_{hi}D_1D_3 + \beta_{hi}\omega D_1D_2 \end{aligned} \tag{3-16}$$

or, in matrix form:

$$\begin{bmatrix} D_1D_4 & 0 & D_2D_4 & -\omega D_3D_4 & D_1D_2 & -\omega D_1D_3 \\ 0 & \omega D_1D_4 & D_3D_4 & \omega D_2D_4 & D_1D_3 & \omega D_1D_2 \end{bmatrix} \begin{Bmatrix} \alpha_k \\ \beta_k \\ \alpha_{low} \\ \beta_{low} \\ \alpha_{hi} \\ \beta_{hi} \end{Bmatrix} = \begin{Bmatrix} \Re[H_R(\omega)]D_1D_2D_4 - \Im[H_R(\omega)]D_1D_3D_4 \\ \Re[H_R(\omega)]D_1D_3D_4 + \Im[H_R(\omega)]D_1D_2D_4 \end{Bmatrix} \tag{3-17}$$

where,

$$D_1 = -\omega^2 + \omega_{n,\,low}^2$$

$$D_2 = -\omega^2 + \omega_{n,\,k}^2$$

$$D_3 = 2\zeta_k\omega_{n,\,k}^2\omega$$

$$D_4 = -\omega^2 + \omega_{n,\,hi}^2$$

As in the case for estimating $\omega_{n,\,k}$ and ζ_k, (3-17) can be written in the form of equation (3-14) and solved using the linear least squares solution of equation (3-15). The residual terms are discarded and the complex residue for mode k, A_{kpq} is estimated as:

$$A_{kpq} = \frac{\beta_k}{2} + j\left(\frac{\alpha_k - \beta_k\omega_{n,\,k}\zeta_k}{-2\omega_{d,\,k}}\right) \tag{3-18}$$

A single mode of a measurement frequency response function has now been identified with the parameters $\omega_{n,\,k}$, ζ_k, and A_{kpq}. While the poles of the system, (in terms of $\omega_{n,\,k}$ and ζ_k) are global parameters, the residue must be estimated for each measurement. The values of $\omega_{n,\,k}$ and ζ_k, as estimated by a single measurement, may be used in (3-17) to repeat the estimation of residues for all measurements. The global parameter estimation stage in the next section will ensure all parameters achieve a best fit for all measured response functions. Alternatively, there are other identification methods in which $\omega_{n,\,k}$ and ζ_k may be estimated globally. Some of these are detailed in [62].

In the case of proportional damping, the real part of the residue is zero. From equation (3-18), this translates to $\beta_k = 0$. Terms corresponding to β_k can be dropped from equation (3-17), and the residue is estimated as:

$$A_{kpq} = -j\left(\frac{\alpha_k}{2\omega_{d,k}}\right) \tag{3-19}$$

Figures (3-2) through (3-4) show the measured transfer function at the tool tip of a 3/4 inch diameter carbide helical endmill mounted on a Fadal vertical machining center with a hydraulic chuck. The identified parameters are listed in Table (3-1). Figure (3-2) shows mode 2 synthesized with the effect of residual modes, for the frequency range which was used during identification. Figure (3-3) shows the mode without the effects of residual modes for the entire frequency spectrum. When all identified modes are superimposed, the residual modes are left out. Figure (3-4) shows the complete transfer function of all modes identified with the procedure above

TABLE 3-1: Identified Modal Parameters with Complex Residues

Mode #	Nat. Freq. [Hz]	Damping Ratio	Residue ($\Re$)	Residue ($\Im$)
1	497.156	9.47E-02	6.47E-06	-1.99E-05
2	661.45	5.04E-02	2.00E-05	-2.90E-05
3	887.04	6.39E-02	9.88E-07	-5.50E-05
4	1642.10	2.54E-02	8.98E-07	-3.19E-06
5	2199.50	1.61E-02	-3.56E-06	-4.76E-05
6	2796.94	2.86E-02	-2.33E-05	-9.41E-05
7	3837.84	7.24E-03	-6.78E-06	-6.21E-05
8	4924.14	1.78E-02	-9.44E-06	-5.71E-05
9	6038.96	1.61E-02	2.08E-06	-1.24E-05
10	7899.67	5.46E-03	-9.48E-07	-1.47E-06

3.3.6 Global Non-Linear Optimization of Parameter Identification

Often the estimations of each mode individually, accounting for the effects of residual modes, provides sufficiently accurate results. For systems with heavy modal coupling, however, it is desired to further optimize the fit of the parameters globally, considering all modes

FIGURE 3-2: Single complex mode identification with residual modes

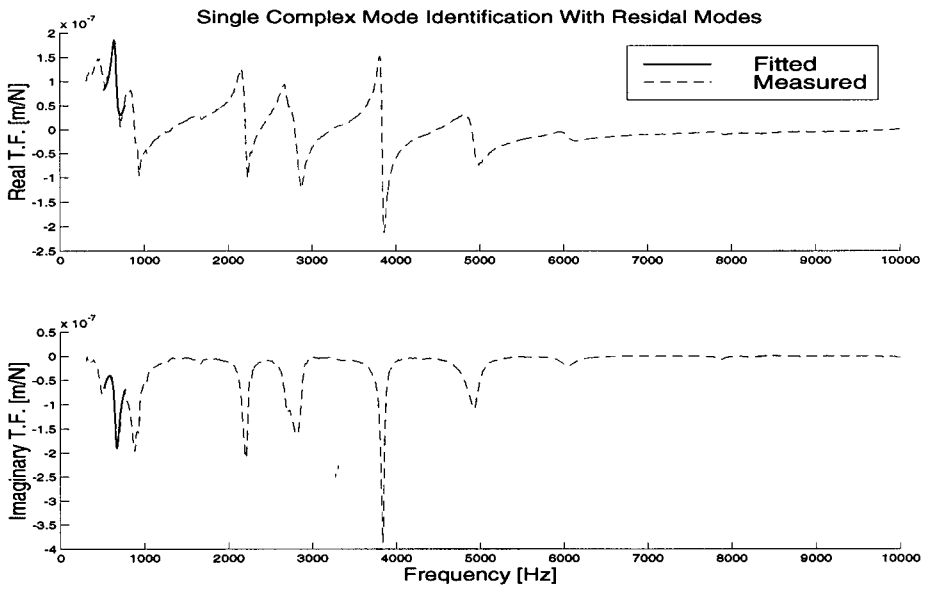

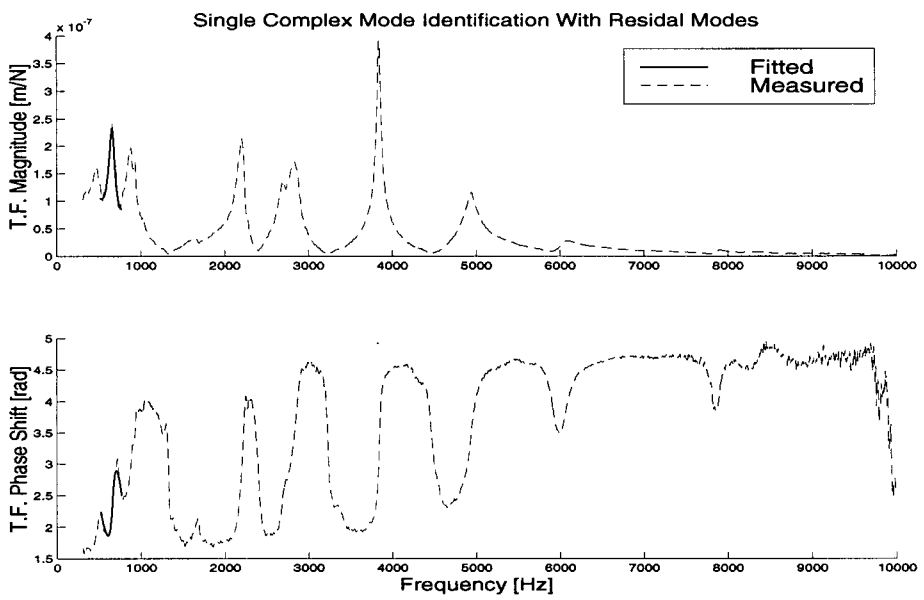

FIGURE 3-3: Single complex mode synthesized without residual modes

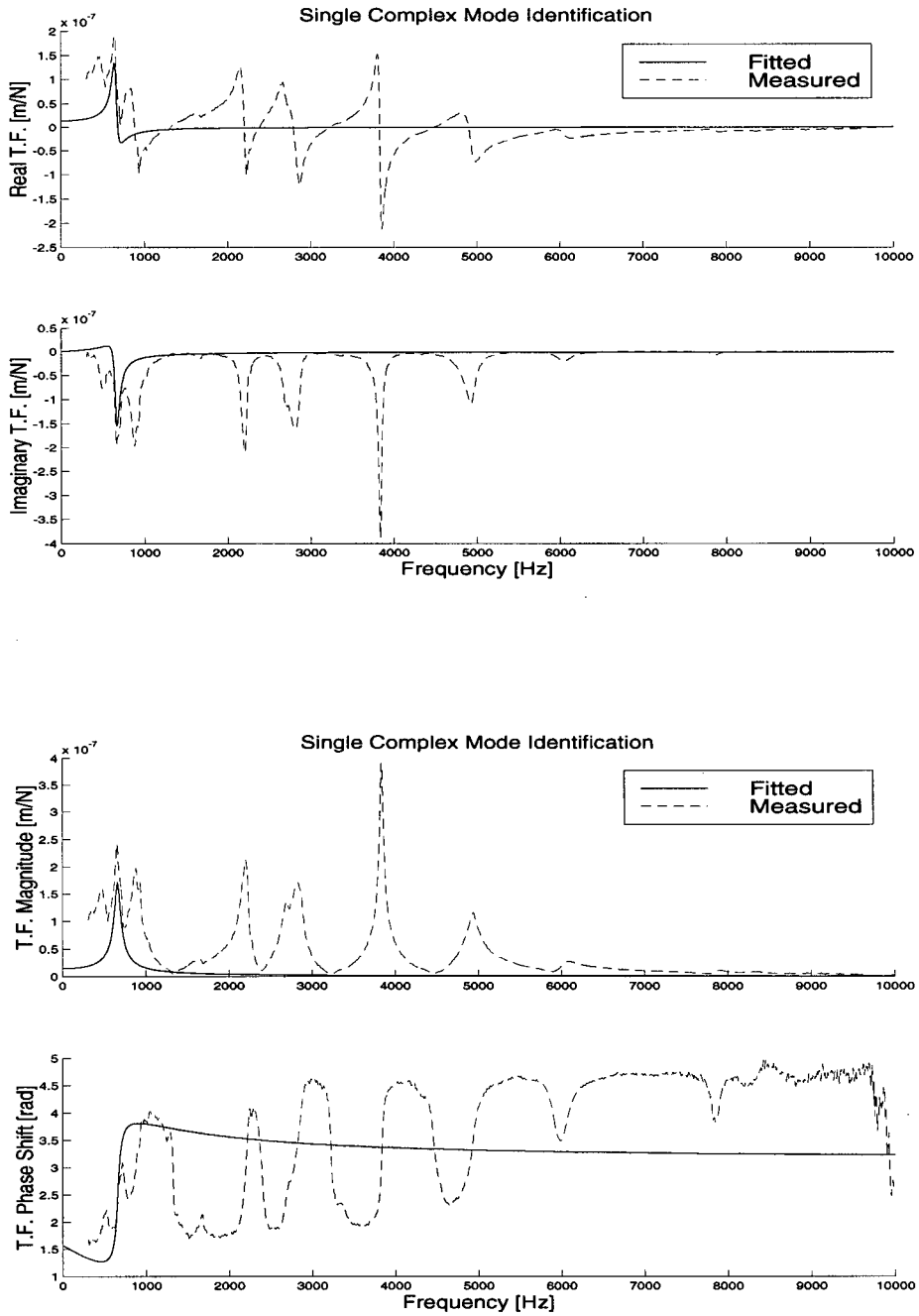

FIGURE 3-4: Multiple complex mode identification

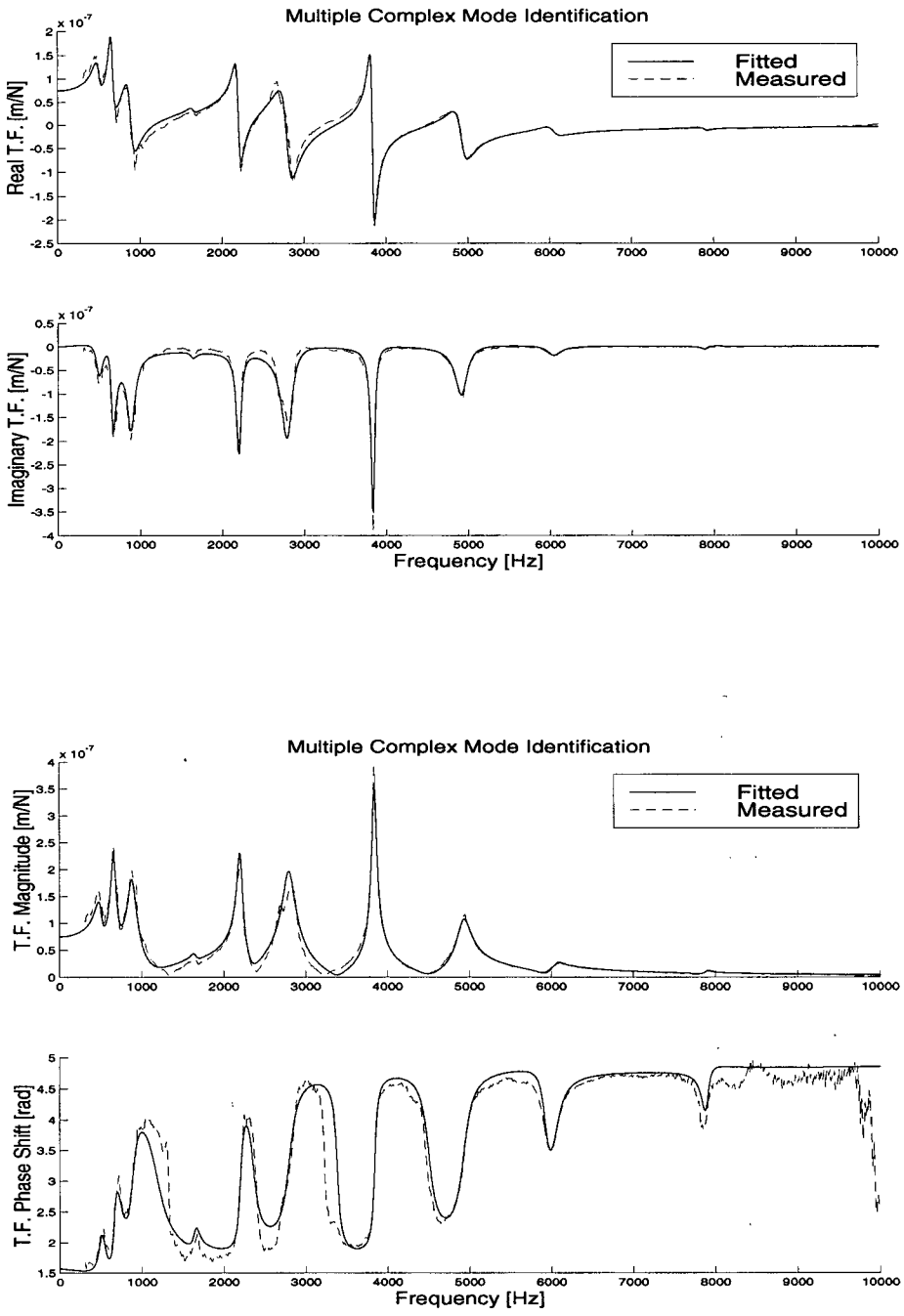

and all measured frequency response functions simultaneously. For this stage of the fitting algorithm, a non-linear least squares steepest descent search algorithm [61] is adopted in which all parameters are varied until a specified error criteria is reached.

Another alternative for global parameter estimation, as detailed in [56], is to use a similar iterative algorithm just for the pole parameters and evaluate the residues using the linear least squares solution above at each iteration step.

The model of each measurement using the superposition of all modes is:

$$[H_{pq}(\omega)] = \sum_{k=1}^{M} \frac{2(\zeta_k \omega_{nk} \Re[A_{kpq}] - \omega_{dk} \Im[A_{kpq}]) + 2\Re[A_{kpq}](j\omega)}{-\omega^2 + 2\zeta_k \omega_{nk}(j\omega) + \omega_{nk}^2} \tag{3-20}$$

For this stage, the model is written in terms of natural frequency, ω_{nk}, damping ratio, ζ_k, and complex and real components of the residues, A_{pqk}, since these parameters are most commonly understood by the user. The user interface designed for this estimation algorithm allows setting parameters to user defined values and also allows the algorithm to fix terms during the optimization stage.

The $M(2N+2)$ estimation parameters ω_{nk}, ζ_k, $\Re[A_{kpq}]$, and $\Im[A_{kpq}]$ are represented as p_j, where $j = 1, 2, \ldots, M(2N+2)$. The measured response function is denoted as $H_{pq}(\omega)$ and the estimated function as $\tilde{H}_{pq}(\omega, p)$.

The cost function used to evaluate the fit, J, is the summed magnitudes of $\Delta H_{pq}(\omega, p)$,the difference between the measured and the estimated functions $H_{pq}(\omega)$ and $\tilde{H}_{pq}(\omega, p)$, for all n data points and all N measurements:

$$J(\omega, p) = \sum_{q=1}^{N} \sum_{i=1}^{n} (\Re[\Delta H_{pq}(\omega_i, p)]^2 + \Im[\Delta H_{pq}(\omega_i, p)]^2) \tag{3-21}$$

For the steepest descent approach, the parameters are updated in the direction of the negative gradient $-\nabla J$. The partial fractions are individually evaluated by numerical approximating the slope over a small interval of the parameter, Δp:

$$\frac{\partial J}{\partial p_j} = \frac{J(\omega, p) - J(\omega, p')}{\Delta p} \tag{3-22}$$

where p' are the parameters p with p_j incremented by Δp. For each iteration, the parameters are then updated as:

$$p_j = p_j - S\frac{\partial J}{\partial p_j} \qquad j = 1, 2, \ldots, M(2N+2) \tag{3-23}$$

where S is the step size, which is selected for optimum decrease of the cost function J. The cost function is first evaluated with a step size of $S = 1.0$. If the cost function decreased, S is incremented by a factor γ ($\gamma > 1.0$), as $S_{new} = \gamma S_{prev}$ until a minimum J is found in the direction $-\nabla J$. Alternatively, if the cost function increased, S is decremented as $S_{new} = \frac{S_{prev}}{\gamma}$ until a step size is found causing J to decrease. Note that while moving in the direction $-\nabla J$, the cost function will always decrease given a small enough interval.

The algorithm continues until the relative change in J between iterations reaches an acceptably small value, ε. The condition for completion is:

$$\frac{|J_{new} - J_{old}|}{J_{new}} < \varepsilon \tag{3-24}$$

Figure (3-5) shows the optimized fit of the transfer function identified above from Figure (3-4).

3.3.7 Evaluating Mode Shape Vectors

After identifying the modal parameters of all MDOF measurements, the evaluation of mode shapes becomes trivial with the assumption of proportional damping. In equation (3-19), α_k

FIGURE 3-5: Optimized multiple complex mode identification

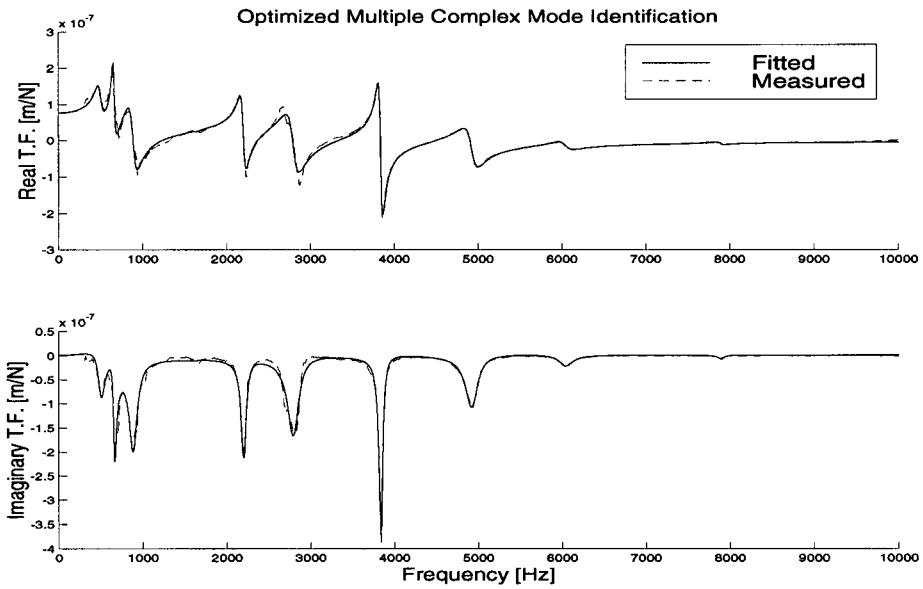

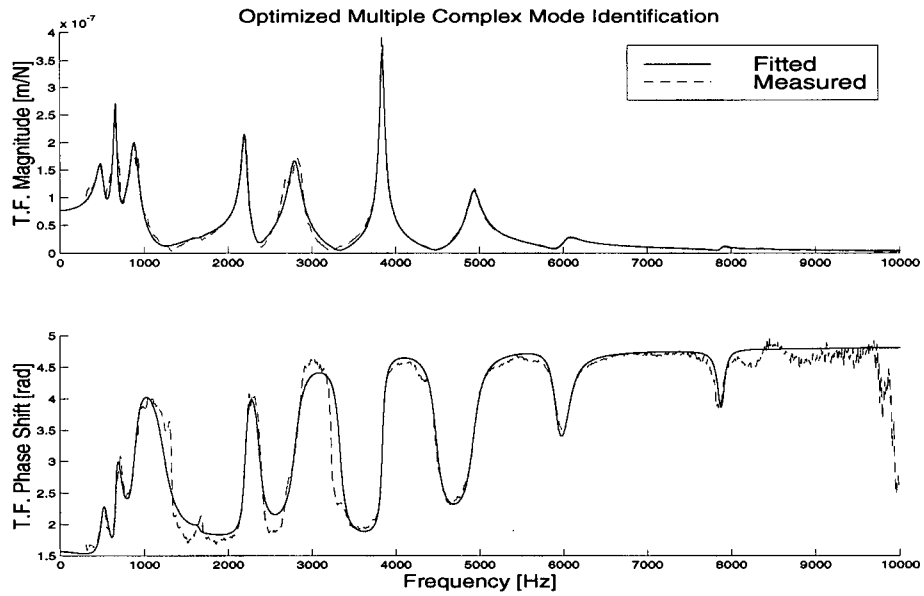

corresponds to the product of the mode shape coefficients of the response degree-of-freedom, p, and the reference degree-of-freedom q, $u_{k,p}u_{k,q}$. Assuming a fixed response point, p, the mode shape coefficients are defined as:

$$u_{k,p} = \sqrt{-2A_{kpq}\omega_{d,k}}$$

$$u_{k,q} = \frac{-2A_{kpq}\omega_{d,k}}{u_{k,p}} \qquad q = 1, 2, \ldots, N \tag{3-25}$$

where $\Re[A_{kpq}] = 0$. Note that for the mode shape coefficient for measurement p, the residue must be negative for $u_{k,p}$ to be a real value. This enforces that the structure will always move in the direction of the applied force at the point of impact.

Figure (3-6) shows measured and fitted transfer functions measured at four points along the axial depth of cut of a thin plate workpiece. The modes are identified in the form of real modes. The natural frequencies, damping ratios, and mode shapes are listed in Table (3-2).

TABLE 3-2: Identified Modal Parameters with Real Mode Shapes

Measurement Point (measured from top of plate)	Mode Shape for Mode 1: ω_n =1540 Hz ζ =0.035	Mode Shape for Mode 2: ω_n =3769 Hz ζ =0.041
Point 1: 0mm	3.871572	3.471743
Point 2: 10mm	2.461387	2.810272
Point 3: 20mm	2.106084	1.921418
Point 4: 30mm	1.524942	0.9160874

3.4 Simulating the Dynamic Response of the Cutter and Workpiece

3.4.1 Time Domain Dynamic Model

Once the modal parameters of the machine tool and workpiece are identified, the reaction of each structure to cutting forces can be simulated in the time domain.

FIGURE 3-6: Multiple mode, multiple degree-of-freedom identification

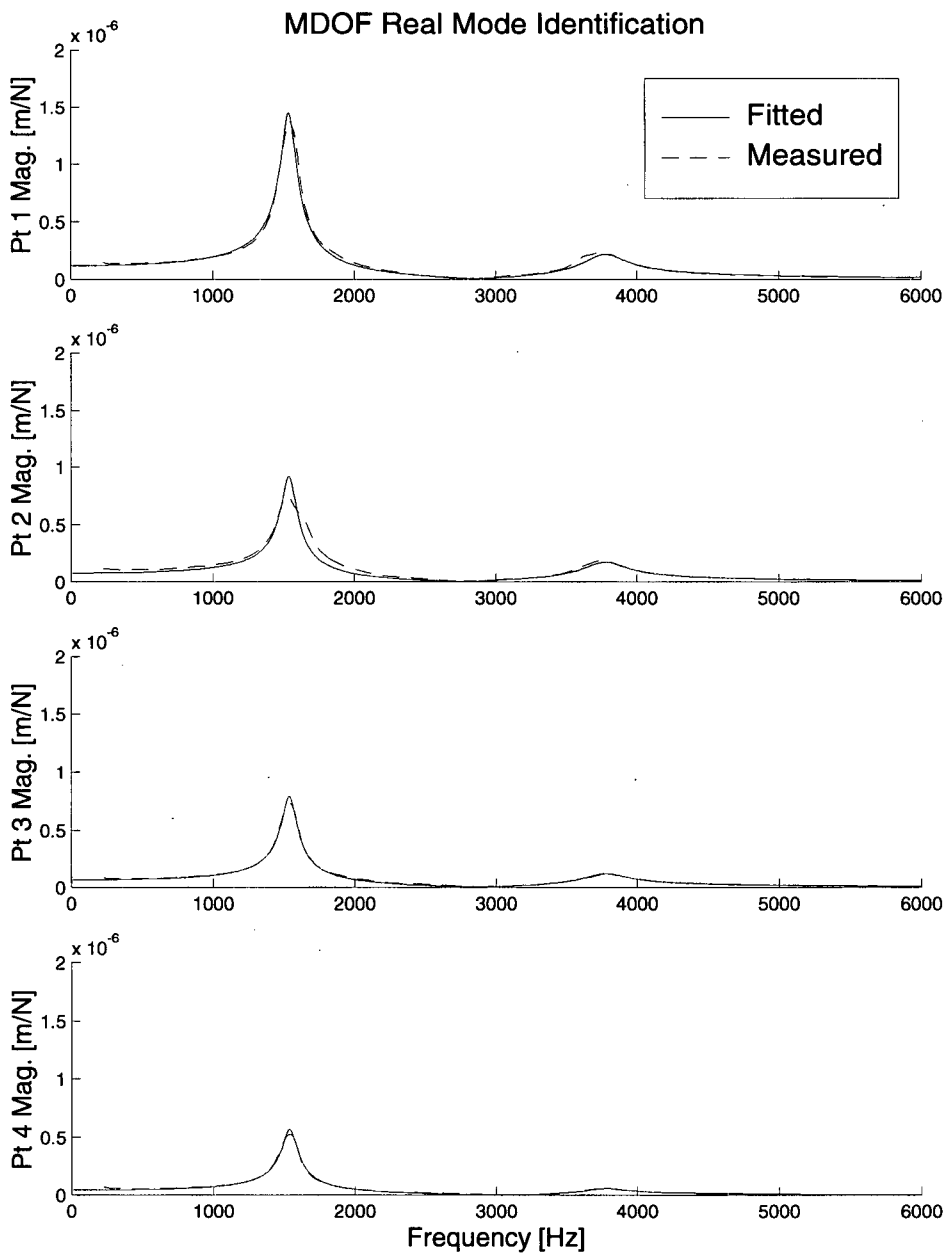

Consider a structure described by the dynamic model defined above. In the Laplace domain, for each mode, k, the response at point p, from an applied force at reference, q, can be expressed in polynomial form as:

$$X_{k,pq}(s) = F_{k,q}(s)\frac{b_o}{s^2 + a_1 s + a_2} \tag{3-26}$$

where,

$$b_0 = u_{k,p}u_{k,q}$$

$$a_1 = 2\zeta_k\omega_{nk}$$

$$a_2 = \omega_{nk}^2$$

This is expressed in continuous state space observable canonical form [63] as the single input, f, and single output, x, system:

$$\begin{bmatrix}\dot{y}_1\\ \dot{y}_2\end{bmatrix} = \begin{bmatrix}0 & -a_2\\ 1 & -a_1\end{bmatrix}\begin{bmatrix}y_1\\ y_2\end{bmatrix} + \begin{bmatrix}b_0\\ 0\end{bmatrix}f$$

$$x = \begin{bmatrix}0 & 1\end{bmatrix}\begin{bmatrix}y_1\\ y_2\end{bmatrix} + 0 \tag{3-27}$$

where y_1 and y_2 are state variables.

Since the response at a point to all applied forces is simply the superposition of N transfer functions with only b_0 varying between the reference points, the total response of each point for each mode may be expanded into the following multiple input, $\{f\}$, single output, x_{kp}, system:

$$\begin{bmatrix} \dot{y}_{1,kp} \\ \dot{y}_{2,kp} \end{bmatrix} = \begin{bmatrix} 0 & -\omega_{nk}^2 \\ 1 & -2\zeta\omega_{nk} \end{bmatrix} \begin{bmatrix} y_{1,kp} \\ y_{2,kp} \end{bmatrix} + u_{k,p}\{u_k\}^T\{f\}$$

$$x_{kp} = y_{1,pk} \tag{3-28}$$

This response function is integrated through time using Runge-Kutta 4th order integration algorithm and the displacement of each mode is superposed to obtain the instantaneous position at each point on the structure.

$$x_p = \sum_{k=1}^{M} y_{1,pk} \tag{3-29}$$

3.4.2 Runge-Kutta 4th Order Integration Algorithm

The Runge-Kutta fourth order formula is by far the most common and most preferred numerical integration algorithm. The algorithm along with computer source code is well described in [64] and [65].

Consider the first part of Equation (3-28) which evaluates the derivatives of y_1 and y_2 for each point and each mode on a structure. The force $\{f\}$ in the milling process is a function of the cutting conditions, which are constant, and the relative position between the cutter and the workpiece, which is a function of the position state variables y_1 and y_2 and of time, t. If these parameters are generalized, letting v_i (i = 1,2,3,...) represent the state variables for all points and all modes on the structures, the time derivative of a state v_i is written as a function of the states and as a function of time:

$$\dot{v}_i = f'(t, v_1, v_2, \ldots) \qquad i = 1, 2, 3, \ldots \tag{3-30}$$

The states at time step $n + 1$ are evaluated based on the states at the previous time step n with the following four stage set of equations:

$$k_{1,i} = \Delta t f'(t_n, v_{n,1}, v_{n,2}, \ldots)$$

$$k_{2,i} = \Delta t f'(t_n + \Delta t/2, v_{n,1} + k_{1,1}/2, v_{n,2} + k_{1,2}/2, \ldots)$$

$$k_{3,i} = \Delta t f'(t_n + \Delta t/2, v_{n,1} + k_{2,1}/2, v_{n,2} + k_{2,2}/2, \ldots)$$

$$k_{4,i} = \Delta t f'(t_n + \Delta t, v_{n,1} + k_{3,1}, v_{n,2} + k_{3,2}, \ldots)$$

$$v_{n+1,i} = v_{n,i} + \frac{k_{1,i}}{6} + \frac{k_{2,i}}{3} + \frac{k_{3,i}}{3} + \frac{k_{4,i}}{6} \tag{3-31}$$

where $i = 1, 2, 3, \ldots$ The last equation above is a weighted sum of the four stages of evaluation. It is important to note that evaluating the function f' during the simulation actually requires several steps. The states must first be converted to position by summing the modes with equation (3-29). Based the relative workpiece and cutting tool position, the cutting conditions, and rotation of the cutter through time, the chip thickness is determined at points along the cutting edge. From the chip load, cutting forces are estimated. The time derivative of the states are then calculated with Equation (3-28). The workpiece-cutting tool interaction described here is discussed in detail in the next chapter.

3.5 Summary

In this chapter, the dynamic model used to describe the cutting tool and the workpiece is defined. An algorithm is outlined which is used to efficiently identify dynamic modal parameters given experimental transfer function measurements at multiple points on the structures. Finally, equations are given to simulate dynamic response from the dynamic model in state space using Runge-Kutta 4th order integration algorithm. These dynamic parameters will be used throughout this thesis in both time domain and frequency domain milling models to predict structural vibrations.

CHAPTER 4

Modelling of Milling Forces

4.1 Overview

This chapter outlines the theory and equations used for modelling milling forces. The cutting force model used is the average linear-edge force model by Budak et al. [15]. For chip thickness evaluation, an improved discretized cutter-workpiece model is presented which provides a more exact kinematics of milling solution. The model features a combination of two algorithms for maintaining the discretized workpiece surface points during the simulation. This will ensure accurate chip thickness calculations even with very small widths of cut and can also provide a 3-D mesh plot of the finished surface. A practical runout model is also included in the simulation. Some experimental results are given of several cutting conditions to support the predicted cutting forces.

4.2 Forces in Milling

The force model used in this thesis is the average-edge force mechanistic model, as detailed in [15]. The geometry and coordinate system is shown in Figure (4-1). The axial (Z) axis is taken from the tip of the cutter with the positive direction towards the spindle. Elemental tangential, radial, and axial forces for tooth j, dF_{tj}, dF_{rj}, and dF_{aj}, along the cutting edge are given by:

FIGURE 4-1: Coordinate system and notation for milling force model

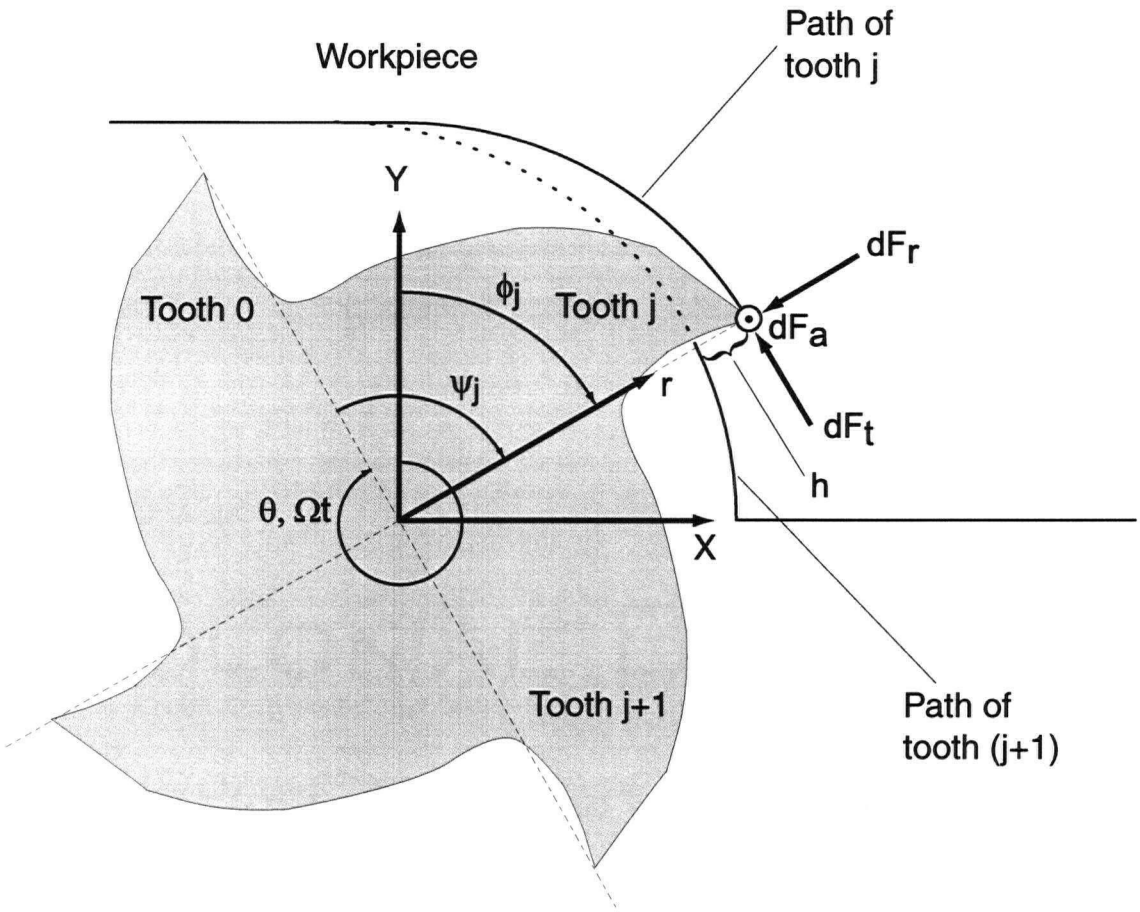

$$dF_{tj} = [K_{te} + K_{tc}h_j]dz$$

$$dF_{rj} = [K_{re} + K_{rc}h_j]dz$$

$$dF_{aj} = [K_{ae} + K_{ac}h_j]dz \tag{4-1}$$

where h_j is the instantaneous uncut chip thickness, and dz is the chip width. For ideal rigid cutter-rigid workpiece and no runout condition, the chip thickness h_j is approximated by $s_t \sin(\phi_j)$, where s_t is the feed per tooth, and ϕ_j is the immersion angle of flute j in radians at axial location z. The immersion angle of flute j at a differential chip element is a function of

cutter orientation, $\theta = \Omega t$, the flutes' angular position relative to a selected reference tooth 0, ψ_j, the helix lag in terms of the helix angle, β, and cutter radius, R, given as:

$$\phi_j = \Omega t + \psi_j - \tan\frac{\beta}{R}$$

Ω is the angular velocity of the cutter in radians per second. For uniform pitch cutters, the relative flute position, ψ_j, is fixed as $\psi_j = \frac{j2\pi}{N}$, where N is the number of teeth.

The forces are modelled in terms of two fundamental phenomena: an edge force component due to rubbing or ploughing at the cutting edge, represented by K_{te}, K_{re}, and K_{ae} on a unit width of cut basis, and a cutting component due to shearing at the shear zone and friction at the rake face, represented by cutting pressure coefficients K_{tc}, K_{rc}, and K_{ac}.

The parameters K_{te}, K_{re}, K_{ae}, K_{tc}, K_{rc}, and K_{ac} are referred to as milling force coefficients and are determined for a specific cutter geometry and workpiece material combination experimentally through cutting tests. A set of slotting experiments are conducted at different feed rates and the average force components are measured in the feed (X), normal (Y), and axial (Z) directions. By developing an analytical expressions for average force per tooth, the force coefficients can be estimated by a linear regression of the experimental data.

To derive average force per tooth equations, the elemental forces of equation (4-1) are first transformed into X, Y, and Z components and integrated along the immersed portion of each flute j, giving:

$$F_{xj} = \frac{R}{\tan\beta}\left[K_{te}\sin\phi_j - K_{re}\cos\phi_j + \frac{s_t}{4}(K_{rc}(2\phi_j - \sin 2\phi_j) - K_{tc}\cos 2\phi_j)\right]\Bigg|_{z_{j,1}}^{z_{j,2}}$$

$$F_{yj} = -\frac{R}{\tan\beta}\left[-K_{re}\sin\phi_j - K_{te}\cos\phi_j + \frac{s_t}{4}(K_{tc}(2\phi_j - \sin 2\phi_j) + K_{rc}\cos 2\phi_j)\right]\Bigg|_{z_{j,1}}^{z_{j,2}}$$

$$F_{zj} = \frac{R}{\tan\beta}[K_{ae}\phi_j - s_t K_{ac}\cos\phi_j]\Big|_{z_{j,1}}^{z_{j,2}} \tag{4-2}$$

where $z_{j,1}$ and $z_{j,2}$ are the lower and upper engagement limits of the in cut portion of flute j. The total force on the cutter at position θ is obtained by summing the contributing forces of each flute.

$$F_x = \sum_{0}^{N-1} F_{xj}$$

$$F_y = \sum_{0}^{N-1} F_{yj}$$

$$F_z = \sum_{0}^{N-1} F_{zj} \tag{4-3}$$

The average forces, $\overline{F_x}, \overline{F_y}$, and $\overline{F_z}$ are determined by integrating equation (4-2) over one complete rotation of the cutter as:

$$\overline{F_x} = -K_{te}S + K_{re}T - \frac{s_t}{4}(-K_{tc}P + K_{rc}Q)$$

$$\overline{F_y} = -K_{te}T - K_{re}S + \frac{s_t}{4}(K_{tc}Q + K_{rc}P)$$

$$\overline{F_z} = -\frac{aN}{2\pi}K_{ae}(\phi_{ex} - \phi_{st}) + s_t K_{ac}T \tag{4-4}$$

where values P, Q, S, and T are defined as:

$$P = \frac{aN}{2\pi}[\cos 2\phi]\Big|_{\phi_{st}}^{\phi_{ex}}$$

$$Q = \frac{aN}{2\pi}[2(\phi - \sin 2\phi)]\Big|_{\phi_{st}}^{\phi_{ex}}$$

$$S = \frac{aN}{2\pi}[\sin\phi]\Big|_{\phi_{st}}^{\phi_{ex}}$$

$$T = \frac{aN}{2\pi}[\cos\phi]\Big|_{\phi_{st}}^{\phi_{ex}} \tag{4-5}$$

ϕ_{st} and ϕ_{ex} are the start and end angles of the cut and a is the axial depth of cut. Since immersion angles and axial depth of cut are kept constant during the cutting tests, the parameters P, Q, S, and T are constants and the average force components can be expressed as a linear function of feed per tooth, s_t, with an offset edge force component as:

$$\overline{F_q} = \overline{F_{qe}} + s_t\overline{F_{qc}} \qquad (q = x, y, z) \tag{4-6}$$

From measured cutting forces at different feed rates, the edge and cutting force components, F_{qe} and F_{qc}, are estimated by linear regression. From equations (4-4) and (4-5), taking the entry and exit angles as $\phi_{st} = 0$ and $\phi_{ex} = \pi$ for slotting, the force coefficients are evaluated from the following relations:

$$K_{te} = -\frac{F_{xe}S + \overline{F_{ye}}T}{S^2 + T^2}$$

$$K_{re} = \frac{K_{te}S + \overline{F_{xe}}}{T}$$

$$K_{ae} = -\frac{2\pi}{aN}\frac{\overline{F_{ze}}}{\phi_{ex} - \phi_{st}}$$

$$K_{tc} = 4\frac{F_{xc}P + \overline{F_{yc}}Q}{P^2 + Q^2}$$

$$K_{rc} = \frac{K_{tc}P + 4\overline{F_{xc}}}{Q}$$

$$K_{ac} = \frac{\overline{F_{zc}}}{T} \tag{4-7}$$

Using Equation (4-1), elemental tangential, radial, and axial forces are reconstructed at any point on the cutter where chip width, *dz*, and chip thickness, *h*, are known. By breaking the cutter into discrete levels, the force distribution along the submersed portions of the cutting edges may be predicted, as shown in Figure (4-2)

FIGURE 4-2: Predicted tangential and radial forces along the cutting edges

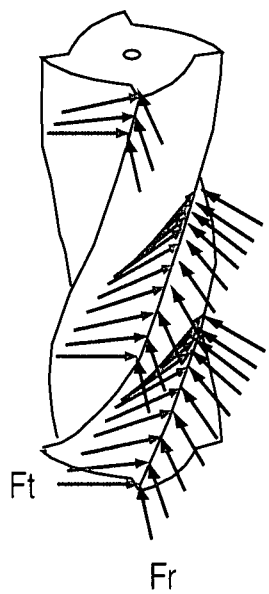

4.3 Surface Generation and Instantaneous Chip Thickness

Since the chip model used in the previous section for estimation of force coefficients is only valid for a rigid cutter-rigid workpiece configuration, an improved model is required in order to simulate milling under conditions in which forces could be dominated by vibrations. Rather than the closed form sinusoidal approximation for chip thickness commonly used, this thesis adopts a model in which instantaneous chip thickness is calculated at discrete time intervals from completely digitized workpiece and cutter surfaces. The exact trochoidal motion of the cutter described by Martellotti [2] is represented. More importantly, this model allows the effect of a flexible workpiece and flexible cutter to be easily considered.

This includes dynamically oscillating chip thickness and changing radial immersion due to deflection and vibrations.

FIGURE 4-3: Digitized cutter and workpiece surface model

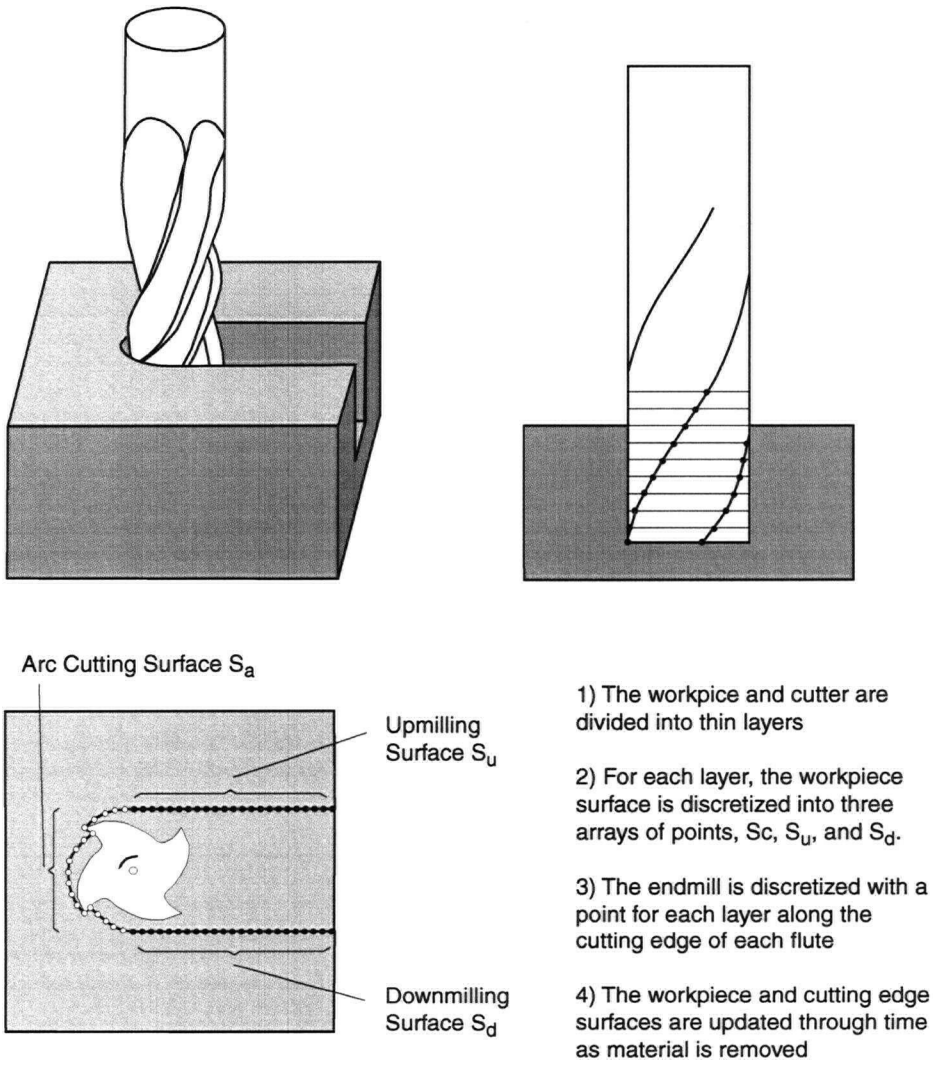

The workpiece surface is first divided into a number of levels. At each level the surface is tracked with up to three arrays of X-Y coordinates. As shown in Figure (4-3), one array, S_a, contains points along the cutting arc of the workpiece. When applicable, the upmilling and

downmilling finished surfaces are tracked using separate arrays S_u and S_d. The points on the surfaces are updated during cutting, and chip thickness is calculated as the difference between the current surface position and the surface left by the previous tooth. All surface arrays are also shifted in the negative X direction at each time interval to account for feed.

Two methods of tracking the surface array can be used. Montgomery [3] used a method in which surface array is updated with the instantaneous angular position of the tooth at each time interval. The radial position of each point is taken as either the radius of the cutter if the tooth is submerged in the workpiece, or as the radial position of the surface left by the previous tooth. This method is shown in Figure (4-4) and will be referred to as Method 1.

FIGURE 4-4: Surface tracking Method 1 (Montgomery & Altintas)

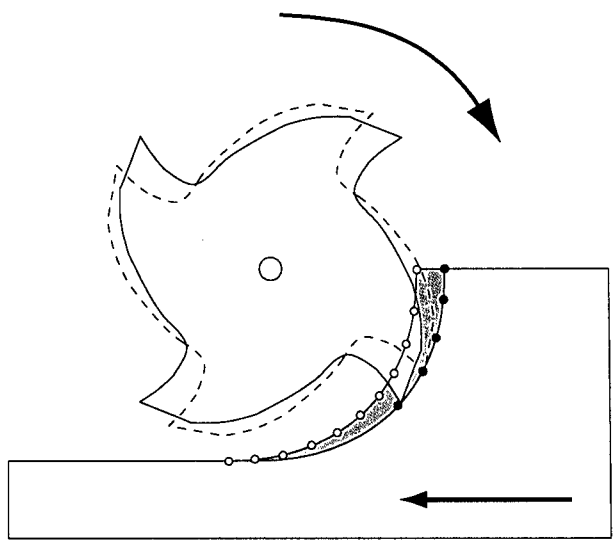

Another method, which will be referred to as Method 2, is one which uses an evenly distributed array of points on the surface which are updated by moving them radially outwards as the tooth cuts into the workpiece, as shown in Figure (4-5). This method, used by Lee [4] is best applicable to more complex geometry cutters such as ballend mills, where radius of the cutter approaches zero at the tip of the cutter. Method 2, however, is not well applicable to

FIGURE 4-5: **Surface tracking Method 2 (Lee)**

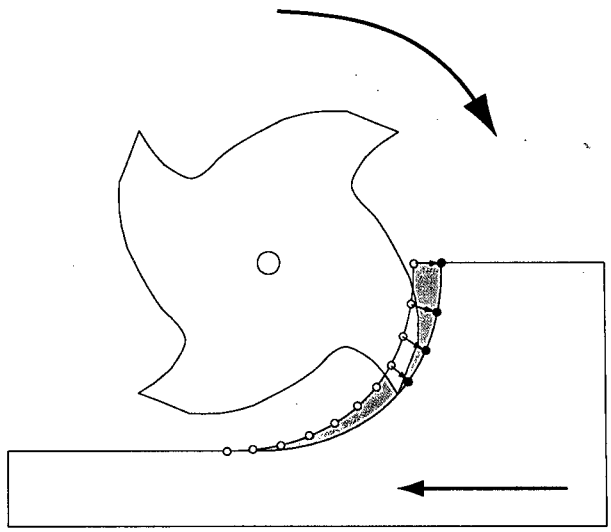

small radial widths of cut or long simulation runs. The radial motion of the points as they are updated by the cutting edge, in combination with the feed in the X direction, caused the points to drift and accumulate, and immersion angles change through time.

The algorithm adopted in this thesis uses a combination of Method 1 for the arc surface, S_a, and Method 2 for best maintaining the history of the finished surfaces, S_u and S_d.

4.3.1 Coordinate Systems

Since the center of the cutter is constantly moving, the points are all stored in Cartesian coordinates with the origin at the non-deflected stationary cutter center, while most calculations are performed in polar coordinates with the origin at the instantaneous center of the cutter. The two coordinate systems are shown in Figure (4-6). For any given point in Cartesian coordinates, (x, y), the following equations are used for converting to a point in the cutter polar coordinate system (r, ϕ):

FIGURE 4-6: Coordinate systems and variable definitions for cutter model

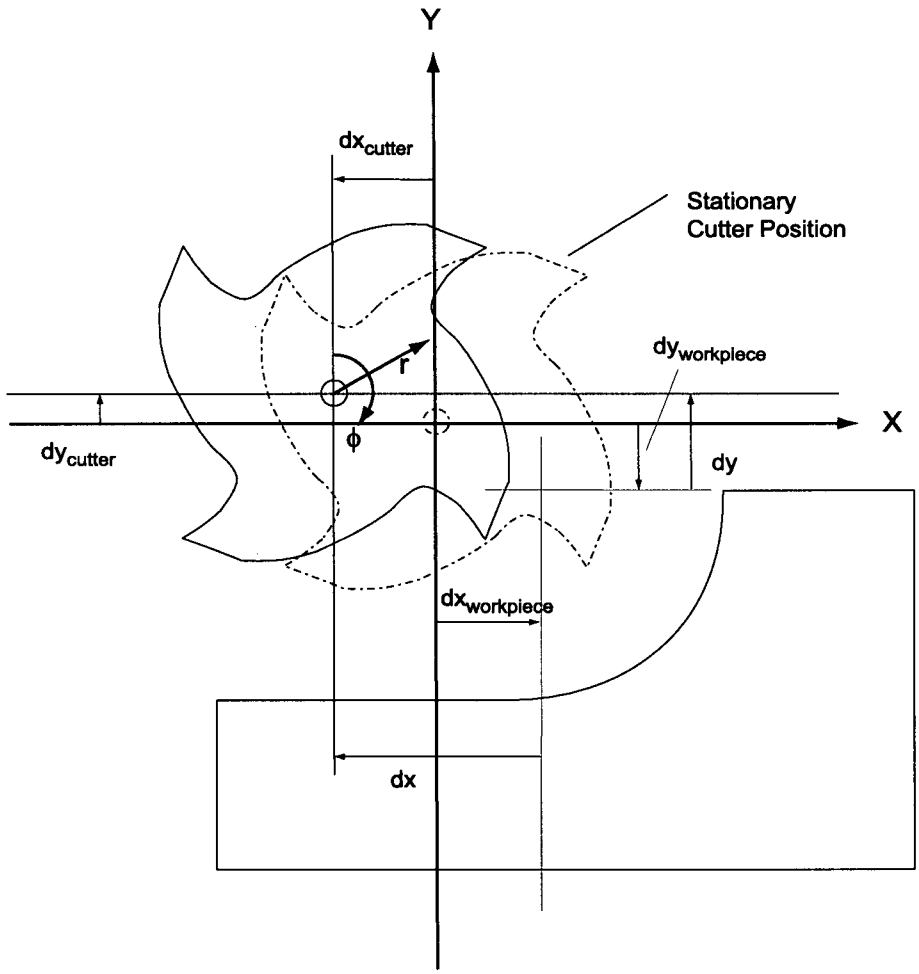

$$r = \sqrt{(x-dx)^2 + (y-dy)^2}$$

$$\phi = \frac{\pi}{2} - \operatorname{atan}\left(\frac{y-dy}{x-dx}\right) \tag{4-8}$$

The atan function is carried out with the `atan2` C function, which ensures the correct quadrant of angle ϕ. dx and dy are the relative displacement components of the cutter with respect to the workpiece due to vibrations and static deflections, calculated as:

$$dx = dx_{cutter} - dx_{workpiece}$$

$$dy = dy_{cutter} - dy_{workpiece} \tag{4-9}$$

4.3.2 Instantaneous Position of the Cutting Edge

At each level of the cutter and workpiece, the position of each tooth is initially defined in the X-Y coordinate system as:

$$x_j = R\sin\phi_j$$

$$y_j = R\cos\phi_j \tag{4-10}$$

where R is the radius of the cutter and ϕ_j is the angular position of the flute as shown in Figure (4-1) and as described in previous sections.

Depending on the type of tool holder being used, runout can become a significant factor influencing peak forces, surface finish, and in extreme cases stability against chatter. The most common form of runout is a parallel axial offset of the cutter center from the rotation axis of the spindle. As a result, the flutes on the offset side of the tool holder have a larger effective radius than those on the opposite side. The effects of axial offset runout on force and geometry is investigated in detail by Kline and DeVor [53]. As shown in Figure (4-7), runout can be modelled with an offset parameter, ρ, and an angular orientation angle, λ, relative to the position of the flutes. Two additional parameters, τ and δ, are also shown, which may be included to model the magnitude and orientation of any axis tilt of the cutter with respect to the spindle.

The model described above is ideal for studying the effects of various runout parameters. However, when simulating an actual existing cutter-spindle setup, these parameters can be difficult to measure. The main purpose of including runout in this thesis is for better comparison of simulation results to measured cutting data. A more practical approach to modelling runout is taken here, which focuses on ease of runout measurement for existing equipment. The effect of runout is modelled with an additional correction term, r_r, added to the radius of the cutter. Multiple radial offset measurements are taken along the axial length

FIGURE 4-7: Parallel axis and axis tilt runout models

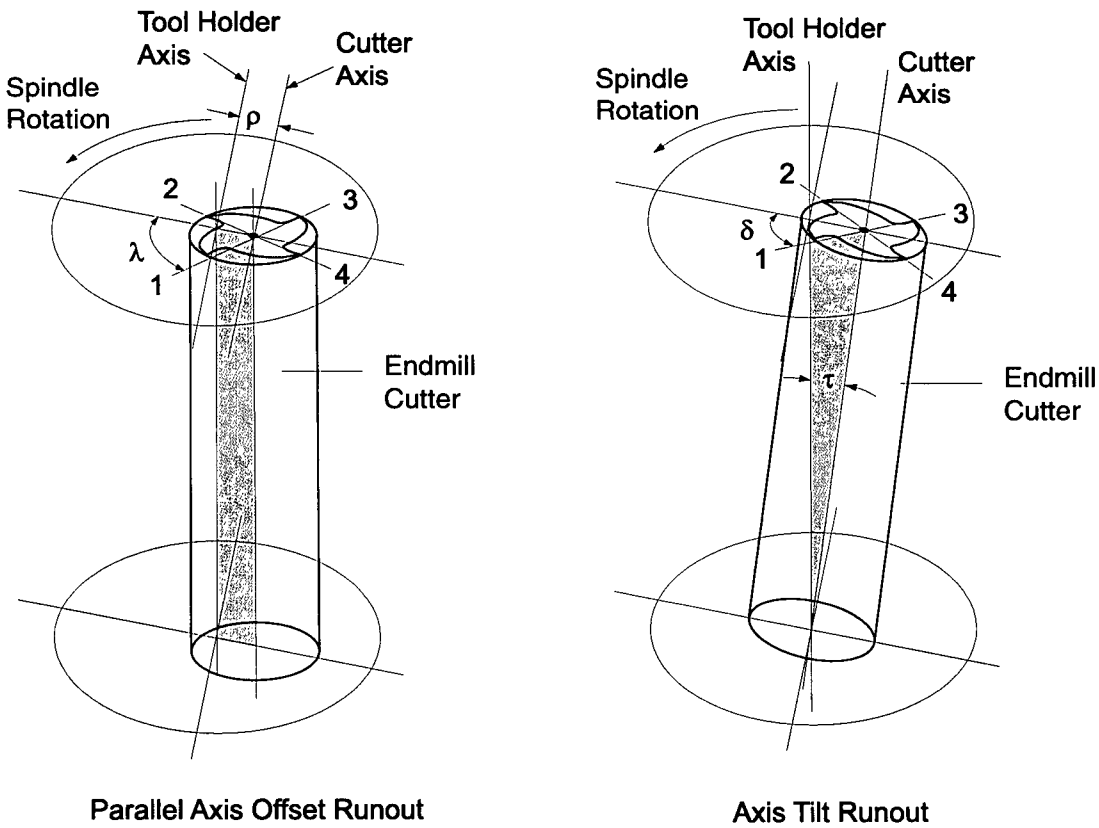

for each flute using a dial gauge, as shown in Figure (4-8). The dial gauge zero position is set to the average radius measurement taken at the cutter shank near the tool holder. Runout between these measurements are obtained by linear interpolation of radius offsets, giving a continuous runout value r_r for each flute as a function of axial position, z. The tooth position with the added runout may be expressed as:

$$x = (R + r_r)\sin\phi_j$$

$$y = (R + r_r)\cos\phi_j \qquad (4\text{-}11)$$

By using measured flute offset positions along the length of the cutter, any possible source of runout will be accounted for.

FIGURE 4-8: Apparatus for measuring cutter runout

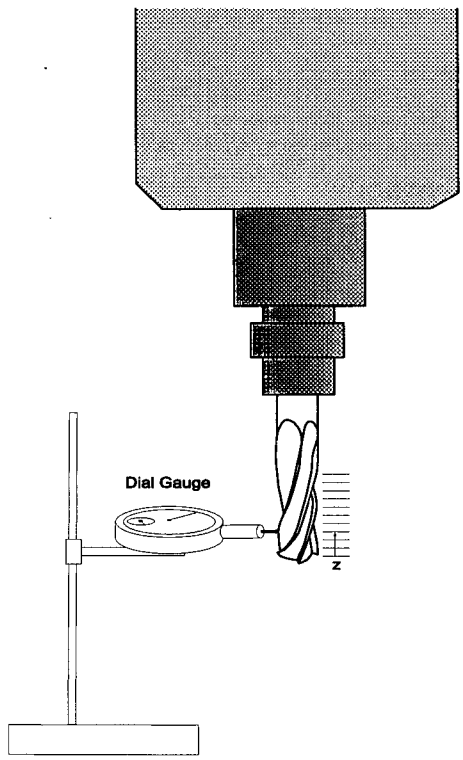

4.3.3 Arc Cutting Surface

The array of points on the arc of the cutting surface is maintained by a procedure similar to that used my Montgomery [3]. Two surface arrays are stored, one of the surface left by the previous tooth and one being created by the current tooth. Figure (4-9) shows how the surface array is updated. At each time interval, a new point (x_i, y_i) is added to the current surface at the angular position of the tooth, ϕ_i. If the tooth is cutting, the instantaneous position of the tooth tip is used, otherwise a point is found on the previous surface at the tooth angle ϕ_i.

FIGURE 4-9: Updating current arc surface array

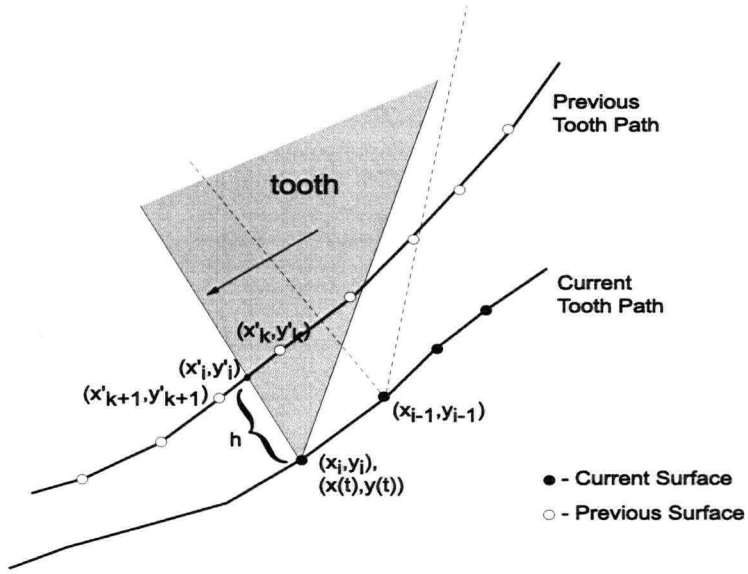

Tooth Submersed in Workpiece

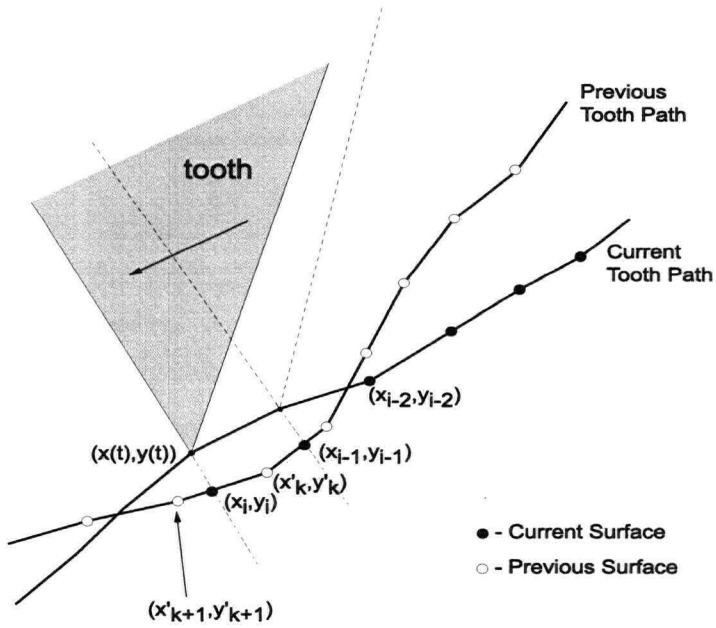

Tooth Separated from Workpiece

In order to determine if the tooth is submersed in the workpiece, the intersection point of the tooth and the previous surface is calculated. The point on the previous surface, (x'_k, y'_k), is found which has an angular position, ϕ_k, immediately preceding the angular position of the tooth, ϕ_i. The intersection point (x'_i, y'_i) is then found by linear interpolation of the radial distance between points k and $k+1$ on the previous surface. In polar coordinates, the intersection point, (ϕ'_i, r'_i) is given as:

$$r'_i = \frac{r'_{k+1} - r'_k}{\phi'_{k+1} - \phi'_k}\phi_i \tag{4-12}$$

If the effective radius of the cutter is greater than r'_i then the tooth is cutting and the chip thickness is calculated as:

$$h = R + r_r - r'_i \tag{4-13}$$

where R is the radius of the cutter and r_r is the cutter runout. In this case, the new point (x_i, y_i) is taken as the instantaneous position of the tooth tip, $(x_j(t), y_j(t))$. Otherwise, if r'_i is less than the effective cutter radius, the tooth has separated from the workpiece. The chip thickness is set to 0 and the new point (x_i, y_i) is assigned the value of (x'_i, y'_i) on the surface left by the previous tooth pass.

4.3.4 Upmilling and Downmilling Finished Surfaces

The upmilling and downmilling surface arrays are maintained in a different way than the arc surface for two main reasons. First, since the finished surface is flat, as points feed away from the cutter, the density of points would decrease if they were distributed according to the angular position of the tooth at each time interval. Secondly, the finished surface is affected by a tooth only at the instant it passes through $\phi = 0$ or $\phi = \pi$. Feed or chatter marks left on the surface could be extremely small and must be tracked using a much denser array of points than that used for the arc surface.

FIGURE 4-10: Updating finished surface array

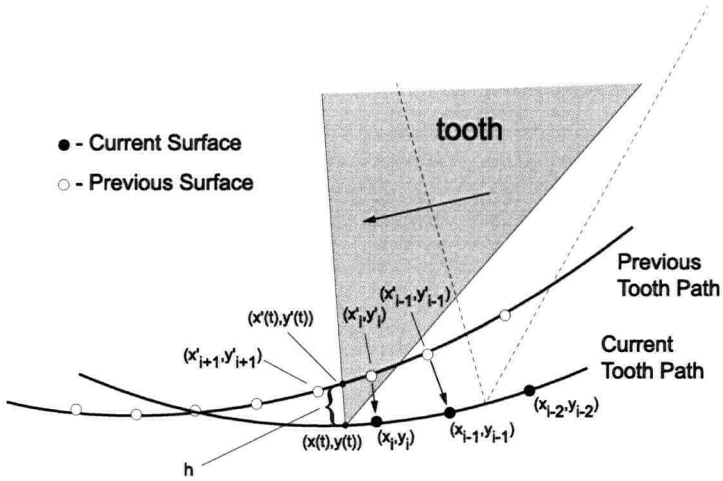

Tooth Submersed in Workpiece

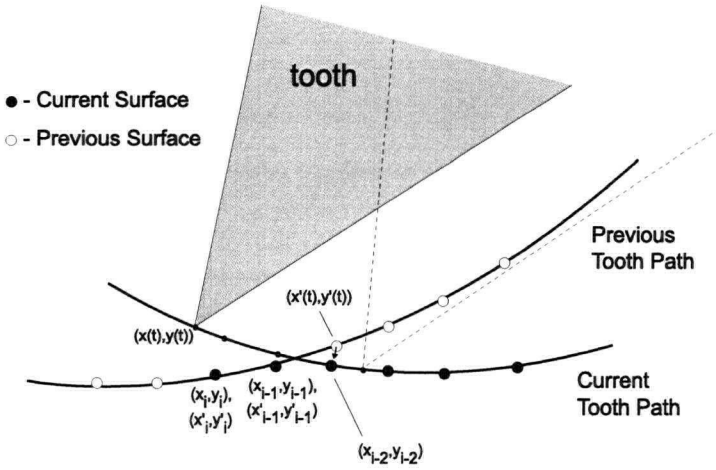

Tooth Leaving Workpiece

Figure (4-10) shows how the upmilling and downmilling finished surfaces are maintained in the simulation. As the tooth passes from its previous position, all points which lie between the angles $\phi_j(t)$ (current tooth position) and $\phi_j(t-\Delta t)$ (previous tooth position) are updated if the tooth is cutting.

Consider point i on the surface left by the previous tooth which is being passed by the current tooth during time interval Δt. If it's radial position, r'_i is smaller than the effective cutter radius, the tooth is cutting and the point is moved radially outward as $r_i = R + r_r$ to form the new current surface. The angular position of each point, ϕ_i, is kept fixed. A point is not added on the new surface at the tip of the tooth as with the arc surface. The only calculations done at the tip of the tooth are for the purpose of determining the chip thickness.

To calculate the instantaneous chip thickness, the intersection point of the tooth with the previous surface is calculated. As with the arc surface, the point on the previous surface, (x'_k, y'_k), is found which has an angular position, ϕ'_k, immediately preceding the angular position of tooth j, $\phi_j(t)$. The intersection point $(x_j'(t), y_j'(t))$ is then found by linear interpolation of the radial distance between points k and $k+1$ on the previous surface:

$$r_j'(t) = \frac{r_{i+1} - r_i}{\phi_{i+1} - \phi_i}\phi_j(t) \tag{4-14}$$

If the effective radius of the cutter is greater than $r_j'(t)$, the tooth is cutting and the chip thickness is calculated as:

$$h = R + r_r - r_j'(t) \tag{4-15}$$

where R is the radius of the cutter and r_r is the cutter runout. Otherwise, the tooth is not submersed in the workpiece and a chip thickness of $h = 0$ is taken.

Using this algorithm, a relatively constant density of points can be maintained. Furthermore, the distribution of the points is not dictated by the time interval, so a much denser array of points can be used if required.

4.3.5 Special Cases

When applying the two algorithms above, there are a few special cases which must be considered when the tooth is just entering or exiting some of the surface arrays.

The first of these cases is when entering or exiting the arc surface. If entering or exiting the surface at an angle other than $\phi = 0$ or $\phi = \pi$, then a point is added to the new surface array to mark the boundary of the workpiece. Consider the time step shown in Figure (4-11) for down milling. The first point in the new surface array is the intersection point between the line $y = y_{enter}$ and the tooth path. The second point is that at the tip of the tooth. The chip thickness is found as usual with Equation (4-13).

A second issue must be addressed in the case when downmilling at small radial immersions and large feed rates. There is no upmilling surface and the tooth enters the arc surface directly at such an angle that the tooth first strikes the upper uncut workpiece surface before cutting the surface cut by previous teeth. The chip thickness is found using Equation (4-13), with the point (x'_i, y'_i) found as intersection between the tooth edge and the line $y = y_{enter}$, as shown in Figure (4-12).

When entering or exiting the surface at $\phi = 0$ or $\phi = \pi$, a point must be added on the new surface to mark the boundary of the arc surface, where the upmilling or downmilling surface begins. The procedure is analogous to that described above for Figure (4-11), except that the intersection point between the tooth and the line $x = 0$ is used.

FIGURE 4-11: Updating arc cutting surface array with tooth completely entering the cut

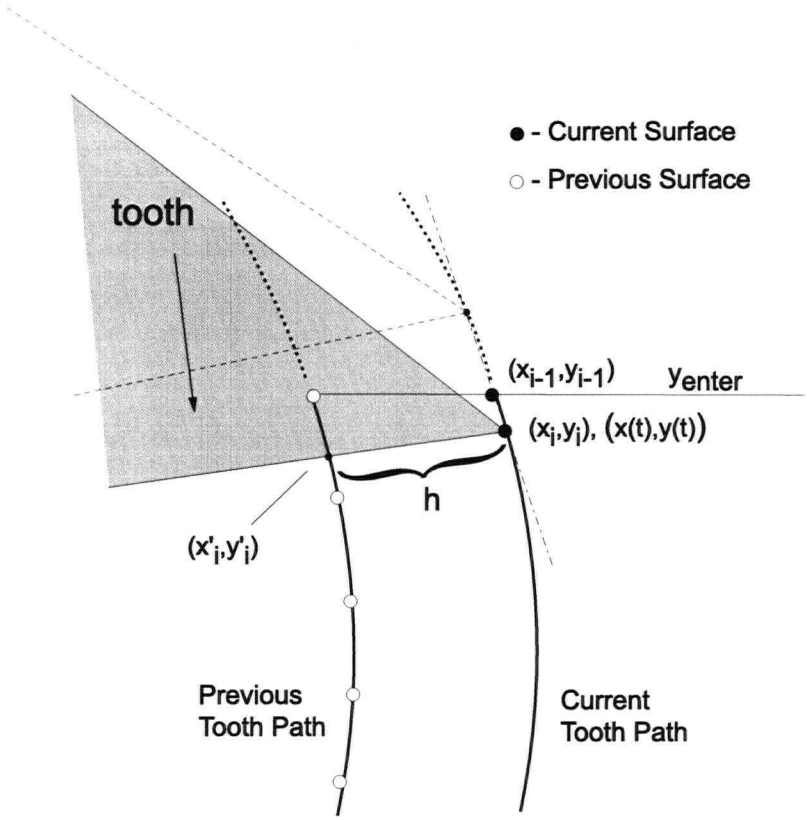

Tooth Entering Arc Surface

4.3.6 Feeding The Workpiece

The workpiece is fed into the cutter at the rate s_t [mm/tooth]. With a spindle speed, n, a time interval of Δt, and N number of teeth, the motion of the workpiece along the X-axis during a single time step is:

$$\Delta x = -s_t N \frac{n}{60} \Delta t \tag{4-16}$$

FIGURE 4-12: Updating arc cutting surface array with tooth partially entering cut

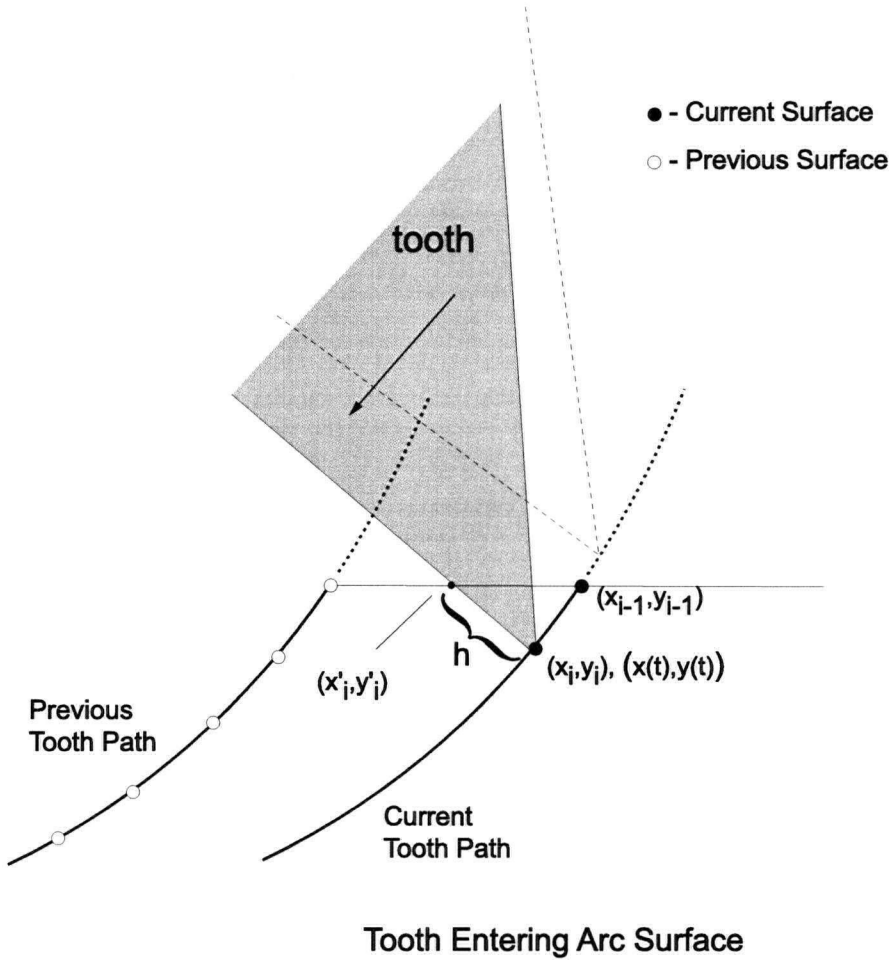

The X component of all points in all surface arrays are incremented by Δx at each time step before the surface is updated due to the teeth cutting. The new intersection points of the arc surface with the $x = 0$ border must be calculated. Points are added to the upmilling and downmilling surface at this intersection point at a time interval based on the desired density of the points.

4.4 Experimental Verification of Cutting Force and Chip Model

In order to verify the cutting force model and the chip thickness algorithms used in the simulation, some static cutting tests are performed. The axial depth of cut is kept well below the chatter limit and measured forces are compared to simulation results using a rigid workpiece-rigid cutter model.

The cutting coefficients are obtained as described in Section 4.2. Cutting forces in the X and Y directions are measured using a Kistler force dynamometer. Slot milling tests are conducted at 1.5 mm axial depth of cut in aluminum alloy Al7075-T651. The cutting tool is a 3/4 inch diameter carbide helical endmill with a 30 degree helix. The forces are measured for feed a spindle speed of 2000 RPM and feed rates from 0.0125 to 0.125 mm/tooth (100 mm/min to 1000 mm/min) The average forces are calculated and plotted in Figure (4-13). The corresponding cutting force coefficients, are shown in Table (4-1). Runout was also measured at several points along the axial length of the cutter for each flute and the results are listed in Table (4-2). Using a dial gauge, measurements were taken with a one micron accuracy, which is sufficient for the tests conducted here.

TABLE 4-1: Cutting Force Coefficients from Slotting Tests

K_{te}	12.508356 N/mm
K_{tc}	947.86792 N/mm^2
K_{re}	13.679662 N/mm
K_{rc}	288.665009 N/mm^2
K_{ae}	1.810814 N/mm
K_{ac}	223.586685 N/mm^2

TABLE 4-2: Runout Measurements

z [mm] (from tip of cutter)	Flute 1 [μ m]	Flute 2 [μ m]	Flute 3 [μ m]	Flute 4 [μ m]
1.5	2	10	0	-9
5.0	2	10	1	-7
10.0	0	10	4	-7
15.0	0	9	5	-7
20.0	-2	9	6	-4

FIGURE 4-13: Measured Cutting Forces in X, Y, and Z directions for Slotting Tests

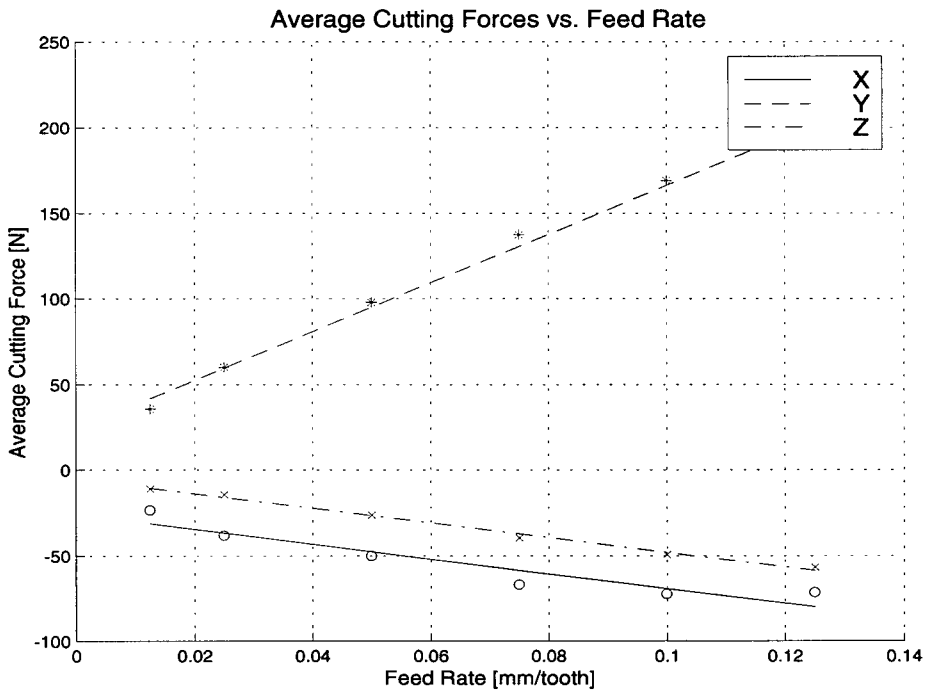

TABLE 4-2: Runout Measurements

z [mm] (from tip of cutter)	Flute 1 [μ m]	Flute 2 [μ m]	Flute 3 [μ m]	Flute 4 [μ m]
25.0	-2	8	7	-1
30.0	-3	6	7	-1

The force and chip models have been implemented into a working PC based simulation software. The predicted X and Y forces for several cutting conditions are shown below. First, Figure (4-14) compares measured versus simulated forces for a slotting tests above. Since the force coefficients are determined from a linear least squares fit of these experimental tests, the very close agreement is expected. Note, however, that while runout is included in the simulation, it was not included for evaluating the force coefficients. The results below show how runout can significantly affect the cutting forces.

Figures (4-15) and (4-16) show good agreement of measured versus simulated results while milling with smaller widths of cut (as low as 0.5mm), and larger depths of cut (as large as

30.0mm). It is evident that most of the discrepancy between experimental and simulated forces is due to inaccurate runout measurements. In general, the cutting force and kinematic models provide acceptable accuracy in predicting milling forces.

FIGURE 4-14: Simulated and Measured X/Y forces - slotting, a=1.5mm, feed=0.1mm/tooth, n=2000RPM

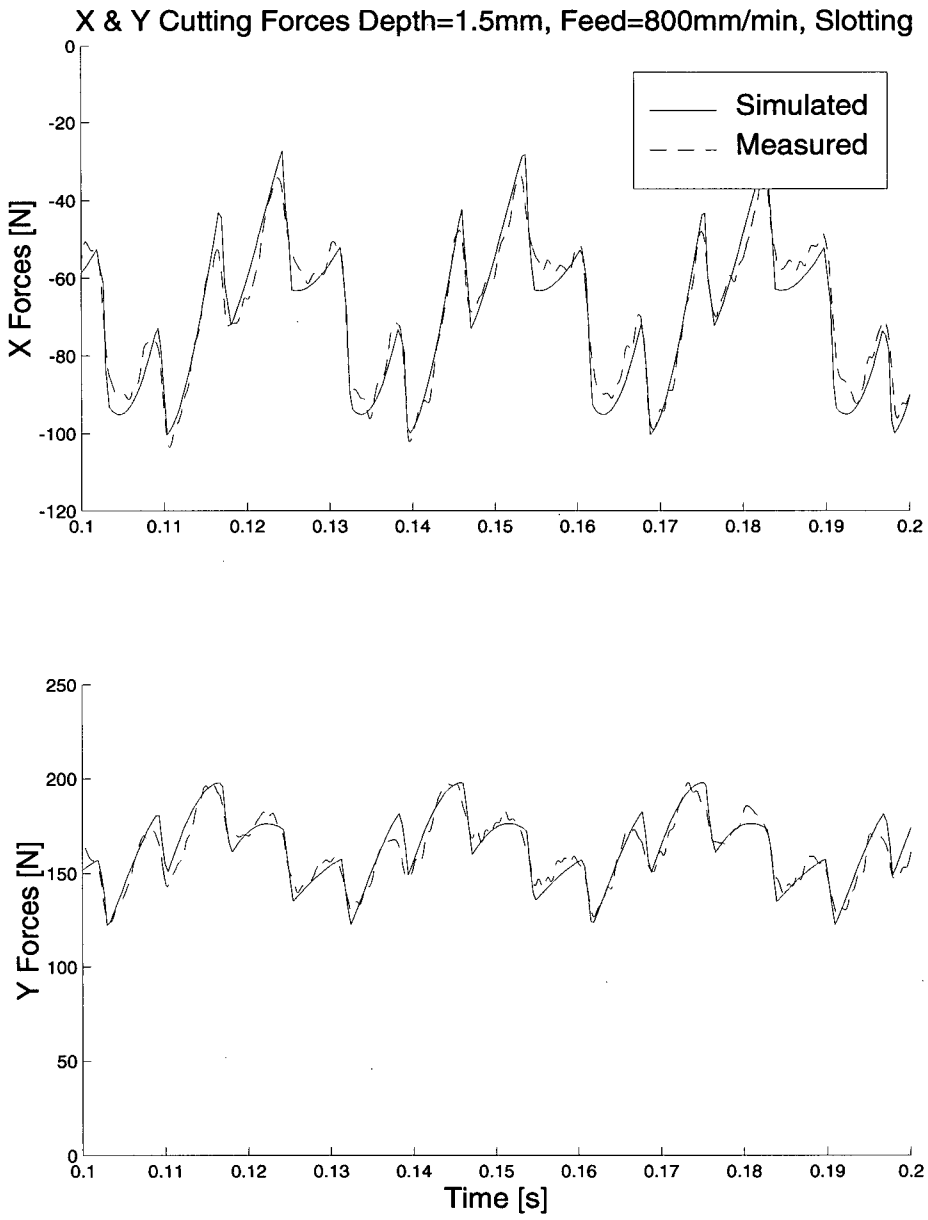

FIGURE 4-15: Simulated and Measured X/Y forces - downmilling width of cut=0.5mm, a=25.0mm, feed rate=0.2mm/tooth, n=2000RPM

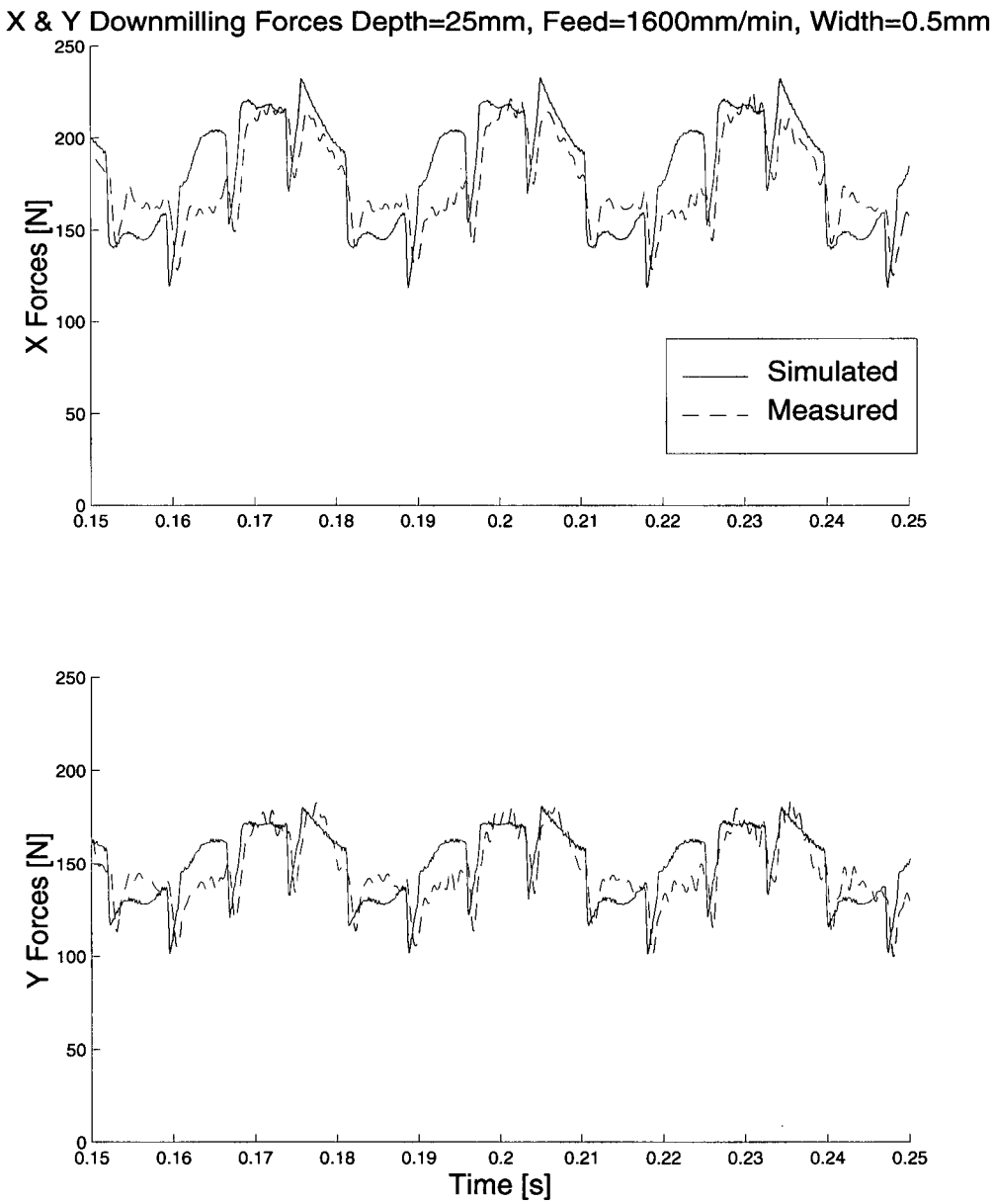

FIGURE 4-16: Simulated and Measured X/Y forces - downmilling width of cut=1.0mm, a=30.0mm, feed rate = 0.05mm/tooth, n=2000RPM

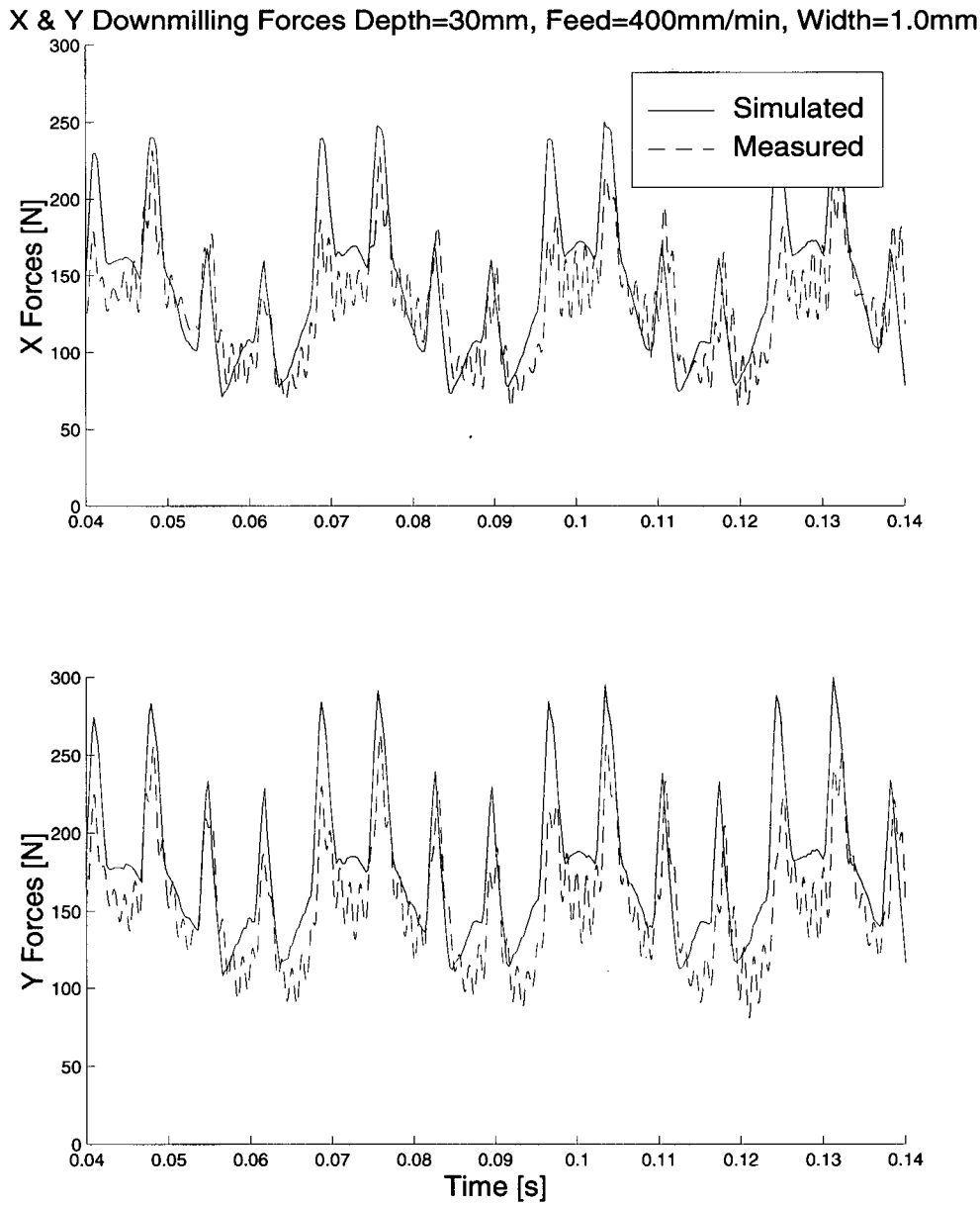

CHAPTER 5

Chatter Stability in Milling

5.1 Introduction

Avoidance of chatter in machining is critical to ensure proper tolerances, and to prevent excessive vibrations, which lead to poor surface finish, and could damage the cutter, the machine tool, or the workpiece. Often in practice, chatter is avoided by using cutting conditions which typically result in more conservative metal removal rates and lower productivity. Knowing the precise limits of cutting conditions before chatter occurs has been the efforts of many machining researchers.

The most common form of displaying chatter stability limit has been the *chatter stability lobes*. For a given cutting condition, axial depth of cut limit is plotted versus spindle speed.

In this chapter, stability lobes are predicted by two methods: from time domain simulations and from a frequency domain model. While stability lobes from the time domain model provide more realistic results, the long simulation time makes this method impractical. A new frequency domain stability lobe model is discussed here which accounts for the main source of chatter (wave regeneration). The previously unreported effect of feed rate on the regeneration effect is also investigated and included in the model.

5.2 Determining Chatter Stability Lobes from Time Domain Simulations

The time domain simulation outlined in the preceding chapters includes all the necessary effects to model chatter, with the exception of process damping at lower spindle speeds. Wave regeneration and mode coupling are both included, which are the two main mechanisms causing chatter. The exact kinematics of milling is used, which includes the effects of feed and the non-linearity of the cutter separating from the workpiece.

For a single time domain simulation, it is usually quite obvious whether or not the conditions are unstable by visually inspecting the program output for excessively large vibrations and forces. However, in order for the program to automatically scan through a range of spindle speeds and search for the axial depths of cut limit, a reliable mathematical algorithm must be developed for this procedure.

The chatter stability criteria used in this thesis for time domain simulations relies on predicted dynamic chip thickness at all cutting points on the cutter. Under chatter conditions, vibrations become unstable, but the magnitude of the vibrations are eventually limited by the cutting tool jumping out of the workpiece. The maximum dynamic chip thickness is found during this steady-state chatter condition. This value is normalized by dividing by the maximum uncut chip thickness during a static milling simulation, giving a non-dimensional chatter parameter, η. Until this parameter exceeds a pre-defined limit, the process is considered chatter-free.

Using the following steps, the stability lobes are evaluated by finding the axial depth of cut limit through a range of spindle speeds:

1. Machine dynamics, workpiece dynamics, cutting tool geometry, feed rate, cutter orientation and immersion, workpiece material, and a starting axial depth of cut, a, are specified.
2. A range of spindle speeds and a spindle speed step size are specified.

3. For a given spindle speed, a static time domain simulation is run (suppressing any workpiece and cutter vibrations) and the maximum static uncut chip thickness, $h_{s,\,max}$, is stored. For uniform pitch endmill cutters with no runout, this is equal to the feed per tooth, s_t.

4. A second time domain simulation is run using a flexible workpiece-flexible cutter model until a steady-state chatter condition is reached. The largest dynamic chip thickness of all cutting points on the cutter, $h_{d,\,max}$, is stored for the last few revolutions of the simulation.

5. The non-dimensional chatter parameter, η, is evaluated as:

$$\eta = \frac{h_{d,\,max}}{h_{s,\,max}} \tag{5-1}$$

6. If η is greater than a pre-determined limit (1.1 is used in this thesis), the process is unstable, otherwise the process is chatter-free. Note that excessive forced vibrations may also trigger a "chatter" condition.

7. If the process is stable, a_{min} is set to the current value of a. a is doubled and steps 3-6 are repeated until chatter occurs. Then a_{max} is set to the value of a when chatter occurred.

   If the process is not stable, a_{max} is set to the current value of a. a is halved and steps 3-6 are repeated until the process is stable. Then a_{min} is set to the stable depth of cut, a.

8. Once the range a_{min} to a_{max} is found between which the axial depth of cut limit lies, a bisection search is performed with $a_{min} > a > a_{max}$, repeating steps 3-6 until the axial depth of cut limit, a_{lim}, is found within a given tolerance, ε.

Predicted stability lobes using this algorithm for a half-immersion downmilling case is shown in Figure (5-1). A four fluted endmill is used with dynamic parameters: ω_x = 500

FIGURE 5-1: Stability lobes evaluated from time domain simulations

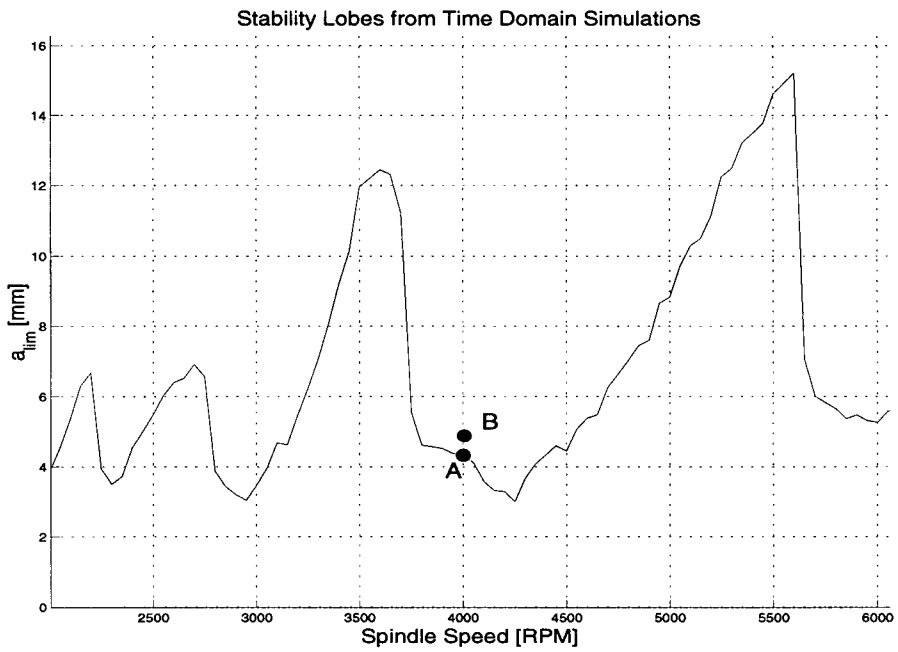

Hz, ω_y = 700 Hz, k_x=k_y=1e6 N/m, ζ_x=ζ_y= 0.05. The material is Aluminum Al7075. Examining several points around the stability limit, demonstrates the algorithm's effectiveness. Figures (5-2) and (5-4) show the forces and vibrations just at the stability limit, while Figures (5-3) and (5-5) show the unstable condition just above the stability limit. At stable conditions, the FFT of the vibrations show that dominant frequencies are at the harmonics of the tooth frequency, 300 Hz. When chatter develops, the natural frequencies (500 Hz in the X direction and 700 Hz in the Y direction) become more dominant. The forces and vibrations grow to a higher steady-state level where the system stabilizes only due to the cutter separating from the workpiece.

An alternate stability criteria for determining stability in time domain simulations, such as the one used by Lee [4], is to use predicted peak-to-peak cutting forces or peak-to-peak cut-

FIGURE 5-2: X/Y forces for conditions at point A: a = 4.5 mm, n = 4000 RPM

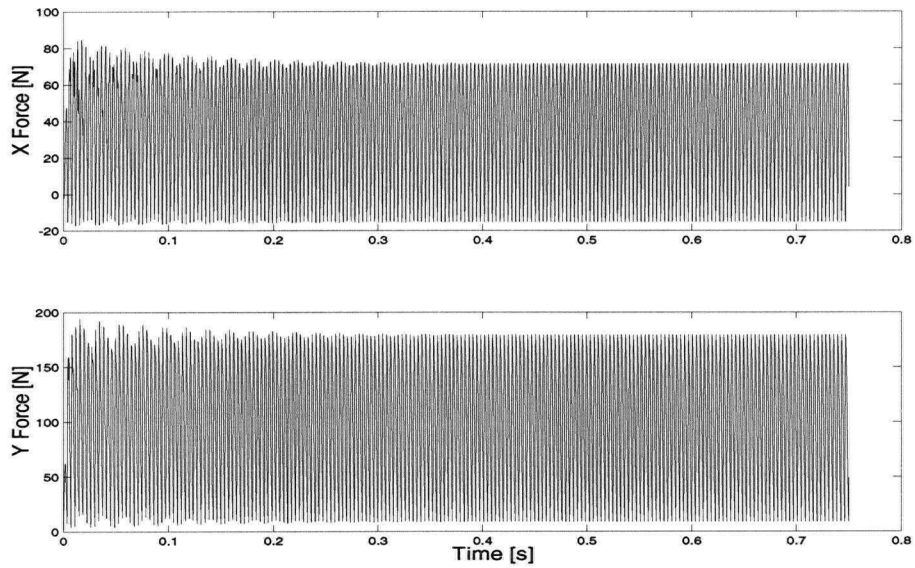

FIGURE 5-3: X/Y forces for conditions at point B: a = 5.0 mm, n = 4000 RPM

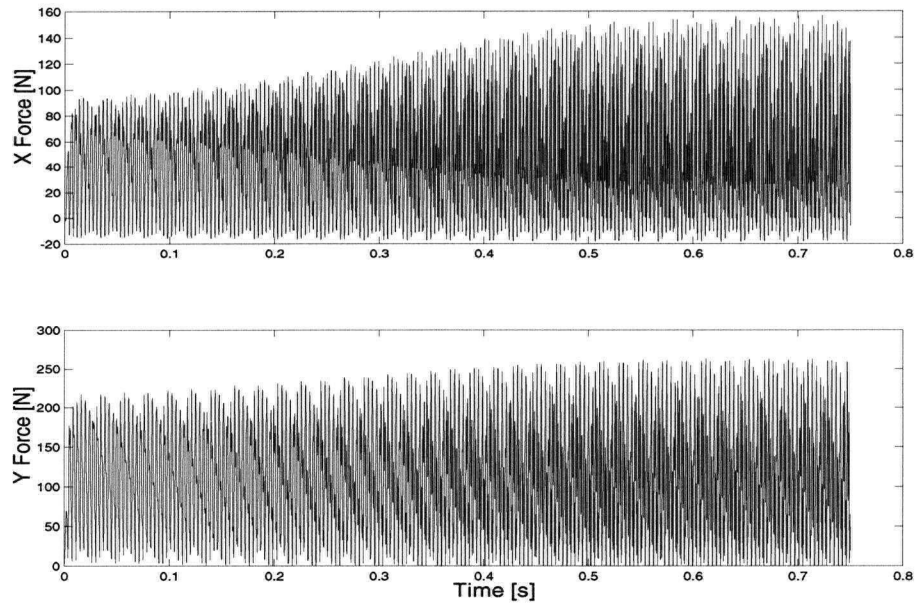

FIGURE 5-4: X and Y vibrations for conditions at point A: a = 4.5 mm, n = 4000 RPM

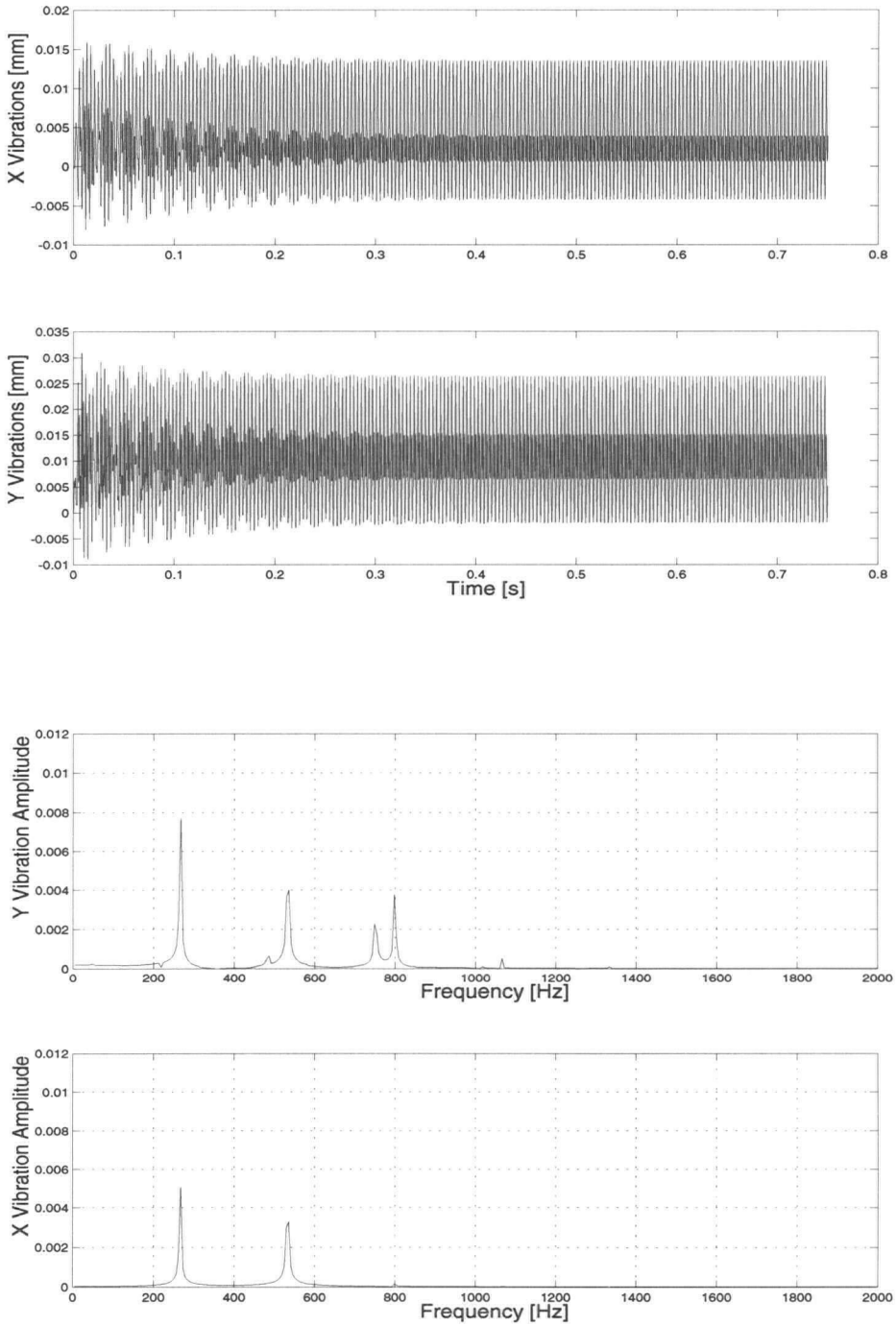

FIGURE 5-5: X and Y vibrations for conditions at point B: a = 5.0 mm, n = 4000 RPM

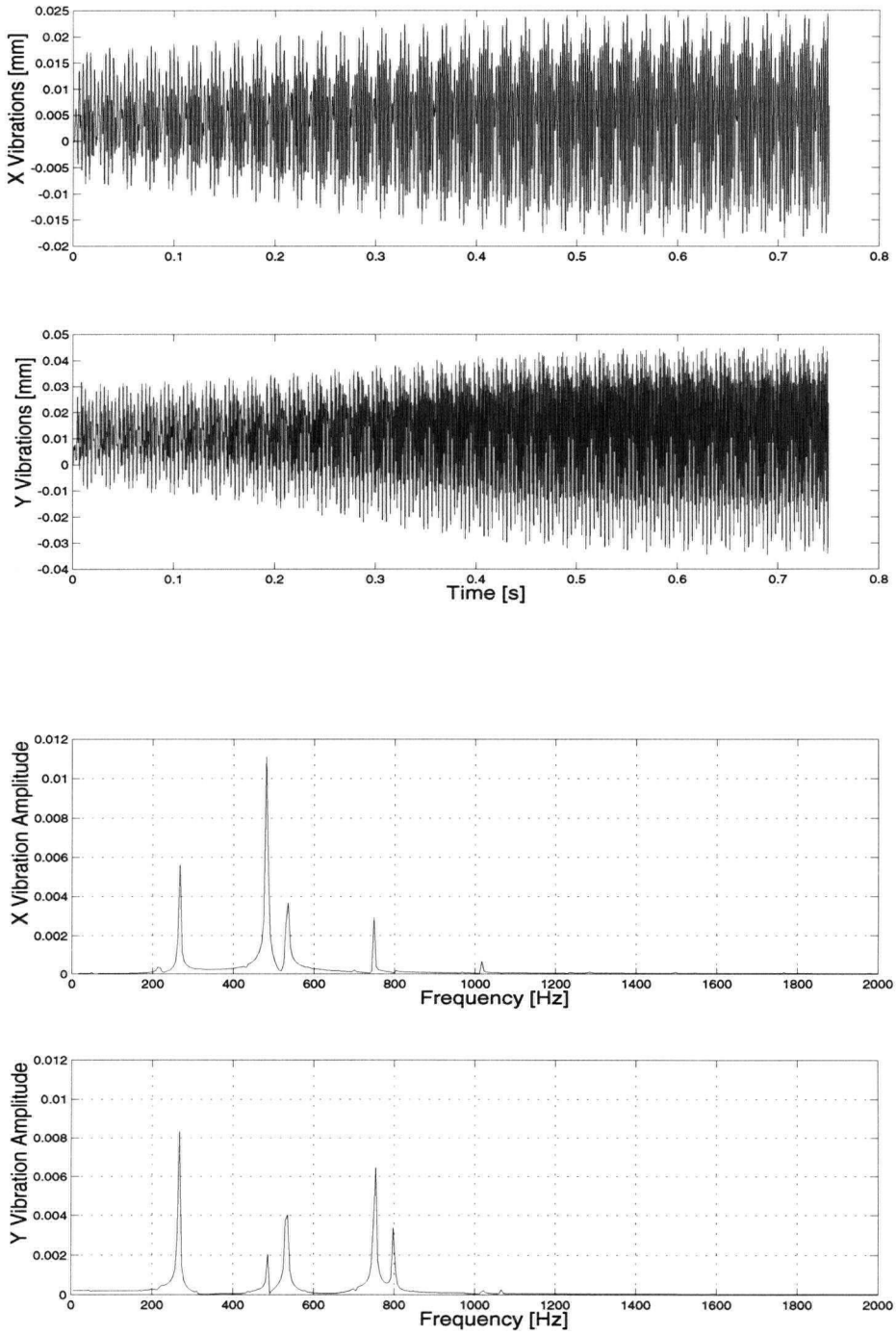

ter and workpiece vibrations. However, the AC component of predicted X and Y forces may not accurately detect chatter in conditions such as slotting, when radial and tangential forces may cancel in the transformation from polar to Cartesian coordinates. Also, tangential forces may have a smaller AC component during slotting with a multiple tooth cutter, when vibrations can cause an increasing chip thickness for one tooth, while decreasing chip thickness for another. Using vibrations to detect chatter can lead to difficulties in separating chatter from large forced vibrations and static deflections. These conditions may result in an artificially large or artificially small chatter parameter, η, giving inaccurate stability lobes. The chatter parameter calculated above from maximum uncut dynamic and static chip thicknesses, offers a more consistent measurement. This criteria best reflects chip thickness variations caused by chatter, while filtering out most effects of forced vibrations and static deflection.

5.3 Increased Stability Against Chatter at Lower Spindle Speeds

At lower spindle speeds with relatively higher frequency vibration modes, an increased stability has been noted in practice. This stability increase in most works to date is attributed solely to *process damping*. A comprehensive explanation of this effect was provided by Sisson and Kegg [29], who describe the process damping in turning in terms of physical quantities such as tool edge roundness, tool clearance angles, and chatter frequency. Later works [30][31][32] describe process damping as being primarily caused by the varying relief angle of the cutting tool due to vibrations. In general, the theory behind process damping is very qualitative and most attempts to model this effect have relied heavily on experimentally determined coefficients, in which case the predictions are restricted to limited cutting conditions.

This increased stability at low spindle speeds has also been noticed in the time domain simulation used in this thesis, which does not include the effect of process damping. In Figure (5-6), for example, the stability lobes are predicted from time domain simulations for down milling a flexible plate with a natural frequency of 1000 Hz with a rigid cutter with a feed

rate of 0.5 mm per tooth. There is an increasing stability at lower spindle speeds. This effect becomes greater with increasing feed rate.

Hence, another mechanism must exist which affects stability in this range. In the next section, a frequency domain model for evaluating stability lobes is discussed. A newly reported phenomenon is explained and simulated, which can have an extremely important role in increasing stability at lower spindle speeds. This phenomenon is based on the effect of feed rate on wave regeneration. This does not replace process damping, which undoubtedly exists, from noted trends in turning. Rather it is a contributing effect to the increase in stability at lower spindle speeds. Its neglect in past works can be a critical factor explaining the limited success achieved in modelling this effect in milling.

5.4 Evaluating Stability Lobes from Frequency Domain Model

Time domain simulations can very accurately determine chatter stability limits, taking into account many non-linear effects which are difficult to model in any closed form mathematical model. However, the calculations involved can be computationally expensive. The time domain simulations for calculating the stability lobes in Figure (5-6), for example, took several days of computation on a Pentium II 266 MHz processor. Furthermore, time domain simulations offer little theoretical explanation for the resulting predictions.

Chatter theory is explained here in detail and a frequency domain mathematical model is derived for evaluating stability lobes. The chatter model developed by Budak and Altintas [49][50][51] is extended to include the effect of feed rate.

5.4.1 Dynamic Milling Model

5.4.1.1 Milling Mechanics

Consider the cutting model illustrated in Figure (5-7) with the following cutting conditions:

- spindle speed n [RPM]
- start and exit immersion angles, ϕ_{st} and ϕ_{ex} [rad]

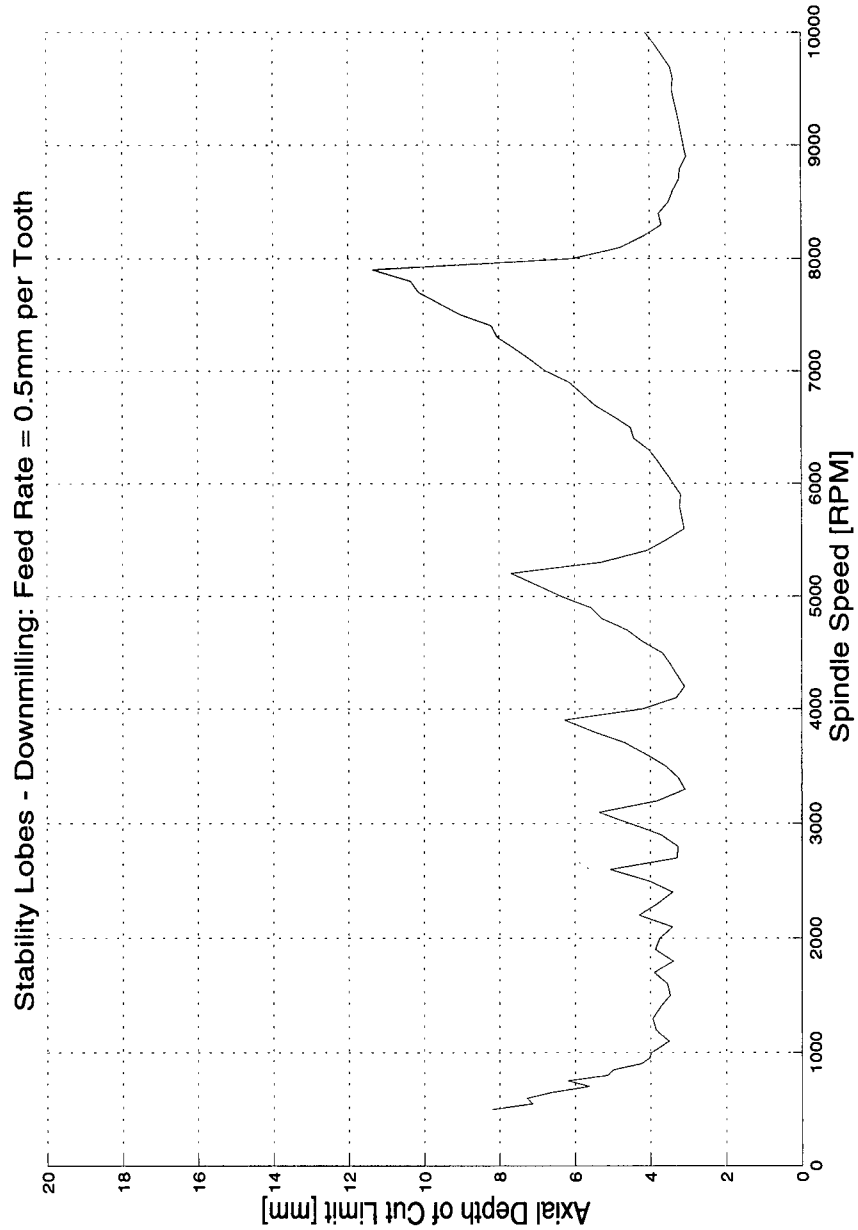

FIGURE 5-6: Predicted stability lobes from time domain simulations showing increasing stability at lower spindle speeds

- feed rate s_t [mm/tooth]
- N number of teeth - zero helix angle is assumed
- transfer functions $[G(\omega i)]$ describing the relative motion of the cutting tool and the workpiece
- cutting force coefficients in the radial and tangential directions, K_t and K_r

FIGURE 5-7: Dynamic milling model

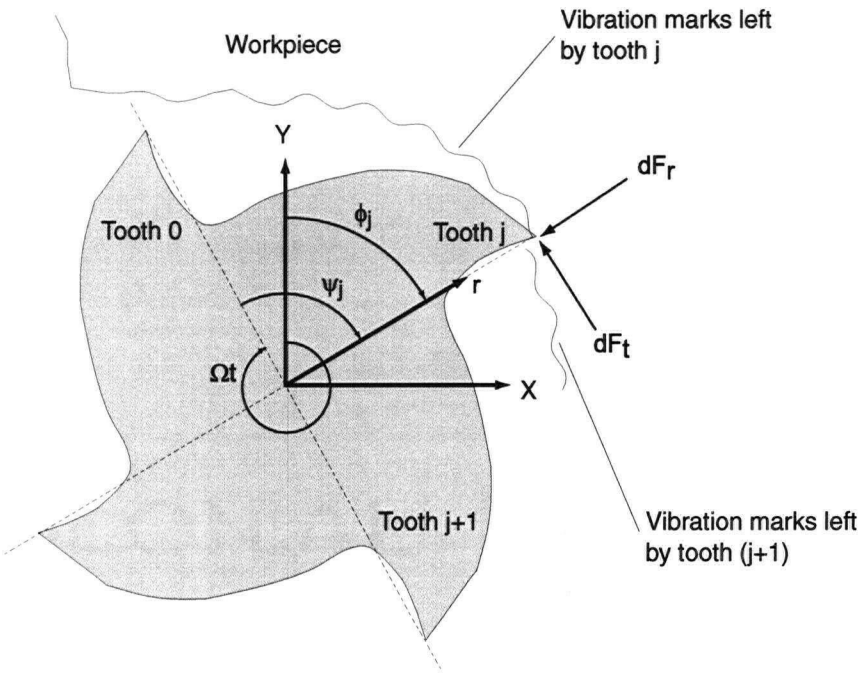

Cutting forces excite the structure in the X (feed) direction and in the Y (normal) direction causing dynamic displacements x and y. Since chip thickness is measured in the radial direction, the displacement can be expressed as:

$$r_j = -x\sin\phi_j - y\cos\phi_j \tag{5-2}$$

where ϕ_j is the instantaneous angular position of the tooth j, measured clockwise from the positive Y axis as:

$$\phi_j(t) = \Omega t + \psi_j \tag{5-3}$$

where Ω is the rotational velocity of the spindle in radians: $\Omega = \frac{2\pi n}{60}$. The tooth location angle, ψ_j, is taken as the angular position of tooth j with respect to the cutter. The angles ψ_j may represent non-uniform pitch or uniform pitch, in which case $\psi_j = \frac{j2\pi}{N}$.

The resulting chip thickness consists of a static term, approximated as $s_t \sin\phi_j$, and a dynamic component, which is evaluated as the difference between the present radial displacement, r_j, and the radial displacement of the surface which would have been left by the previous tooth, $r_{j,0}$. A constant feed per tooth, s_t, is assumed here, which would vary from tooth to tooth when modelling a non-uniform pitch cutter. The total chip thickness can be expressed as:

$$h(\phi_j) = [s_t \sin\phi_j + (r_j - r_{j,0})]g(\phi_j) \tag{5-4}$$

where $g(\phi_j)$ is a unit step function which incorporates the immersion angle limits ϕ_{st} and ϕ_{ex}, giving a zero chip thickness when the tooth is not submersed in the workpiece:

$$\begin{aligned} g(\phi_j) &= 1 \leftarrow \phi_{st} \le \phi_j \le \phi_{ex} \\ g(\phi_j) &= 0 \leftarrow \phi_j < \phi_{st} \text{ or } \phi_j > \phi_{ex} \end{aligned} \tag{5-5}$$

Since the static component of the chip thickness does not contribute to the wave regeneration mechanism, it may be left out for the purpose of determining the limit of stability. The dynamic chip thickness component is transformed to the X-Y coordinate system as:

$$h(\phi_j) = [\Delta x \sin\phi_j + \Delta y \cos\phi_j]g(\phi_j) \tag{5-6}$$

where $\Delta x = x - x_0$ and $\Delta y = y - y_0$. (x_0, y_0) represents the displacement at the previous tooth pass.

The tangential and radial cutting force components for tooth j, $F_{t,j}$ and $F_{r,j}$, are evaluated as:

$$F_{t,j} = K_t a h(\phi_j)$$

$$F_{r,j} = K_r h F_{t,j} \tag{5-7}$$

where a is the axial depth of cut. Note that a more simplified force model is used here than in the time domain simulation. K_t is the cutting pressure, and K_r is a ratio between tangential and radial cutting pressures. The forces are transformed to X and Y directions as:

$$F_{x,j} = -F_{t,j}\cos\phi_j - F_{r,j}\sin\phi_j$$

$$F_{y,j} = F_{t,j}\sin\phi_j - F_{r,j}\cos\phi_j \tag{5-8}$$

The forces contributed by each tooth are summed to get the total force acting on the cutter.

$$F_x = \sum_{j=1}^{N} F_{x,j}$$

$$F_y = \sum_{j=1}^{N} F_{y,j} \tag{5-9}$$

Combining equations (5-6) to (5-9) and rearranging into matrix form gives:

$$\begin{Bmatrix} F_x \\ F_y \end{Bmatrix} = \frac{1}{2} a K_t \begin{bmatrix} a_{xx} & a_{xy} \\ a_{yx} & a_{yy} \end{bmatrix} \begin{Bmatrix} \Delta x \\ \Delta y \end{Bmatrix} \tag{5-10}$$

where the time dependent dynamic milling force coefficients are given as:

$$a_{xx} = \sum_{j=1}^{N} -g_j[\sin 2\phi_j + K_r(1 - \cos 2\phi_j)]$$

$$a_{xy} = \sum_{j=1}^{N} -g_j[(1 + \cos 2\phi_j) + K_r \sin 2\phi_j]$$

$$a_{yx} = \sum_{j=1}^{N} g_i[(1 - \cos 2\phi_j) - K_r \sin 2\phi_j]$$

$$a_{xx} = \sum_{j=1}^{N} g_j[\sin 2\phi_j + K_r(1 + \cos 2\phi_j)] \tag{5-11}$$

In simplified form, equation (5-10) can be expressed as:

$$\{F(t)\} = \frac{1}{2} a K_t [A(t)]\{\Delta(t)\} \tag{5-12}$$

5.4.1.2 Dynamic Chip Regeneration

Assume a chatter frequency ω_c. The current displacement and the displacement at the previous tooth pass (x, y) and (x_0, y_0) can be expressed as sinusoidal functions.

Traditionally, (x_0, y_0) is taken as the displacement at time $t - T$, where T is the tooth period. For non-uniform pitch cutters, the period will vary from tooth to tooth. The number of vibration marks left on the surface during one tooth period is $k + \frac{\varepsilon}{2\pi}$,

$$k + \frac{\varepsilon}{2\pi} = \frac{\omega_c T}{2\pi} \tag{5-13}$$

where k is the number of complete vibration marks and ε is the remaining fraction of a wave, as shown in Figure (5-8). ε also represents the phase shift between a tooth's vibration and the wavy surface left by the previous tooth. Each *lobe* of the stability border corre-

sponds to each integer value of k, with the bottom of the lobe typically representing a phase shift, ε, of about $180°$ when the regeneration has most influence.

FIGURE 5-8: Number of vibration marks in a single tooth period

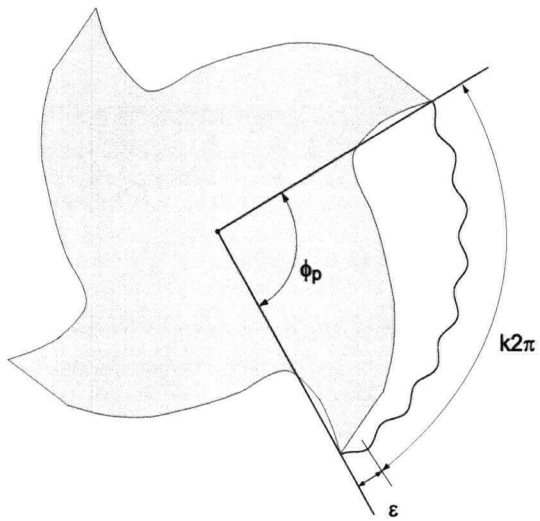

For small feed rates, using a delay of T between the tooth path of successive teeth is a valid approximation. However, when the feed per tooth is significant compared to the length of the wave mark left on the cutting surface, an additional delay term is required to account for feed.

Consider Figure (5-9), which shows an exaggerated feed rate. The actual instantaneous chip thickness is the distance between point **c**, the current location of Tooth j, and point **b**, the point on the surface at Tooth j's current position. The approximation above which assumes this corresponds to a time delay of T, actually gives point **a** on the surface, a distance s_t in the negative X direction from the current tooth position. A more exact representation of chip thickness is given by taking an additional time delay, $-T_{s_t}\cos\phi_j$, where T_{s_t} corresponds to the time a tooth takes to travel the feed per tooth distance, s_t:

FIGURE 5-9: Chip thickness evaluation considering additional time delay caused by feed rate

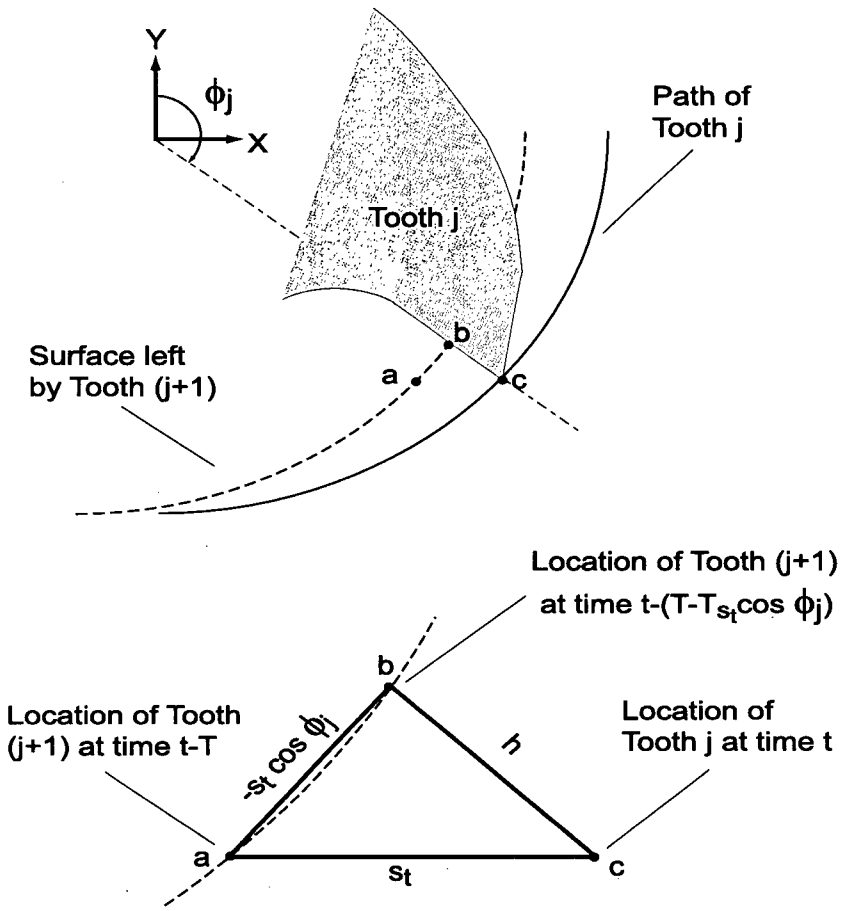

$$T_{s_t} = \frac{s_t}{\Omega R} \tag{5-14}$$

When considering vibration marks left on the surface, this additional time delay corresponds to $T_{s_t}\omega_c/2\pi$ wave cycles. At any tooth position, ϕ_j, the additional phase shift between current tooth path and surface left by the previous tooth in cycles is given as $-T_{s_t}\cos\phi_j\omega_c$. Considering the start and exit immersion angles, the number of cycles the phase shift changes while the tooth is cutting is:

$$k_{s_t} + \frac{\varepsilon_{s_t}}{2\pi} = \frac{-T_{s_t}\omega_c[\cos\phi_{st} - \cos\phi_{ex}]}{2\pi} \tag{5-15}$$

where k_{s_t} is the integer number of wave marks and ε_{s_t} is the remaining fraction of a vibration wavelength.

When the effect of feed rate is added to equation (5-13), the total number of vibration waves separating the path of the current tooth with the vibration marks left by the previous tooth may be expressed as:

$$k + \frac{\varepsilon}{2\pi} = \frac{(T - T_{s_t}\cos\phi_j)\omega_c}{2\pi} \tag{5-16}$$

The additional delay, $T_{s_t}\cos\phi_j$, causes phase shift, ε , to decrease by $T_{s_t}\omega_c$ from $\phi = 0$ to $\phi = \pi/2$ and to increase by $T_{s_t}\omega_c$ from $\phi = \pi/2$ to $\phi = \pi$. As $T_{s_t}\omega_c$ increases, the time varying phase shift can increase stability.

Figure (5-10),shows a example of wave paths of two consecutive teeth from vibrations in the Y direction, with a significant feed rate relative to the radius of the cutter and to the wave length of vibrations. As the cutter rotates, the phase shift changes as a function of the angular position of the tooth. The additional phase shift due to the feed rate causes the phase shift to change from point A through to point E, where $\phi = \pi$ and the current tooth lags the previous tooth path by T_{s_t}, or by the length s_t on the cutting surface.

Regeneration of vibrations in the X direction will be less impacted by feed since the greatest effect of feed is at $\phi = 0$ and at $\phi = \pi$, where chip thickness is taken in the normal (Y) direction. The directional coefficients will take this into consideration.

The dynamics of the system are described by the transfer function matrix, $[G(i\omega)]$:

$$[G(i\omega)] = \begin{bmatrix} G_{xx}(i\omega) & G_{xy}(i\omega) \\ G_{yx}(i\omega) & G_{yy}(i\omega) \end{bmatrix} \tag{5-17}$$

FIGURE 5-10: Wave regeneration with a large feed rate relative to vibration wave length and to the cutter radius; phase shift changes at different angular positions of the cutter

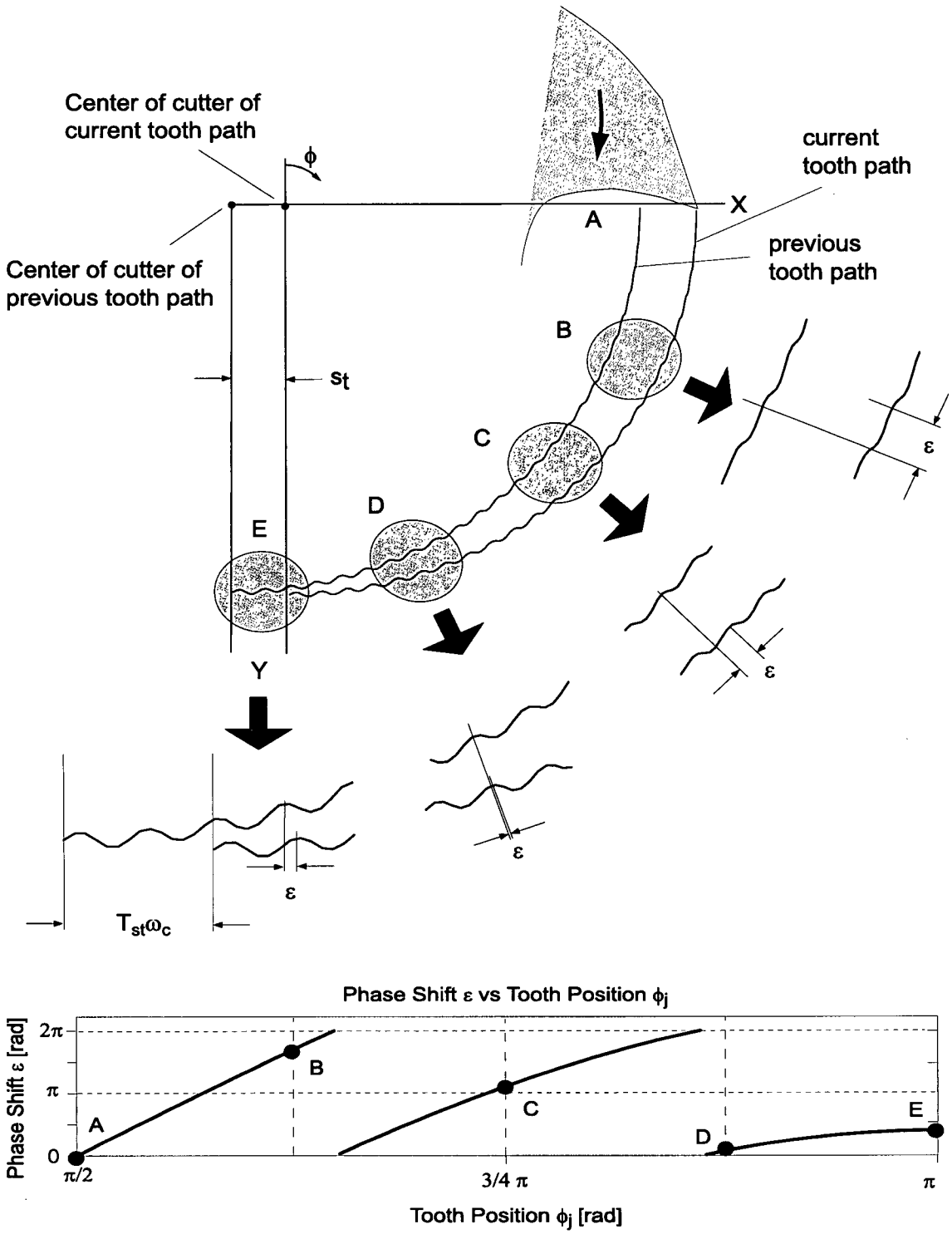

If two orthogonal degrees of freedom are considered in the X and Y directions, the cross transfer functions $G_{xy}(i\omega)$ and $G_{yx}(i\omega)$ are omitted. With an assumed constant chatter frequency, ω_c, the vibrations may be expressed in the frequency domain as:

$$\begin{Bmatrix} x(i\omega) \\ y(i\omega) \end{Bmatrix} = \begin{Bmatrix} G_{xx}(i\omega)F_x \\ G_{yy}(i\omega)F_y \end{Bmatrix} e^{i\omega_c t}$$

$$\begin{Bmatrix} x_0(i\omega) \\ y_0(i\omega) \end{Bmatrix} = e^{-i\omega_c(T - T_{s_t}\cos\phi_j)} \begin{Bmatrix} x(i\omega) \\ y(i\omega) \end{Bmatrix} \tag{5-18}$$

where $\omega_c(T - T_{s_t}\cos\phi_j)$ is the phase delay between the vibrations at successive tooth passes in both the X and Y directions. A more condensed form is expressed as dynamic chip thickness vector $\{\Delta(i\omega_c)\}$:

$$\{\Delta(i\omega_c)\} = b[G(i\omega_c)]\{F\}e^{i\omega_c t} \tag{5-19}$$

where the time dependent *regeneration coefficient*, $b(t, i\omega_c)$, is given as:

$$b(t, i\omega_c) = 1 - e^{-i\omega_c(T - T_{s_t}\cos\phi_j)} \tag{5-20}$$

$\{\Delta(i\omega_c)\}$ from (5-19) is substituted into the dynamic milling force equation (5-12) and written in the frequency domain as:

$$\{F\}e^{i\omega_c t} = \frac{1}{2}aK_t[A(t)][b(t, i\omega_c)][G(i\omega_c)]\{F\}e^{-i\omega_c t} \tag{5-21}$$

Since $[A(t)]$ and $b(t, i\omega_c)$ are time dependent, they may be approximated by the average of their combined values over one tooth period. This time constant *oriented regeneration* matrix is evaluated as:

$$[C(i\omega_c)] = \begin{bmatrix} c_{xx} & c_{xy} \\ c_{yx} & c_{yy} \end{bmatrix} = \frac{1}{T}\int_0^T [A(t)]b(t, i\omega_c)dt \tag{5-22}$$

5.4.1.3 Evaluating Chatter Frequency and Stability Limit

The simplified dynamic milling equation is now given as:

$$\{F\}e^{i\omega_c t} = \frac{1}{2}aK_t[C(i\omega_c)][G(i\omega_c)]\{F\}e^{-i\omega_c t} \tag{5-23}$$

which has a non-trivial solution if its determinant is zero:

$$det\left[[I] - \frac{1}{2}aK_t[C(i\omega_c)][G(i\omega_c)]\right] = 0 \tag{5-24}$$

The eigenvalue of the characteristic equation above is defined as:

$$\Lambda = -\frac{1}{2}aK_t \tag{5-25}$$

The resulting characteristic equation becomes:

$$det[[I] + \Lambda[C(i\omega)][G(i\omega)]] \tag{5-26}$$

With $[G(i\omega)]$ being a diagonal matrix from the assumption of two orthogonal degrees-of-freedom, the solution to the eigenvalue problem becomes a simple quadratic equation:

$$a_0\Lambda^2 + a_1\Lambda + 1 = 0 \tag{5-27}$$

where,

$$a_0 = G_{xx}G_{yy}(c_{xx}c_{yy} - c_{xy}c_{yx})$$

$$a_1 = c_{xx}G_{xx} + c_{yy}G_{yy} \tag{5-28}$$

The complex eigenvalue is obtained as:

$$\Lambda = -\frac{1}{2a_0}(a_1 \pm \sqrt{a_1^2 - 4a_0}) \tag{5-29}$$

The axial depth of cut limit a_{lim} is found from equation (5-25) as:

$$a_{lim} = -\frac{2\Lambda}{K_t} \tag{5-30}$$

For an arbitrary spindle speed and an assumed chatter frequency, ω_c, a_{lim} is a complex value. Since the depth of cut must be a real positive value, the chatter frequency must fall where the imaginary component of a_{lim} is zero. For a given spindle speed, a range of chatter frequencies around the natural frequencies of the system are scanned for all real and positive values of a_{lim}. The system is most susceptible to chatter at the frequency where the axial depth of cut limit is smallest. The axial depth of cut limit for the given conditions is the minimum value of a_{lim}, which satisfies the condition $\Im[a_{lim}] = 0$. The corresponding frequency is that at which the system will chatter.

5.4.1.4 Stability Lobes

The steps in calculating the stability lobes are summarized below:

1. Machine dynamics, cutting tool geometry, feed rate, cutter orientation and immersion, and force coefficients are specified.
2. A range of spindle speeds and a spindle speed step size is specified.
3. A range of chatter frequencies around the natural frequencies of the system and a chatter frequency step size are specified.
4. For a given spindle speed and each chatter frequency, the oriented regeneration matrix $[C]$ is found by numerically evaluating the integral of equation (5-22).
5. For each chatter frequency, the eigenvalue Λ is solved using equation (5-29) and the complex axial depth of cut limit is found from equation (5-30).
6. By scanning through the values of a_{lim} for the range of chatter frequencies, the chatter frequencies and real a_{lim} values are interpolated for at each point where $\Im[a_{lim}]$ crosses

zero. The smallest positive depth of cut limit is selected from these real a_{lim} values, and the corresponding frequency is the chatter frequency, ω_c.

7. Steps 4 through 6 are repeated for each spindle speed.

5.4.2 Simplified Case of Milling a Flexible SDOF Workpiece

Consider the dynamic milling model in Figure (5-11). In this simplified system, the cutter is considered rigid relative to the flexible workpiece, which is allowed to deflect only in the Y (normal) direction. This is commonly encountered in the machining of very flexible plates.

FIGURE 5-11: Milling a Flexible SDOF Workpiece

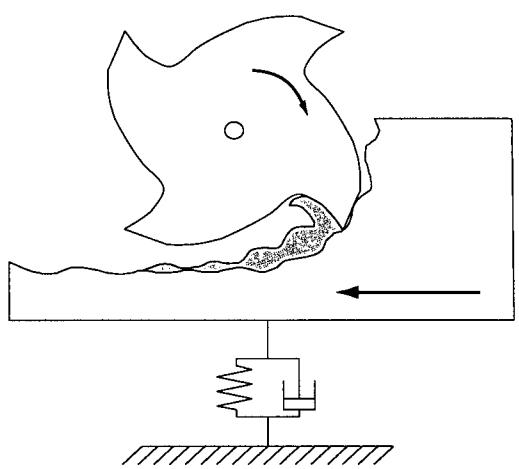

For a SDOF system, equation (5-24) reduces to:

$$1 - \frac{1}{2} a K_t c_{yy}(i\omega_c) G_{yy}(i\omega_c) = 0 \tag{5-31}$$

which has a single solution for a_{lim} in the form:

$$a_{lim} = \frac{2}{K_t c_{yy}(i\omega) G_{yy}(i\omega)} \tag{5-32}$$

Note that when modelling the dynamics in the form of a transfer function, G_{yy}, the motion in the degree of freedom Y may contain multiple modes.

The same seven steps above are followed to evaluate the stability lobes except equation (5-32) is used in step (5) to evaluate a_{lim}.

5.4.3 Example 1: Milling a SDOF workpiece

The cutting conditions are defined as follows:

- Workpiece dynamics: $\omega_{n_y} = 3800$ Hz, $\zeta_y = 0.04$, $k_y = 1e7$ m/N
- The machine and cutter are assumed to be rigid
- Force coefficients: $K_t = 796$ MPa, $K_r = 0.21$
- Cutter geometry: 0° helix, uniform 4 flute, $R = 10.0$ mm

The transfer function $G_{yy}(i\omega)$ is evaluated as:

$$G(i\omega) = \frac{\omega_{n_y}^2 / k_y}{-\omega^2 + 2\zeta_y \omega_{n_y}(i\omega) + \omega_{n_y}^2}$$

The imaginary and real components and the magnitude/phase shift plots for $G_{yy}(i\omega)$ are shown in Figure (5-12).

A range of spindle speeds is selected from 500 to 5000 RPM. For each spindle speed, c_{yy} is evaluated over a range of chatter frequencies and a_{lim} is found from equation (5-32).

For half immersion downmilling and a spindle speed of $n = 1000$ RPM, a_{lim} versus ω_c is shown in Figure (5-13) with all valid a_{lim} values located where its imaginary component crosses zero. For these cutting conditions at $n = 1000$ RPM, the limiting depth of cut is $a_{lim} = 2.95$ mm and the corresponding chatter frequency is $\omega_c = 3966$ Hz.

FIGURE 5-12: Relative tool-workpiece transfer function in Y direction

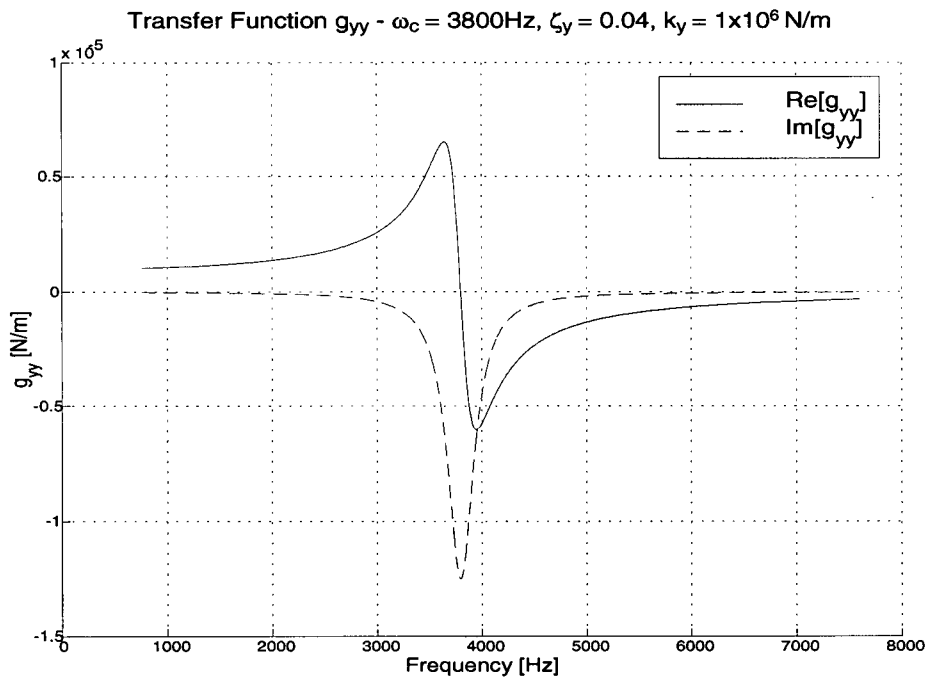

The resulting stability for the entire range of spindle speeds is shown in Figure (5-14). Figure (5-15) shows the stability lobes for an increased feed rate of s_t = 0.5 mm/tooth. In addition to the lobes created for each integer value of k, a second larger set of lobes are now present as k_{s_t} changes through multiple integer values. These *feed lobes* can become more pronounced depending on the directional coefficient matrix $[A]$. In Figures (5-16) through (5-18) stability lobes are plotted for half immersion upmilling and downmilling, and slotting for various feed rates. For slotting, note that the stability border actually decreases slightly for a range of spindle speeds. The borderline then eventually shifts upwards at lower spindle speeds. This pattern will be explained in a later section.

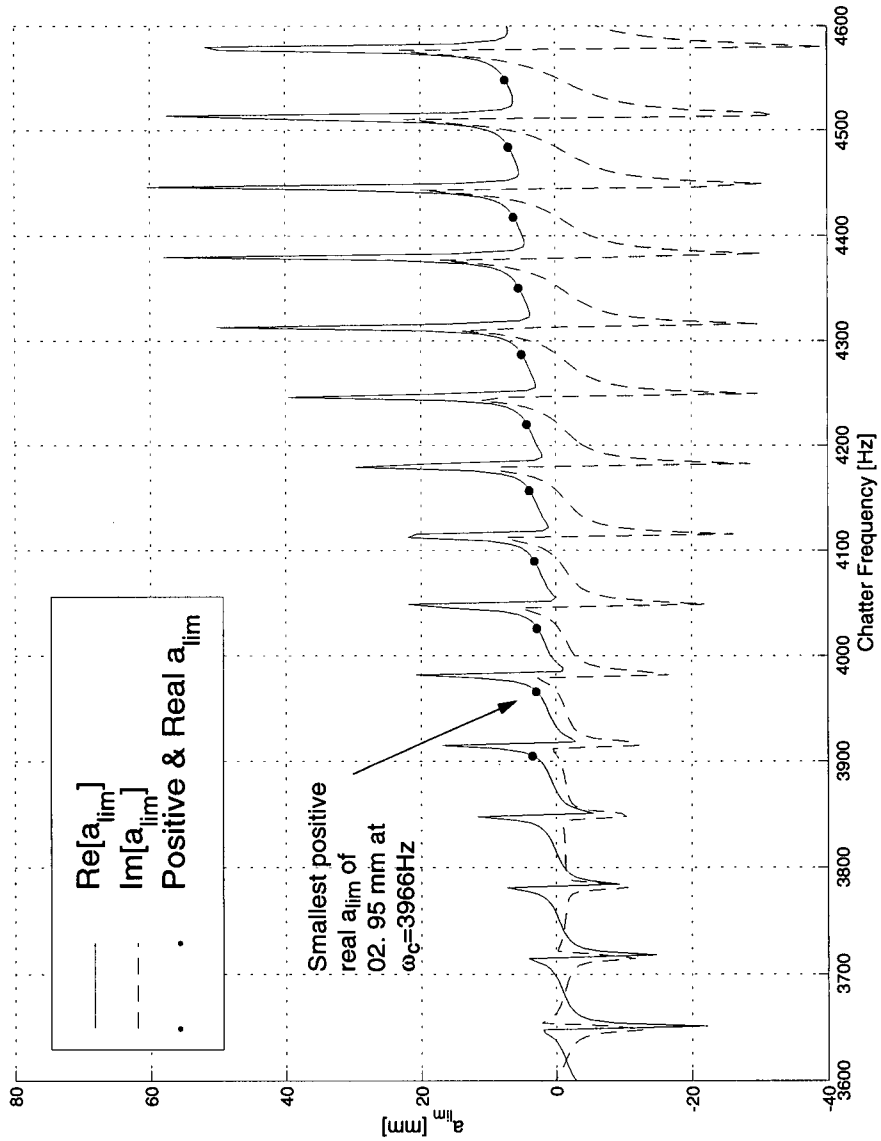

FIGURE 5-13: Real and positive a_{lim} values for n = 1000 RMP

FIGURE 5-14: Stability lobes - downmilling, half immersion, feed = 0.1 mm/tooth

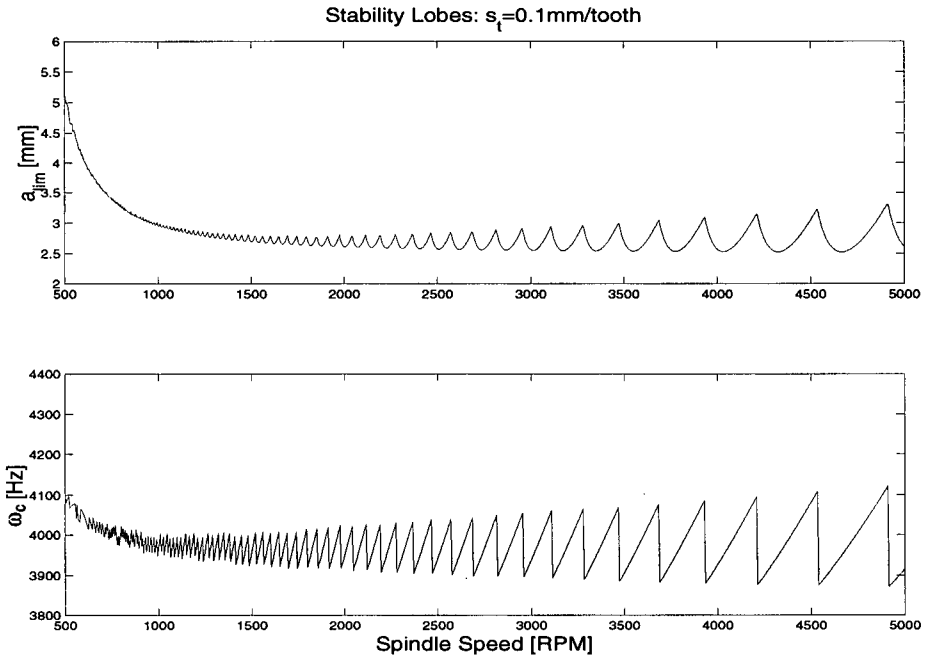

FIGURE 5-15: Stability lobes - downmilling, half immersion, feed = 0.5 mm/tooth

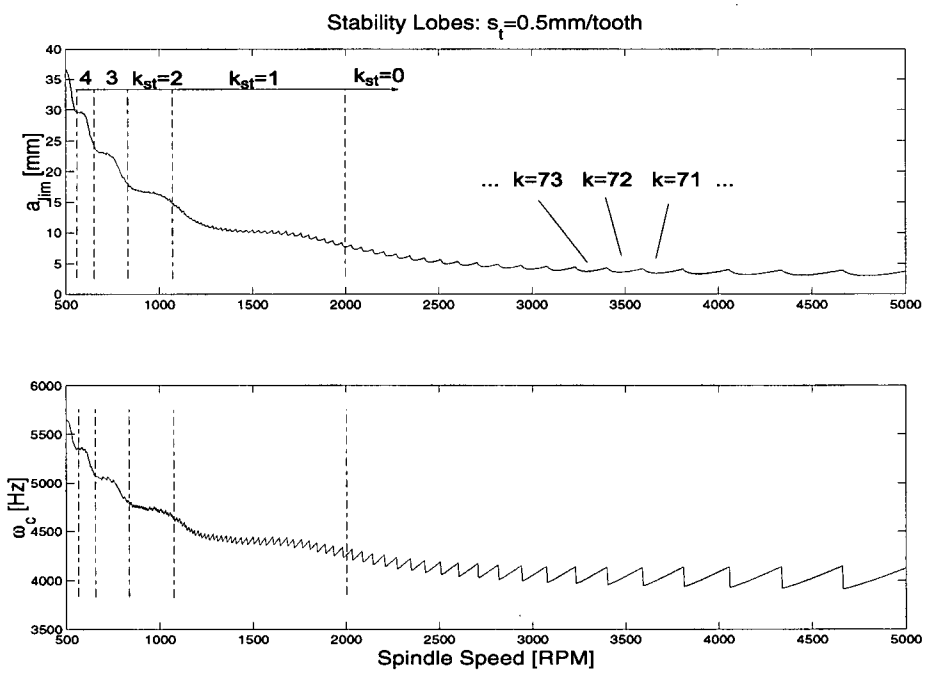

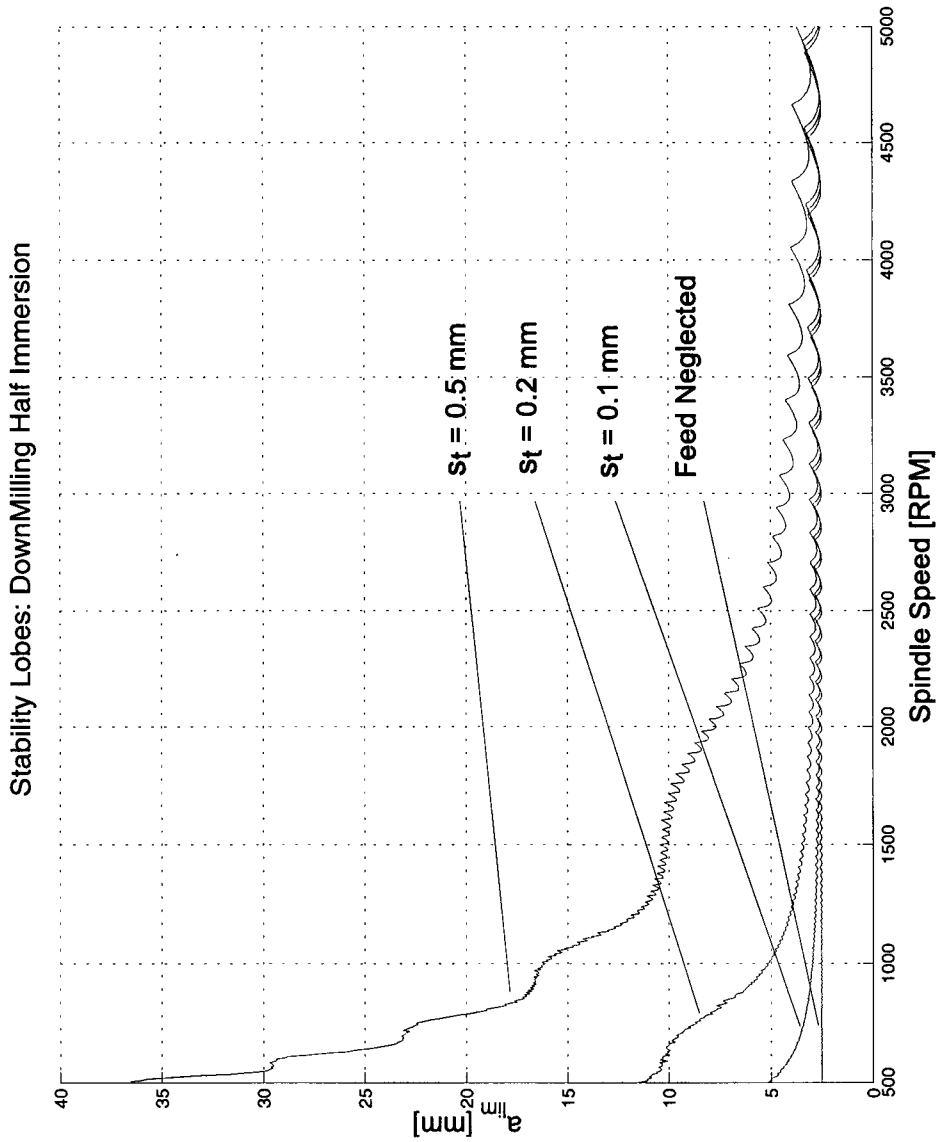

FIGURE 5-16: Stability Lobes: Downmilling half immersion - feed of 0 to 0.5 mm/tooth

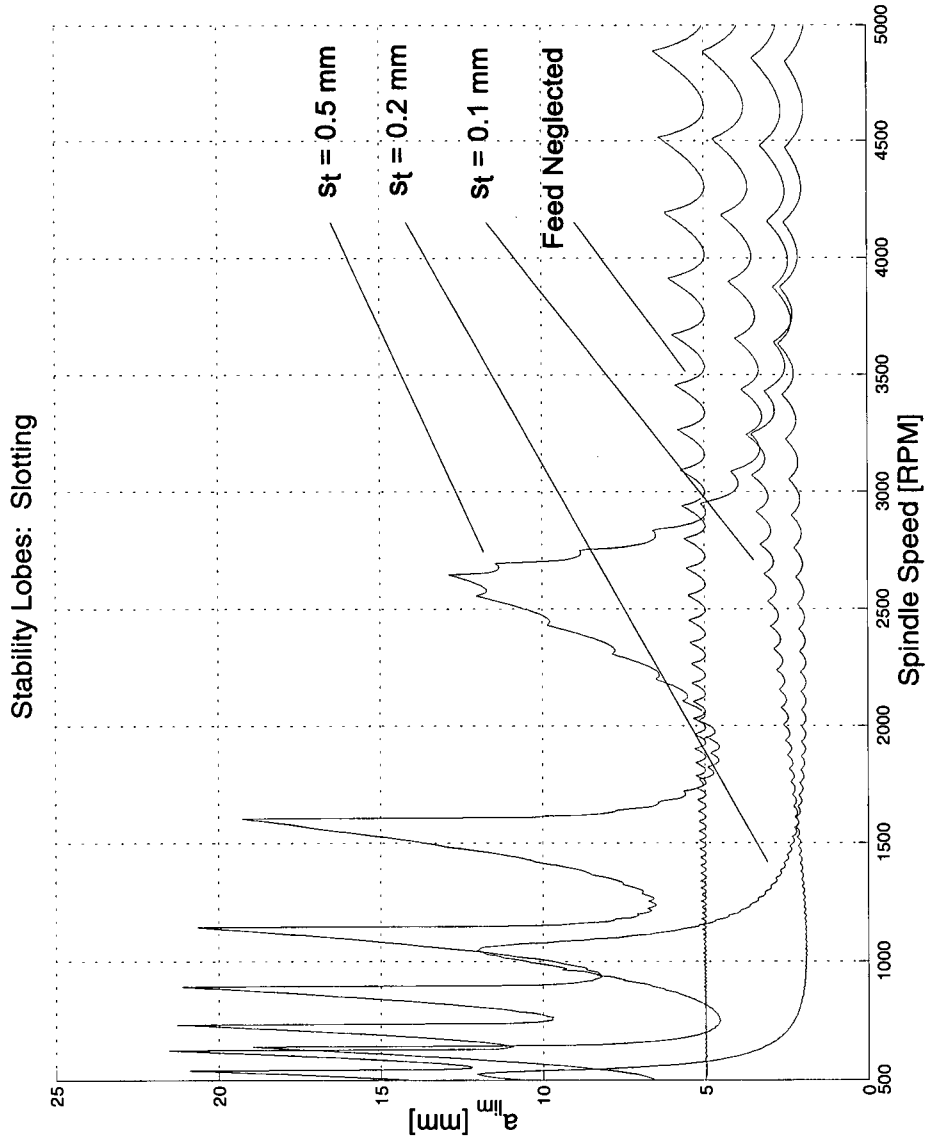

FIGURE 5-17: Stability Lobes: slotting - feed of 0 to 0.5 mm/tooth

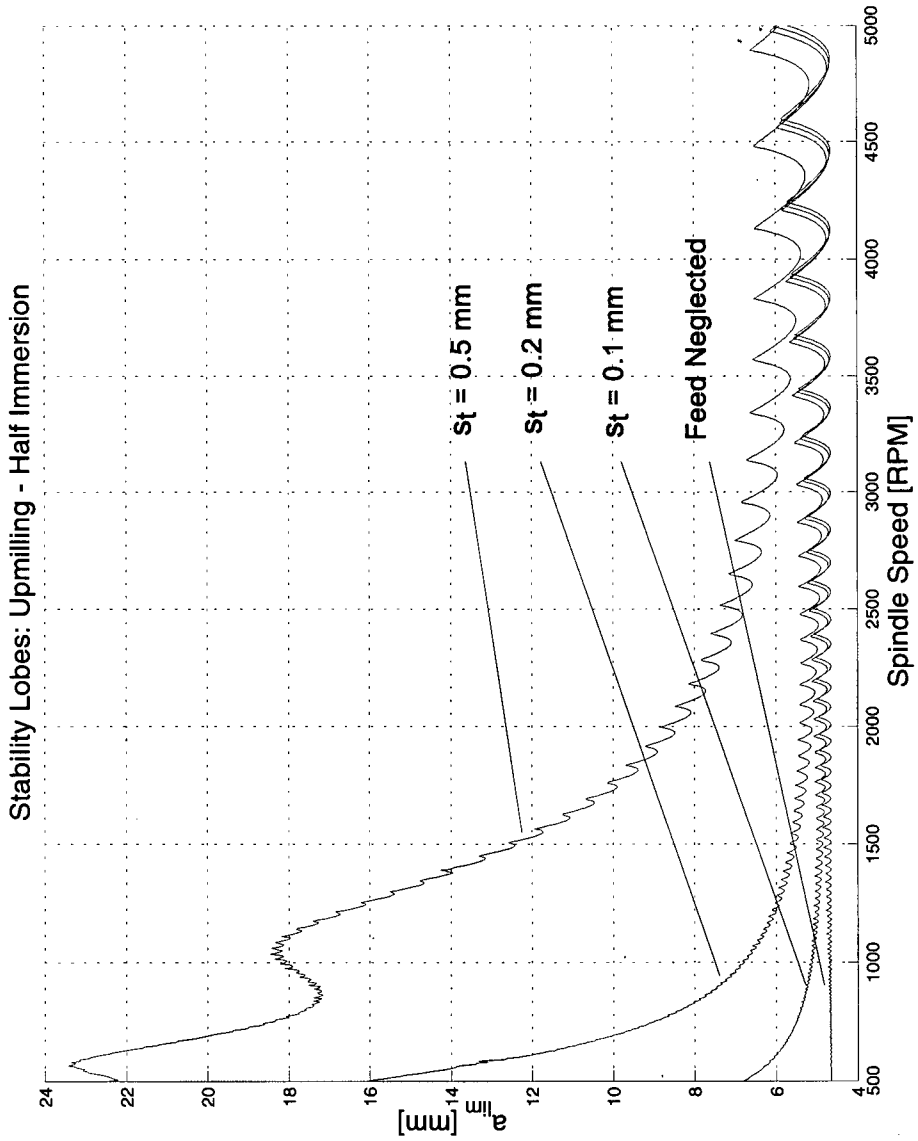

FIGURE 5-18: Stability Lobes: upmilling, half immersion - feed of 0 to 0.5 mm/tooth

5.4.4 Example 2: Milling with Two DOF Dynamics

This example uses dynamics both in the X and in the Y directions. The same dynamic parameters are used in both directions, as would be the case then milling with a flexible cutter and rigid workpiece. The cutting conditions for the simulation are as follows:

- Cutter dynamics in X direction: ω_{n_x} = 3800 Hz, ζ_x = 0.04, k_x = 1e7 m/N
- Cutter dynamics in Y direction: ω_{n_y} = 3800 Hz, ζ_y = 0.04, k_y = 1e7 m/N
- The workpiece is assumed to be rigid
- Force coefficients: K_t = 796 MPa, K_r = 0.21
- Cutter geometry: 0° helix, uniform 4 flute, R = 10.0 mm
- Feed rate s_t = 0.0 to 0.5 mm/tooth

Figures (5-19) to (5-21) show the predicted stability lobes for downmilling and upmilling half immersion and slotting cases with and without the effect of feed rate. The trends are similar to the single degree of freedom case in Example 1, with one key difference. The larger lobes caused by the feed are deeper and do not show as much of an increase in stability at lower spindle speeds as in Example 1. This may be attributed to the fact that regeneration of vibrations in the X direction are not as affected by the feed rate as vibrations in the Y direction, as explained above. At lower spindle speeds the stability border becomes limited by the influence of modes in the X direction.

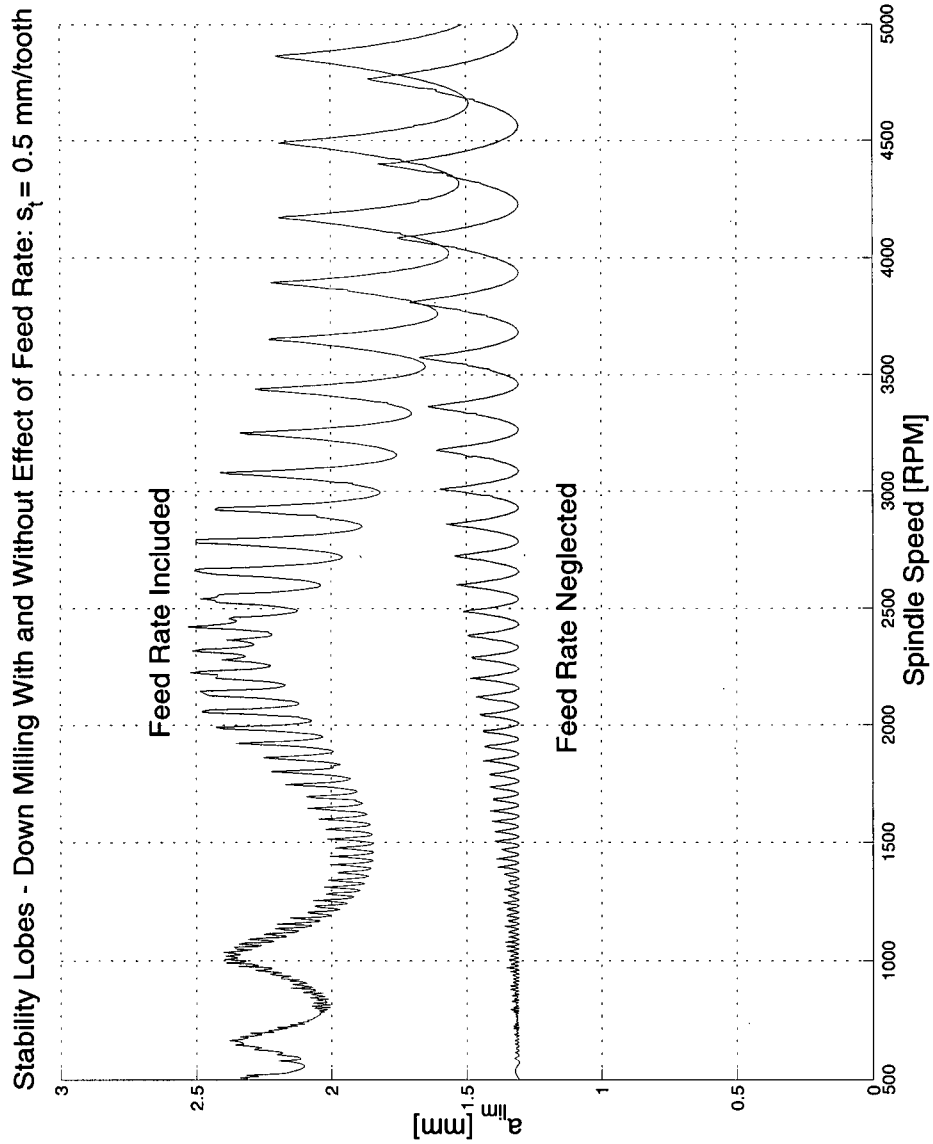

FIGURE 5-19: Stability Lobes: down milling, half immersion - with and without effect of feed of 0.5 mm/tooth

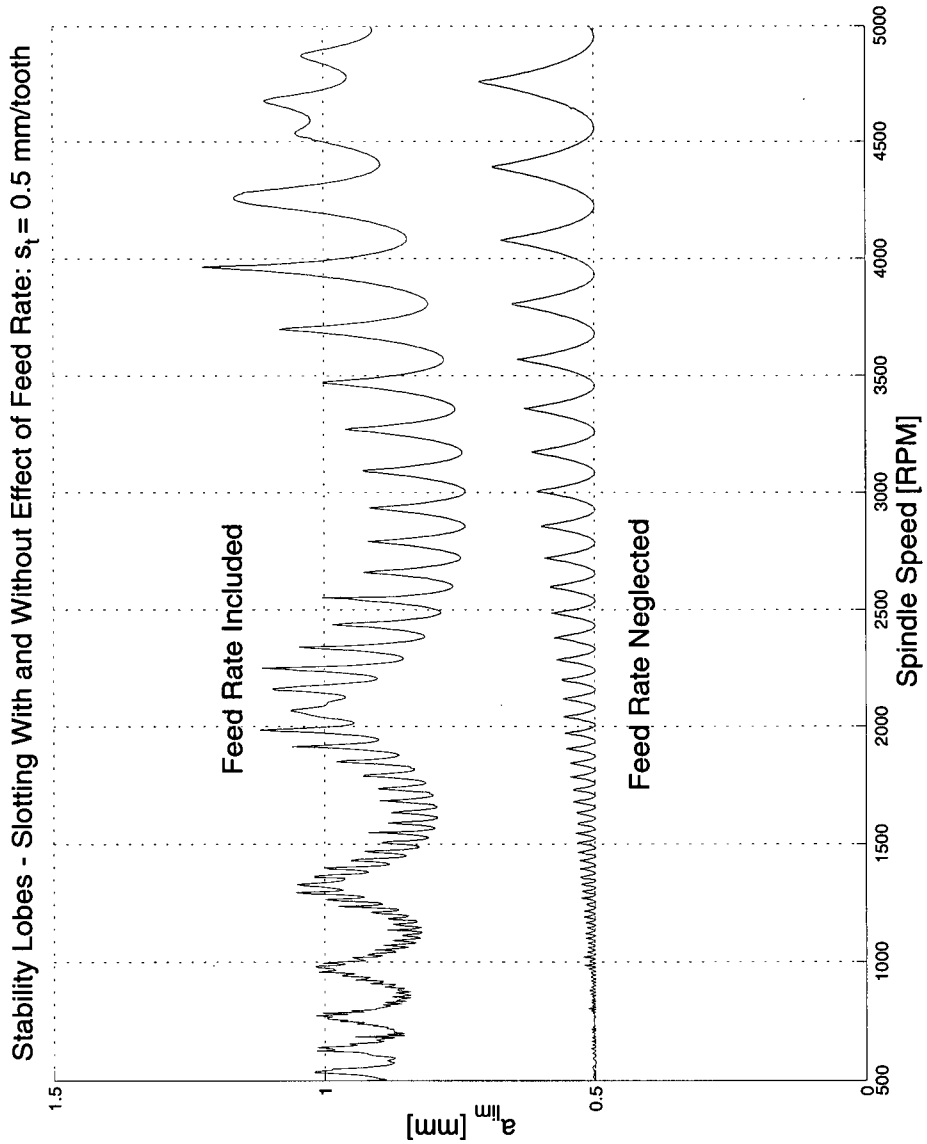

FIGURE 5-20: Stability Lobes: slotting - with and without effect of feed of 0 to 0.5 mm/tooth

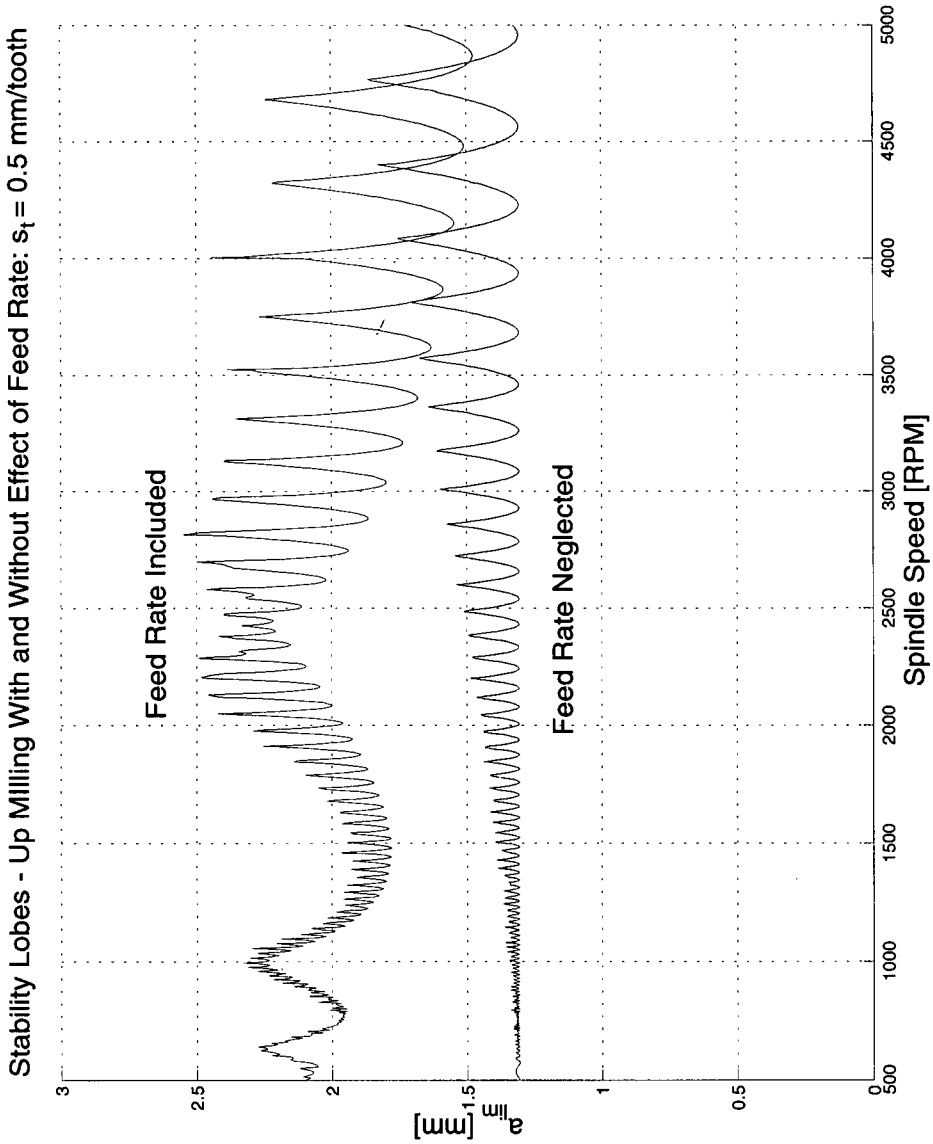

FIGURE 5-21: Stability Lobes: up milling, half immersion - with and without effect of feed of 0.5 mm/tooth

5.4.5 Example 3: Milling at Smaller Radial Widths of Cut

Here, Example 1 is repeated for one quarter and one eighth immersion upmilling and downmilling to observe the effects of feed rate at smaller radial widths of cut. Figures (5-22) to (5-25) show the stability lobes for feed rates up to 0.5 mm/tooth. Note that for smaller radial widths of cut, the maximum chip thickness becomes smaller, allowing larger feed rates. For example, for one eighth immersion, the width of cut for a 10.0 mm cutter is 0.76 mm. For a 0.5 mm/tooth feed rate, this corresponds to a maximum static uncut chip thickness of 0.19 mm.

The results show that radial immersion and orientation have a large impact on the way feed affects the stability border. As the immersion angle decreases, the feed lobes shift to lower spindle speeds. This is expected from equation (5-15), in which the number of wave cycles, k_{s_t}, decreases with smaller immersion angles. Also, for the one eighth immersion upmilling case, note that the feed lobes drop significantly rather than increase. Here the difference between upmilling and downmilling becomes more evident. This can be explained by two main factors. First, from equation (5-16), the feed rate causes the regeneration phase shift, ε, to decrease for upmilling and to increase for downmilling. Secondly, the directional coefficients vary considerably at different angular positions of the cutter, causing the matrix $[A]$ to differ between upmilling and downmilling.

The resulting directional regeneration matrix, $[C]$, can cause the overall stiffness of the system to increase or decrease. In most cases above, the shift is away from the natural frequency of the system, causing an increased stability. In certain conditions, the effect of feed rate on regeneration may cause the chatter frequency to shift towards the natural frequency for a range of spindle speeds, decreasing stability. This explains the downward shift in the feed lobes for the one eighth immersion upmilling case, and for the slotting case in Example 1.

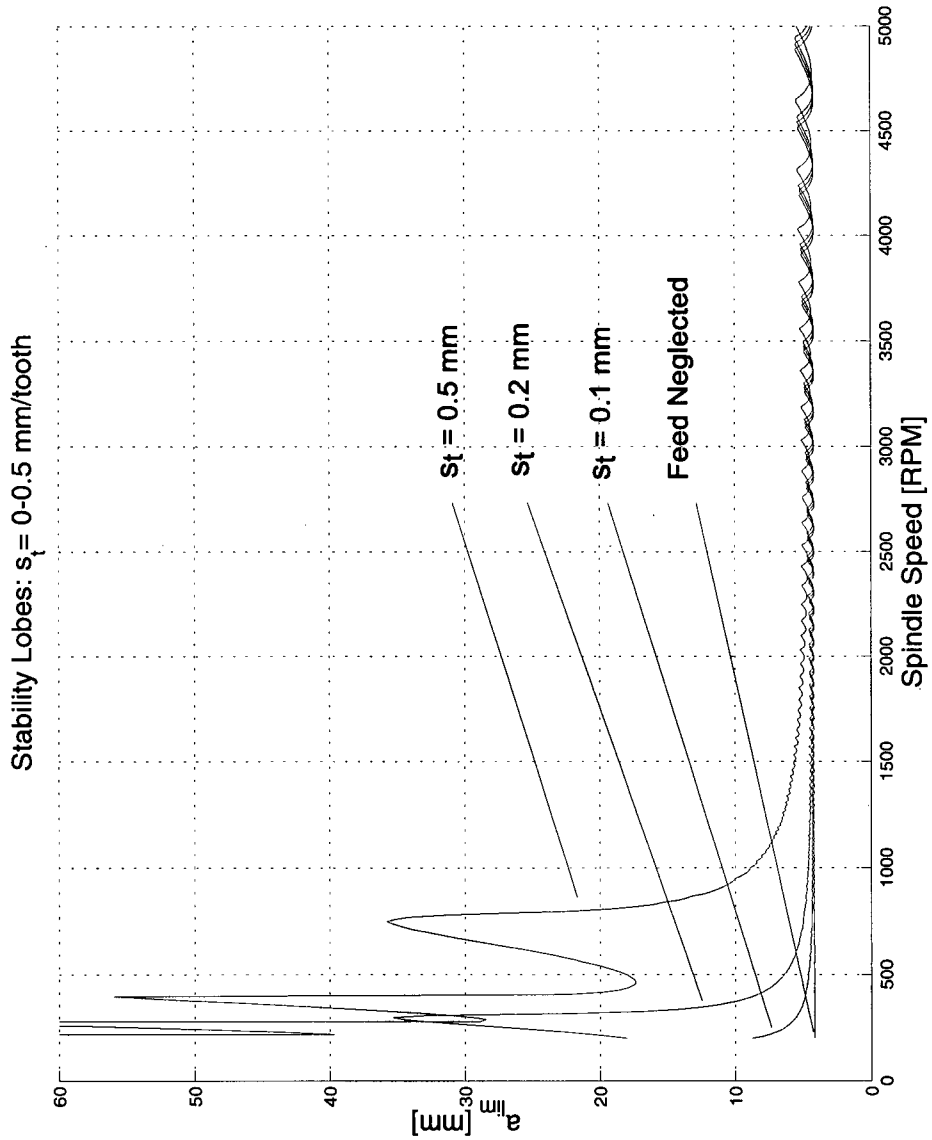

FIGURE 5-22: Stability Lobes: down milling, quarter immersion with feed rates up to 0.5 mm/tooth

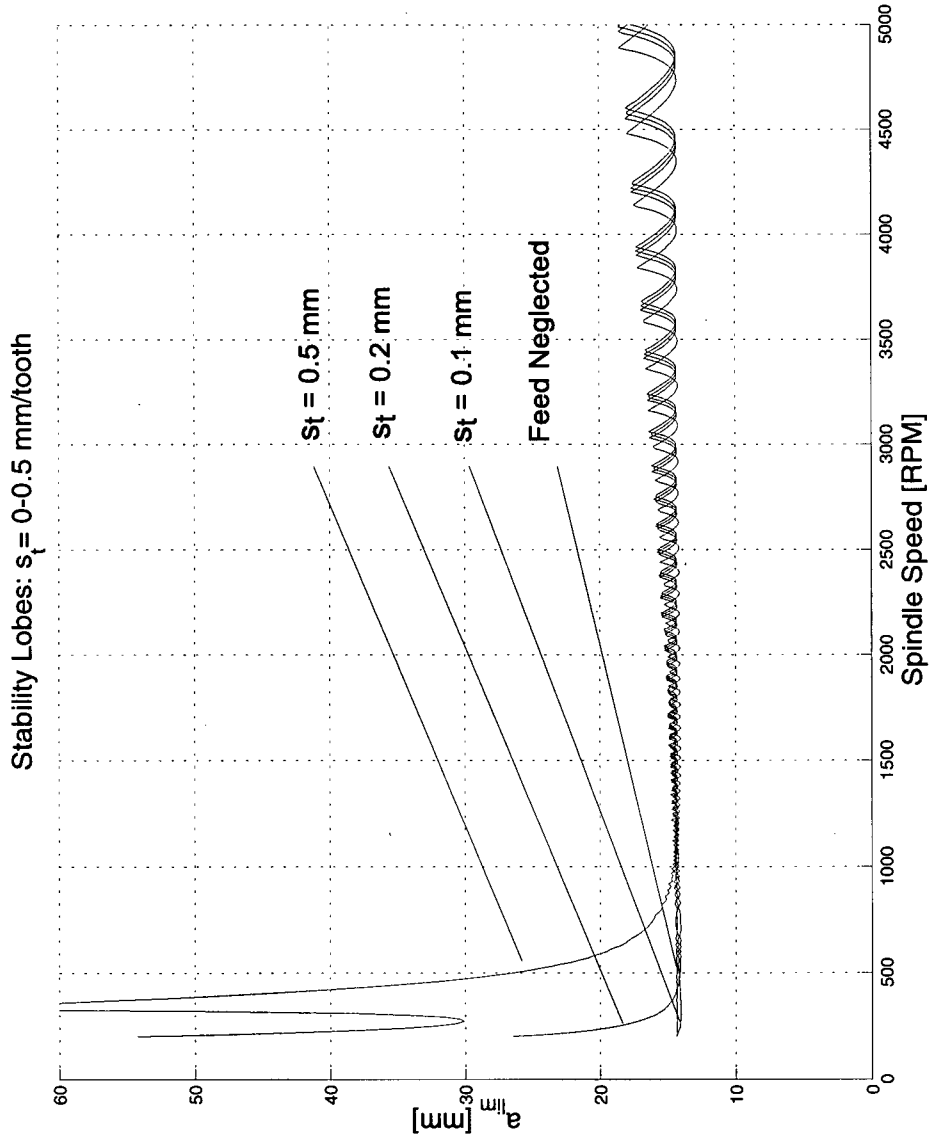

FIGURE 5-23: Stability Lobes: up milling, quarter immersion with feed rates up to 0.5 mm/tooth

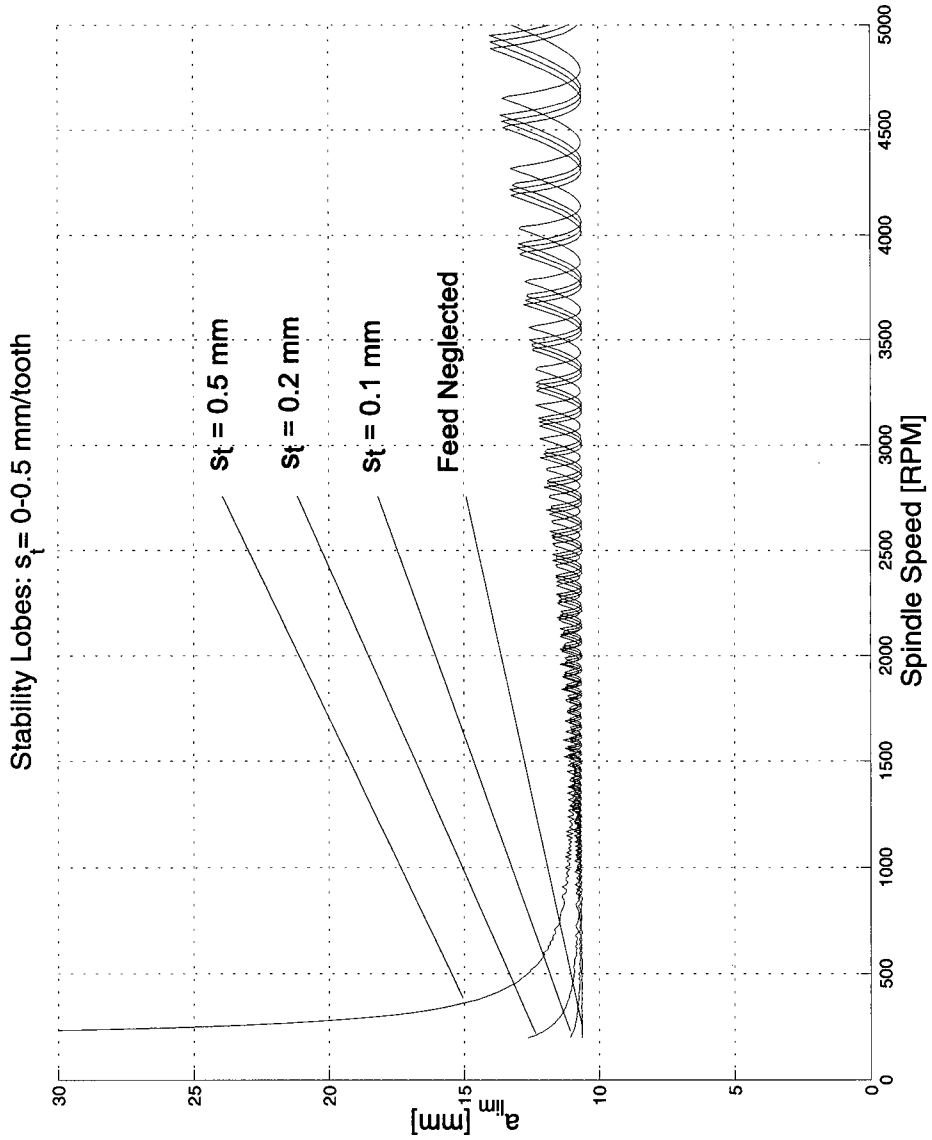

FIGURE 5-24: Stability Lobes: down milling, eighth immersion with feed rates up to 0.5 mm/tooth

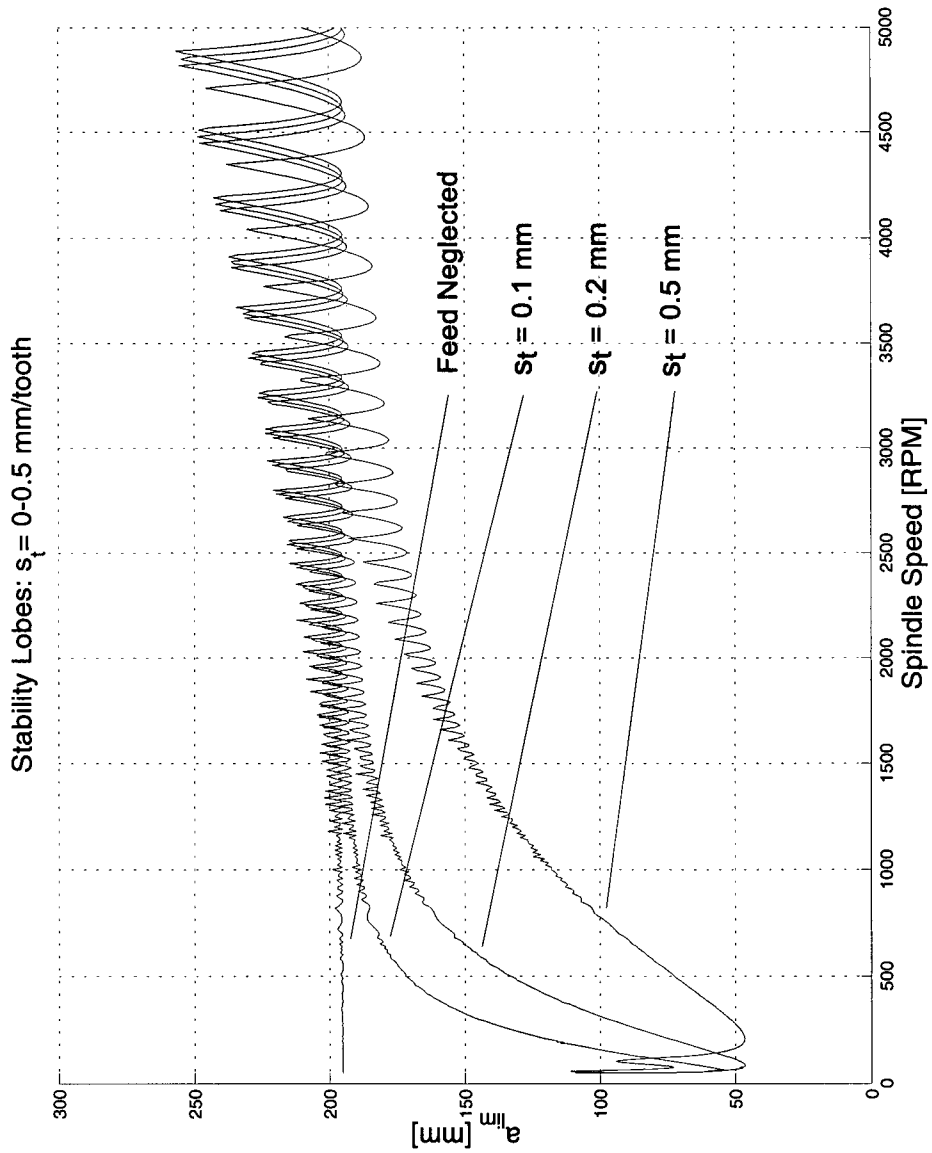

FIGURE 5-25: Stability Lobes: up milling, eighth immersion with feed rates up to 0.5 mm/tooth

5.5 Stability Lobes from Time Domain Versus from Frequency Domain

In this section, predicted stability lobes from time domain and from frequency domain models are compared for machining a flexible plate with a natural frequency of 1000 Hz. The cutter is assumed rigid.

The computation time of the time domain simulations is greatly affected by depth of cut, spindle speed, and frequency of vibrations. At lower spindle speeds and higher frequency vibrations, the density of points required to accurately maintain the cutting surface is much higher, requiring more computations. Larger depths of cut lead to more layers of points in the axial direction, also increasing computation time. In order to keep simulation times to a feasible range, the axial depth of cut is kept small with a workpiece stiffness of 1.0e6 N/m. The spindle speed is limited to no lower than 1000 RPM for the workpiece natural frequency of 1000 Hz. Under these conditions, a large feed rate of 1.0 mm per tooth had to be used to demonstrate the effect of feed on stability. Although such a large feed rate is typically impractical for a 3/4 inch cutter, the limited computational power of today's computers limit the cutting conditions which may be simulated.

Figures (5-26) and (5-27) show the predicted stability lobes with a very small feed rate and with a feed rate of 1.0 mm per tooth. The two models show the same increase in stability and lobing effect at lower spindle speeds. An offset does exist between the two predictions, which is most likely attributed to the difference in criteria used to determine the stability limit, as discussed in above. Further more, stability becomes difficult to predict in regions where values of k_{s_t} are greater than 0. The phase shift of wave regeneration changes significantly throughout a single tooth period. This can cause chatter to build up during a portion of the tooth period, creating large vibrations, but stabilizing during a different portion of the tooth period. The stability algorithm may trigger a chatter condition due to these intermittent vibrations for a process which is, in fact, stable. Generally, the two stability lobe models do support the existence of the phenomenon which alters the stability border at lower spindle speeds and larger feed rates.

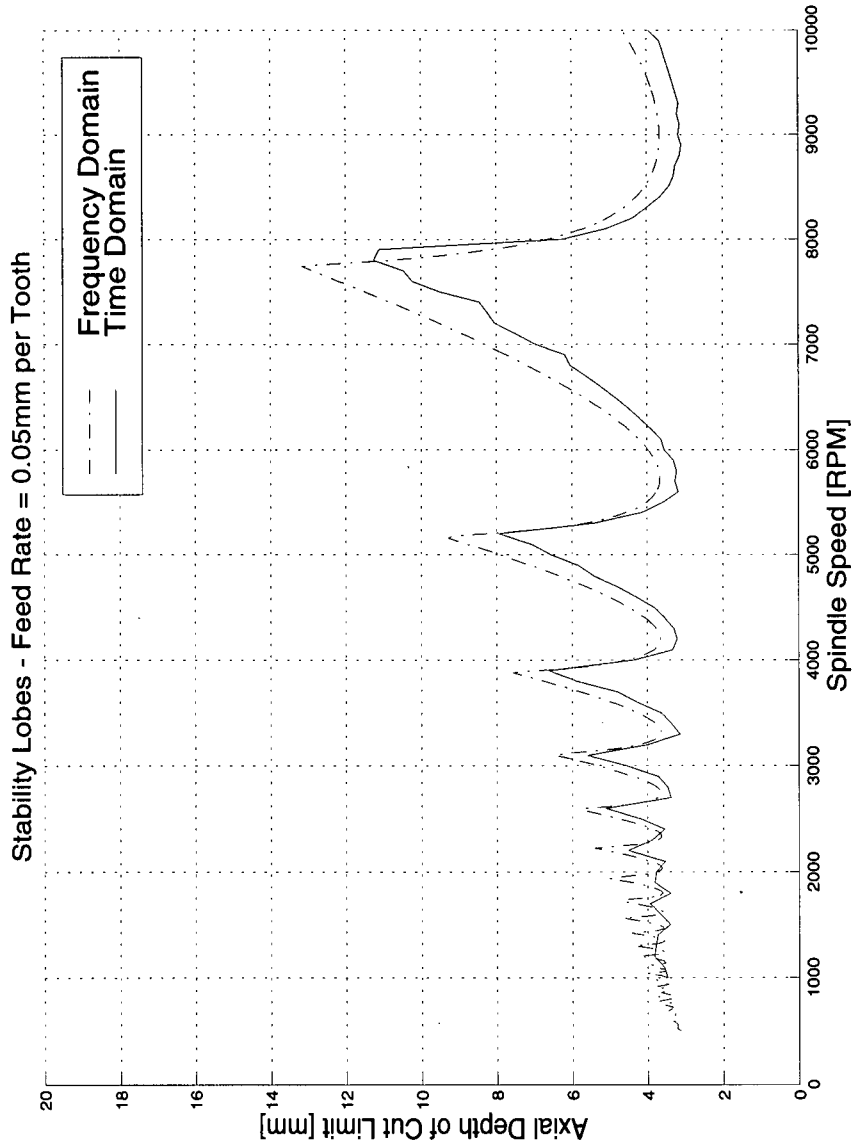

FIGURE 5-26: Predicted stability lobes using time domain and frequency domain simulations with small feed rate

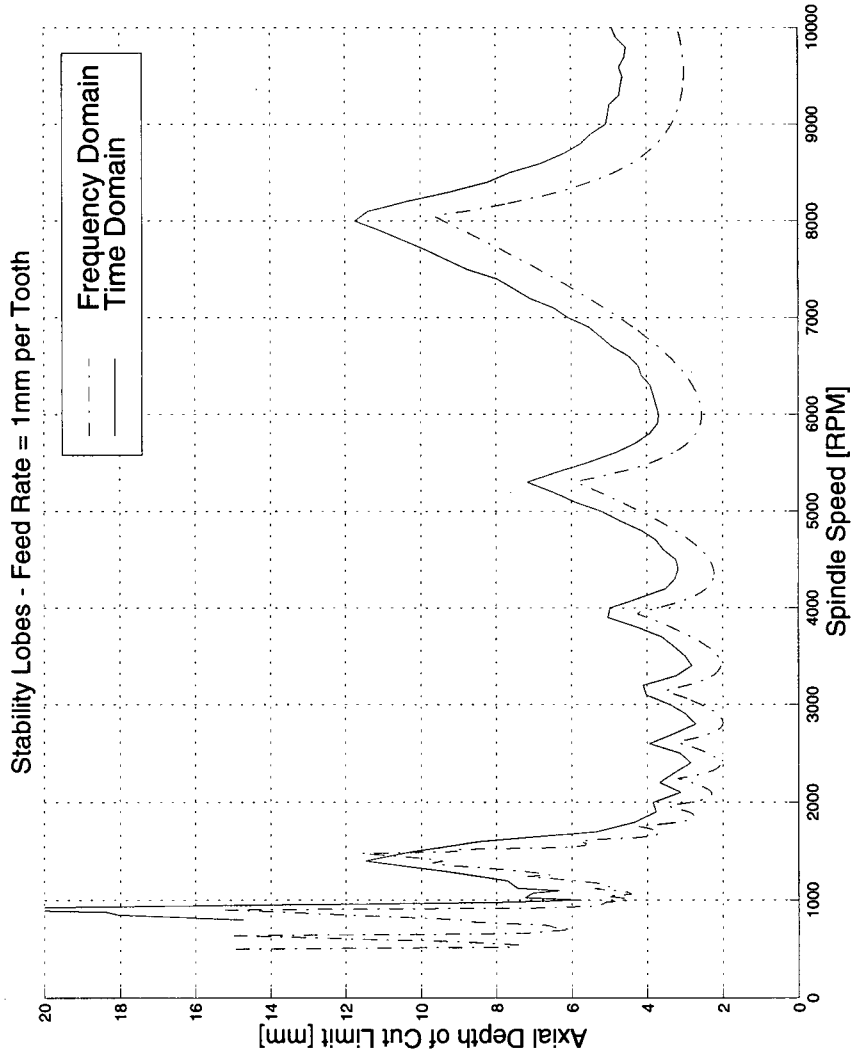

FIGURE 5-27: Predicted stability lobes using time domain and frequency domain simulations with large feed rate

5.6 Summary

In this chapter, two models were presented for evaluating stability lobes in milling. The time domain model offers more realistic predictions, considering more variables such as different dynamics along the axial depth of cut, while the frequency domain model is more practical, given its computational speed.

The good agreement in results from the two models suggests that the increase in stability and secondary lobing effect of the stability border noted at lower spindle speeds is, in fact, due to the effect of feed rate on the regeneration effect. At higher feed rates and lower spindle speeds, when the most flexible mode is relatively high, the feed rate has been shown to greatly affect the stability limit.

To the author's best knowledge, these stability lobe models demonstrate a phenomenon previously undocumented. However, as mentioned above, the conditions in which the effect of feed is most significant are those where process damping also has a stabilizing affect. A more complete model should also include process damping in the prediction of stability lobes.

CHAPTER 6

Experimental Results

6.1 Introduction

In this chapter, some milling experiments are conducted to support some results predicted by the milling simulation described in the preceding chapters. The experimental procedures are given for measuring transfer functions, measuring vibrations, and detecting chatter. The collected measurements are compared to simulation predictions.

The following cutting tests are conducted:

- Chatter stability border is found by cutting at various axial depths of cut for a range of spindle speeds. Chatter was detected by measuring sound frequency spectrum. A flexible machine tool and cutter is used with a rigid workpiece.
- Vibrations are measured when milling a flexible workpiece with a relatively rigid cutter and machine tool. Tests are conducted with both stable and unstable cutting conditions.
- Vibrations are measured at several axial positions of a flexible workpiece while milling to demonstrate the importance of multiple level dynamics when milling flexible structures.

Cutting tests which could not be conducted include machining very flexible workpieces at large depths of cut, and tests to demonstrate the effect of feed rate on stability limit at large

feed rates. The tests were limited primarily due to the availability of equipment at our facilities. The flexibility of the spindle greatly limited stable cutting conditions.

6.2 Experimental Setup

6.2.1 Equipment

All cutting experiments are conducted on a Fadal vertical three axis machining center. A more flexible collet chuck is used for experiments demonstrating chatter from the machine and cutting tool structure, while a stiffer hydraulic chuck is used in cases where a flexible workpiece is the focus.

The cutting tool is a 3/4 inch diameter carbide four fluted helical endmill measuring 52mm from the chuck. The helix angle is 30 degrees. The workpiece material is Aluminum Al7075T651. The cutting parameters for this cutter and workpiece material combination were identified in Chapter 4.

To measure the transfer function of the two structures at various points, an impact force hammer is used in combination with a laser position sensor. A fourier analyzer reads the force and displacement inputs, and provides the response function in a useable form. The transfer functions are also verified using an accelerometer to measure the vibrations, and the force hammer calibration is verified using a force dynamometer. The modal analysis program developed as part of this thesis is used to identify the modal parameters for input to the milling simulations.

Vibrations are also measured of the workpiece during machining. The laser sensor provides workpiece displacement with a resolution of 0.2 μm at a frequency of up to 100 KHz, which is sufficient to measure static deflection and chatter vibrations when machining the flexible workpieces used in the cutting tests below.

While vibrations of the cutting tool cannot be measured during machining, sound pressure levels acquired with a microphone can give an acceptable representation of the vibration fre-

quency spectrum for the purpose of detecting chatter conditions. The microphone is mounted on the machine's spindle casing.

The workpiece vibration and sound pressure level data is acquired using an in-house developed data acquisition system.

During all machining tests, exact spindle speeds are verified using a digital tachometer since the machine sometimes seemed to deviate from its indicated spindle speed by up to 15 percent. The feed rate was verified by timing the motion of the X-Y table over a known distance.

6.2.2 Measuring Machine Tool and Cutter Dynamics

The machine and cutting tool dynamics are measures in the X (feed) and Y (normal) directions with both the collet chuck and the hydraulic chuck at various axial positions measured from the tip of the cutter. The measured and identified transfer functions are shown in Figures (6-1) to (6-4), with the modal parameters listed in Tables (6-1) to (6-4).

From the measurements, it seems that the highest frequency modes originate from the cutting tool, judging from the mode shapes diminishing rapidly as the measurement is taken closer to the chuck. All other modes originate either from the spindle or from the chuck. With either chuck, the dominant natural frequency of the entire structure is below 1000 Hz.

FIGURE 6-1: Transfer Function of Machine Tool with Collet Chuck in X Direction

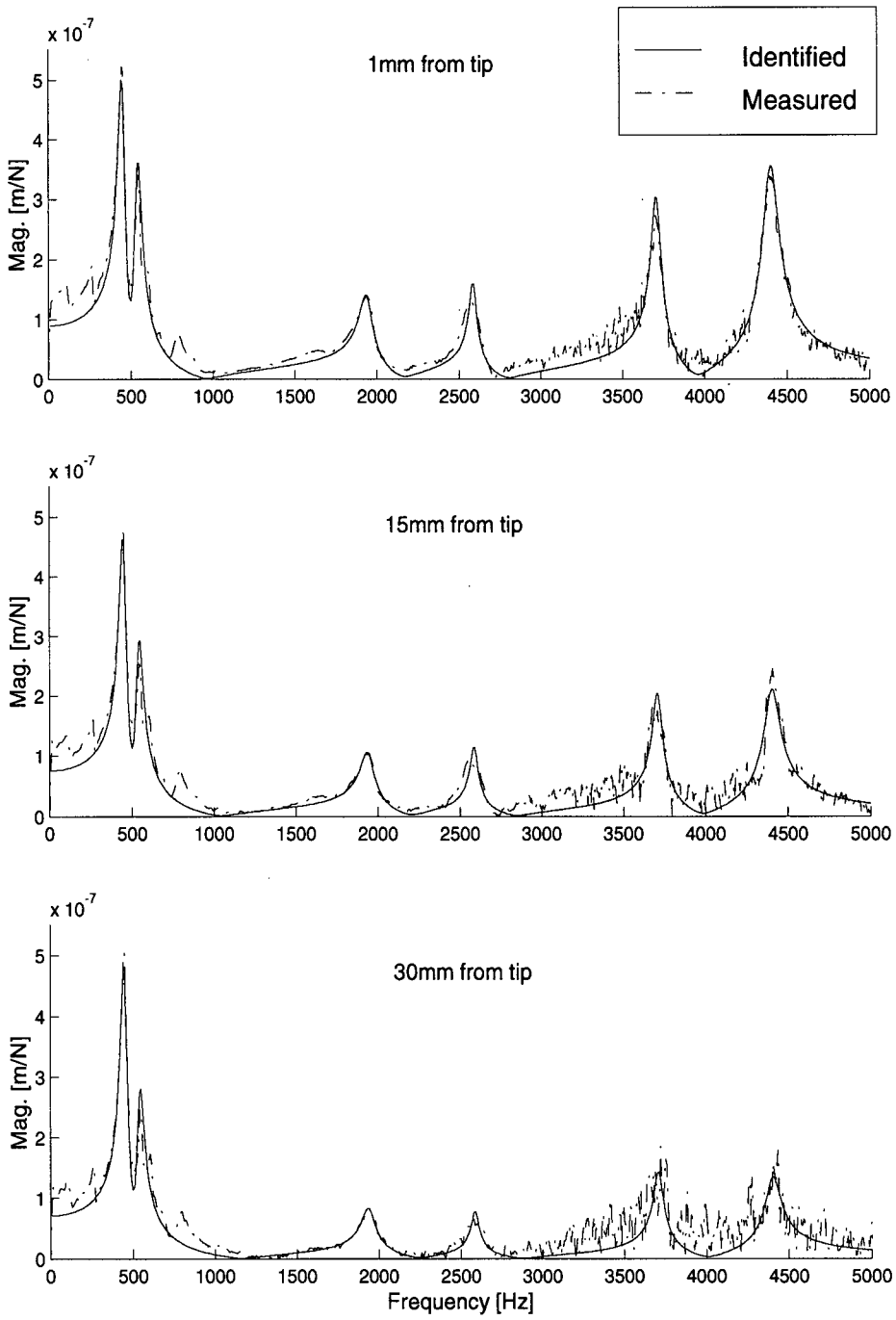

FIGURE 6-2: Transfer Function of Machine Tool with Collet Chuck in Y Direction

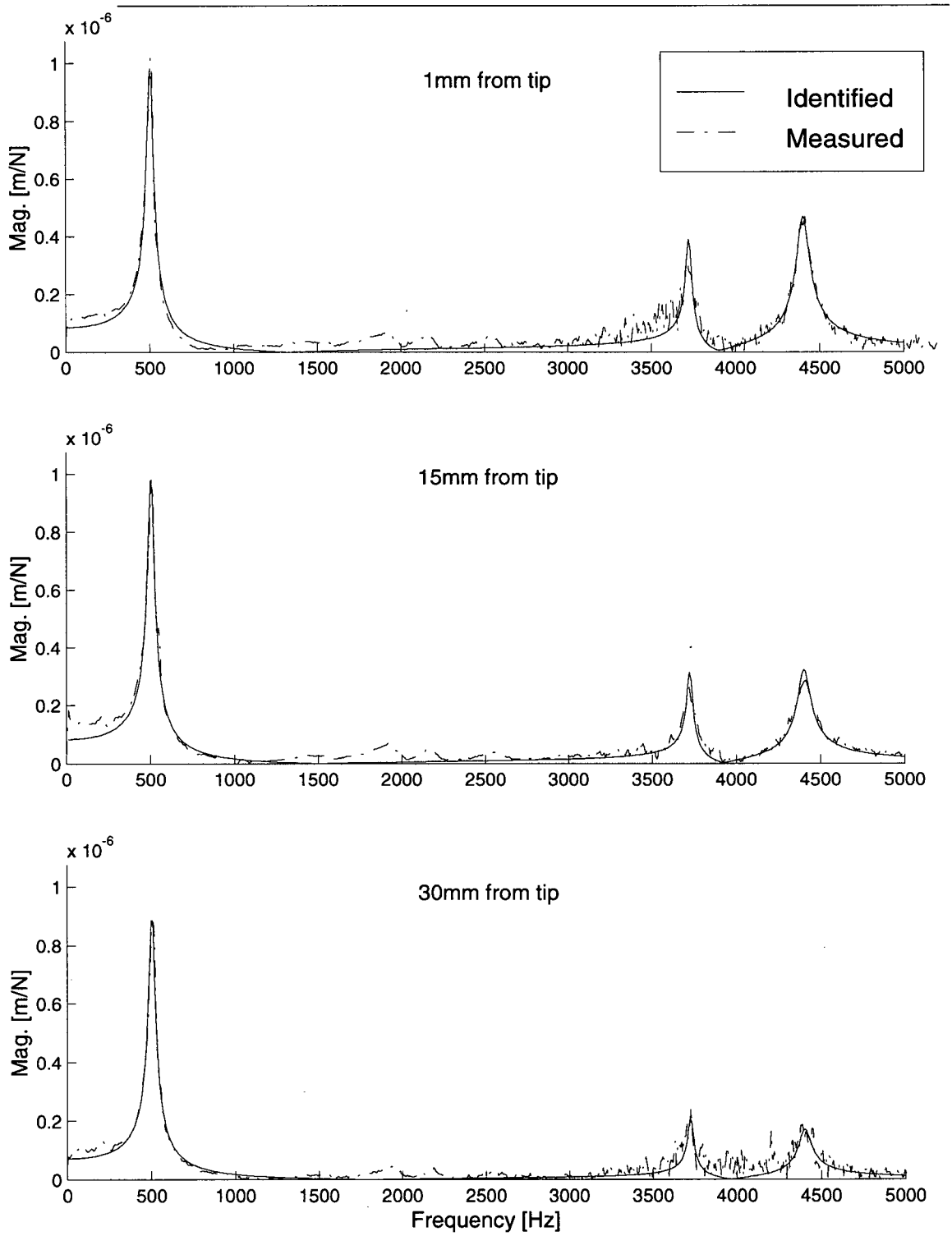

TABLE 6-1: Identified Modal Parameters of Tool with Collet Chuck in X Direction

	ω_n [Hz]	ζ	Mode Shape Coefficients $u_p \left[\frac{m}{Nrad^2}\right]$		
			1mm from tip	15mm from tip	30mm from tip
Mode 1	448.55	0.04439	0.5763567	0.5447158	0.5614634
Mode 2	543.05	0.03964	0.5637977	0.4439832	0.4152877
Mode 3	1938.61	0.02125	0.9324049	0.7136577	0.5595399
Mode 4	2587.06	0.00894	0.8712094	0.6256292	0.4226089
Mode 5	3706.60	0.00786	1.61243	1.084459	0.7606145
mode 6	4400.72	0.01054	2.393511	1.41792	0.9025841

TABLE 6-2: Identified Modal Parameters of Tool with Collet Chuck in Y Direction

	ω_n [Hz]	ζ	Mode Shape Coefficients $u_p \left[\frac{m}{Nrad^2}\right]$		
			1mm from tip	15mm from tip	30mm from tip
Mode 1	504.77	0.03749	0.8653921	0.8682728	0.7869819
Mode 2	3723.44	0.00444	1.378824	1.112611	0.7391905
Mode 3	4401.18	0.00827	2.436991	1.679445	0.888594

FIGURE 6-3: Transfer Function of Machine Tool with Hydraulic Chuck in X Direction

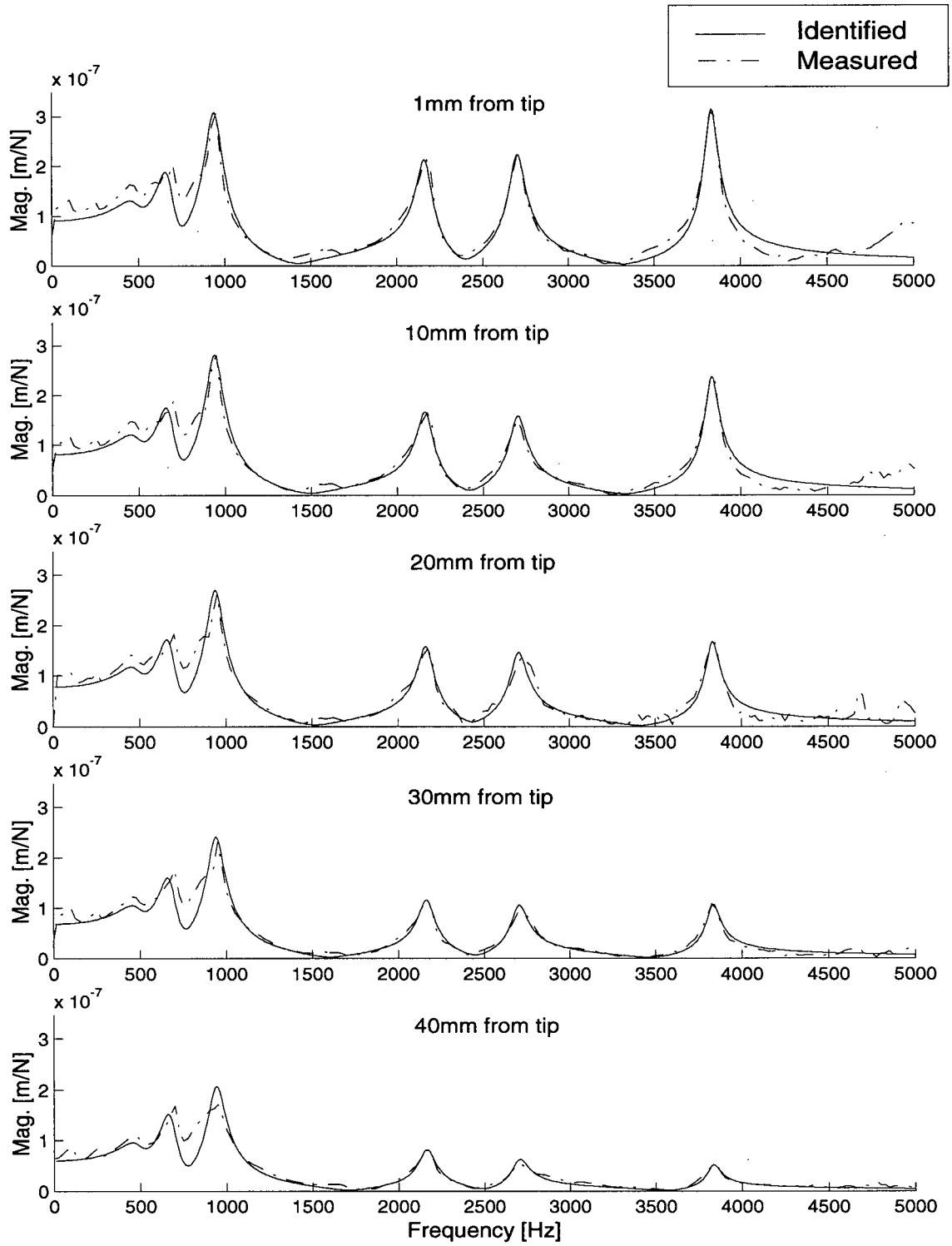

FIGURE 6-4: Transfer Function of Machine Tool with Hydraulic Chuck in Y Direction

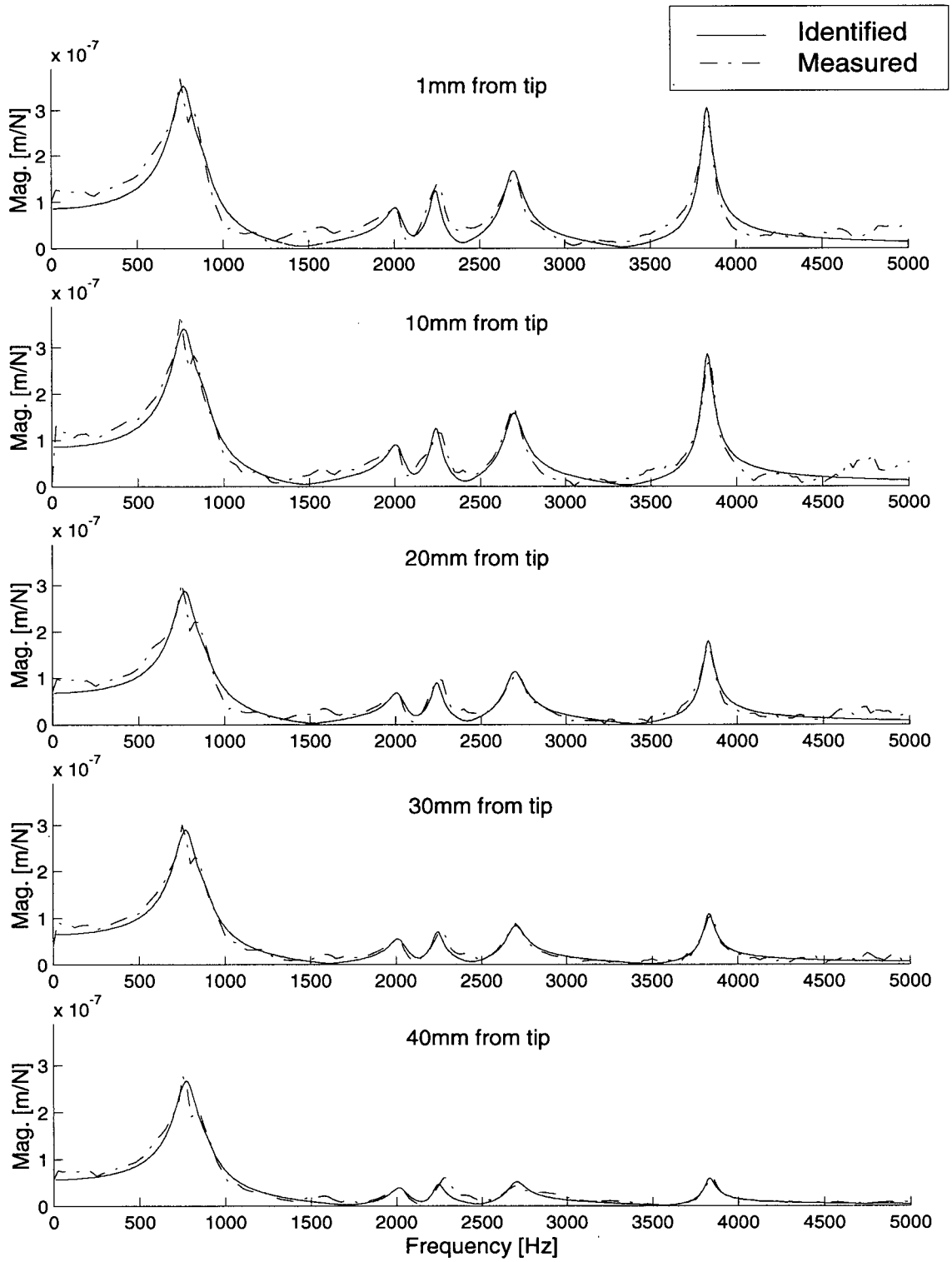

TABLE 6-3: Identified Modal Parameters of Tool with Hydraulic Chuck in X Direction

Mode	ω_n [Hz]	ζ	Mode Shape Coefficients $u_p \left[\frac{m}{Nrad^2}\right]$				
			1mm from tip	10mm from tip	20mm from tip	30mm from tip	40mm from tip
1	489.35	0.15417	0.6155902	0.5934756	0.5925653	0.569762	0.5642318
2	674.93	0.07542	1.082521	0.9891729	0.948205	0.8434781	0.7240363
3	940.45	0.05555	1.287716	1.01607	0.9630499	0.7088588	0.5036081
4	2166.84	0.02153	1.499191	1.06317	0.9812605	0.7027502	0.4173261
5	2702.33	0.01767	1.935752	1.46074	1.026994	0.6539803	0.3144709
6	3830.16	0.01028	0.3505993	0.3550908	0.3523078	0.322933	0.3188513

TABLE 6-4: Identified Modal Parameters of Tool with Hydraulic Chuck in Y Direction

Mode	ω_n [Hz]	ζ	Mode Shape Coefficients $u_p \left[\frac{m}{Nrad^2}\right]$				
			1mm from tip	10mm from tip	20mm from tip	30mm from tip	40mm from tip
1	870.33	0.07176	0.5533035	0.6653421	0.3883336	0.3959651	0.2966715
2	781.31	0.09098	1.183442	1.116723	0.9792922	0.9897918	0.9288155
3	2018.54	0.02420	0.775986	0.7922623	0.6057444	0.5151184	0.3687343
4	2243.02	0.01379	0.8060596	0.812733	0.5746959	0.4503108	0.2942135
5	2697.00	0.02023	1.388321	1.311003	0.9376124	0.6888171	0.4167447
6	3829.42	0.00831	1.71497	1.603707	1.003849	0.610735	0.3272502

6.2.3 Detecting Chatter

Some of the most practical results of milling simulations are those which determine the borderlines between stable conditions and those dominated by chatter vibrations. To evaluate the simulated results, it is important to be able to systematically categorize each cutting experiment as stable or unstable. When machining a flexible workpiece, it is possible to measure the vibrations and static deflections of the workpiece with a displacement sensor.

The frequency spectrum of the vibration data can indicate whether or not the condition is stable. A more practical method is to use sound pressure level to approximate this data. The frequency spectrum of sound pressure level should, in most cases, offer an accurate enough representation of vibrations for the purpose of detecting chatter conditions. Furthermore, vibrations from both the machine tool and the workpiece are captured.

As with the simulation results, assessing measured vibration data requires a systematic approach which can greatly affect the end result. For simulations, the predicted maximum dynamic chip thickness is compared to the maximum static uncut chip thickness to determine whether or not chatter exists. Since this is not possible with experimental tests, an alternate approach is required.

After cutting at several different cutting conditions with and without chatter, many observable signs offered obvious indications of chatter, including large wave patterns on the finished surface and existence of distinctly loud audible vibrations. When analyzing the frequency spectrum of the sound pressure level, chatter conditions are characterized by large amplitudes at one or more natural frequencies of the machine or workpiece in comparison to the tooth frequency and its harmonics. For chatter tests in this thesis, stability of a cutting test is categorized into *stable*, *light chatter* and *chatter*. The criteria for determining stability is as follows:

- *Stable*: the sound pressure level amplitudes at the tooth frequency and/or its harmonics are clearly dominant in comparison to the amplitudes at the system's natural frequencies
- *Light Chatter*: the sound pressure level amplitudes at one or more of the system's natural frequencies are from 1 to 2 times in magnitude in comparison to the amplitudes at the tooth frequency and/or its harmonics
- *Chatter*: the sound pressure level amplitudes at one or more of the system's natural frequencies are over 2 times in magnitude compared to the amplitudes at the tooth frequency and/or its harmonics

The sound pressure level frequency spectrum of three sample cutting tests are shown in Figures (6-6) through (6-7) for stable, light chatter, and chatter cases.

FIGURE 6-5: Sound Pressure Level Frequency Spectrum (Stable)

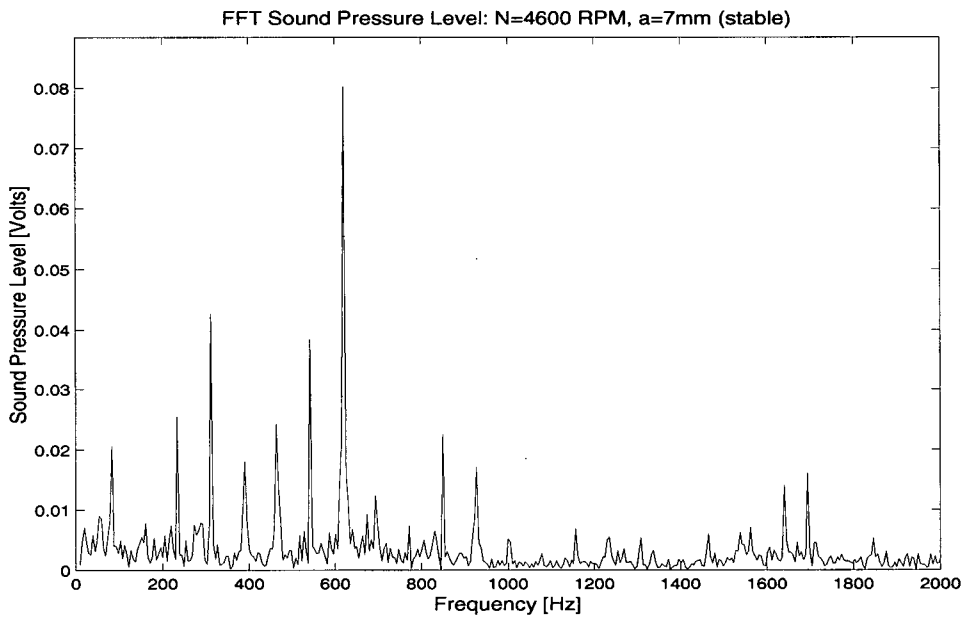

FIGURE 6-6: Sound Pressure Level Frequency Spectrum (light chatter)

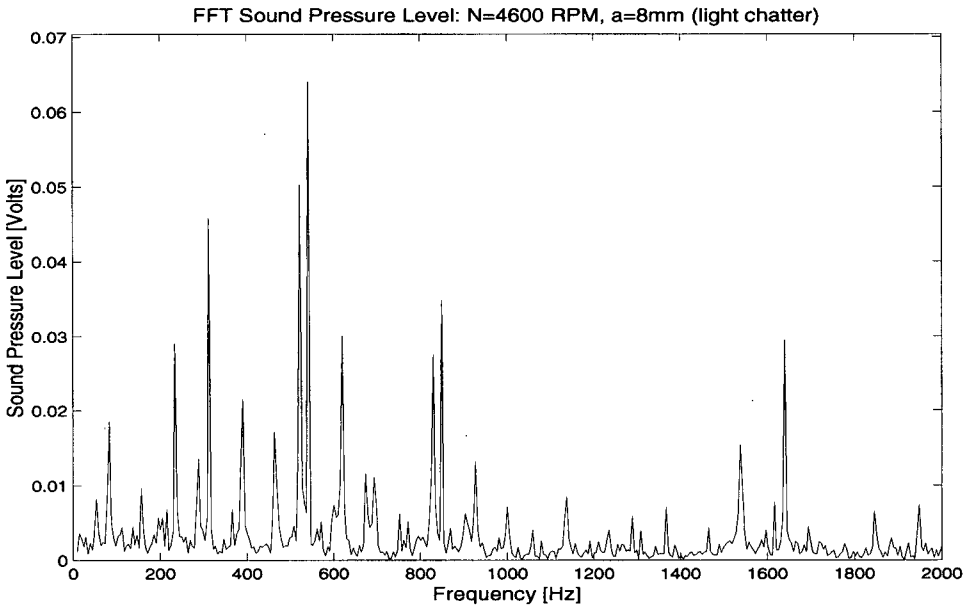

FIGURE 6-7: Sound Pressure Level Frequency Spectrum: (chatter)

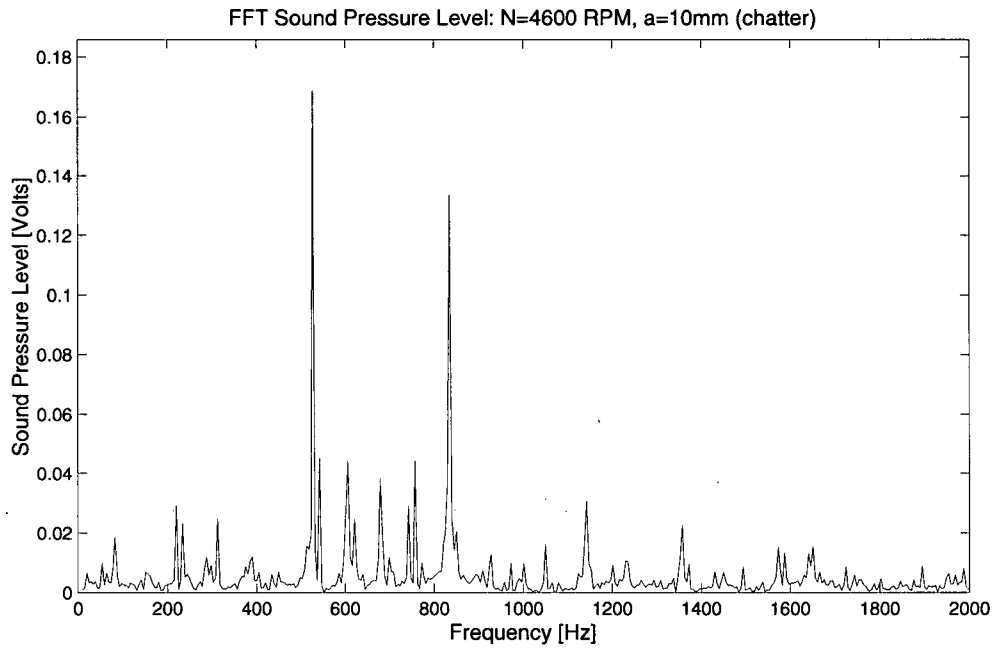

6.3 Chatter Stability Lobes

This section compares several predicted stability lobes with experimental cutting tests. Three predictions are included: 1) stability lobes from time domain simulations, which includes varying dynamics along the axial depth, effect of feed rate, forced vibrations, helix angle, among other effects, 2) frequency domain stability lobes, which includes the effect of feed rate, and 3) stability lobes using the method of Altintas and Budak [49], which does not include the effect of feed rate. The simulation results in Figure (6-8) show good agreement between the different predictions. Since chatter is caused by the spindle and chuck modes, the varying dynamics along the axial depth does have a significant impact. Furthermore, since the chatter vibrations are at a relatively low frequency, k_{s_t} is well below 1 for the spindle speed range shown. Hence, the effect of feed rate in under these conditions are also negligible, shown by the close agreement between the frequency domain solution described in this thesis and the lobes by Budak and Altintas.

Figure (6-9) shows good agreement between the predicted stability limit and experimental cutting tests. The experimental results show lobes shifted slightly to the left relative to the predicted lobes. Some measurement error may exist in acquiring natural frequency of the machine tool. Generally, some discrepancy between simulated and experimental stability lobes is expected. Some sources of error are listed below:

- Different criteria for determining stability: A different stability criterion was used for detecting chatter from cutting tests than from simulated results. This involved a completely different approach with different data; sound pressure level versus oscillating force amplitudes. This most likely accounts for most of the error between predicted and experimental stability lobes.
- Transfer function accuracy: The transfer functions are critical in determining the location, shape, and height of the lobes. There are many data acquisition and numerical FFT processing variables involved which can alter the results. Furthermore, dynamic characteristics are approximated by a linear model which can cause significant error when modelling a complex structure such as a spindle.
- Forced vibrations may trigger a chatter condition: When the tooth frequency and its harmonics are close to a natural frequency of the system, it can be difficult to distinguish between forced vibrations and chatter vibrations. The different criteria used to detect chatter will handle such circumstances differently.
- Cutting force coefficients used in the simulation were conducted at a spindle speed of 2000 RPM, which corresponds to a cutting speed of 120 m/min. As the spindle speed changes, the cutting forces may vary with changing cutting speed. Ideally, the simulation program would interpolate from a database of cutting force coefficients at several different cutting speeds.

FIGURE 6-8: Predicted Chatter Stability Lobes: Collet Chuck and Rigid Workpiece

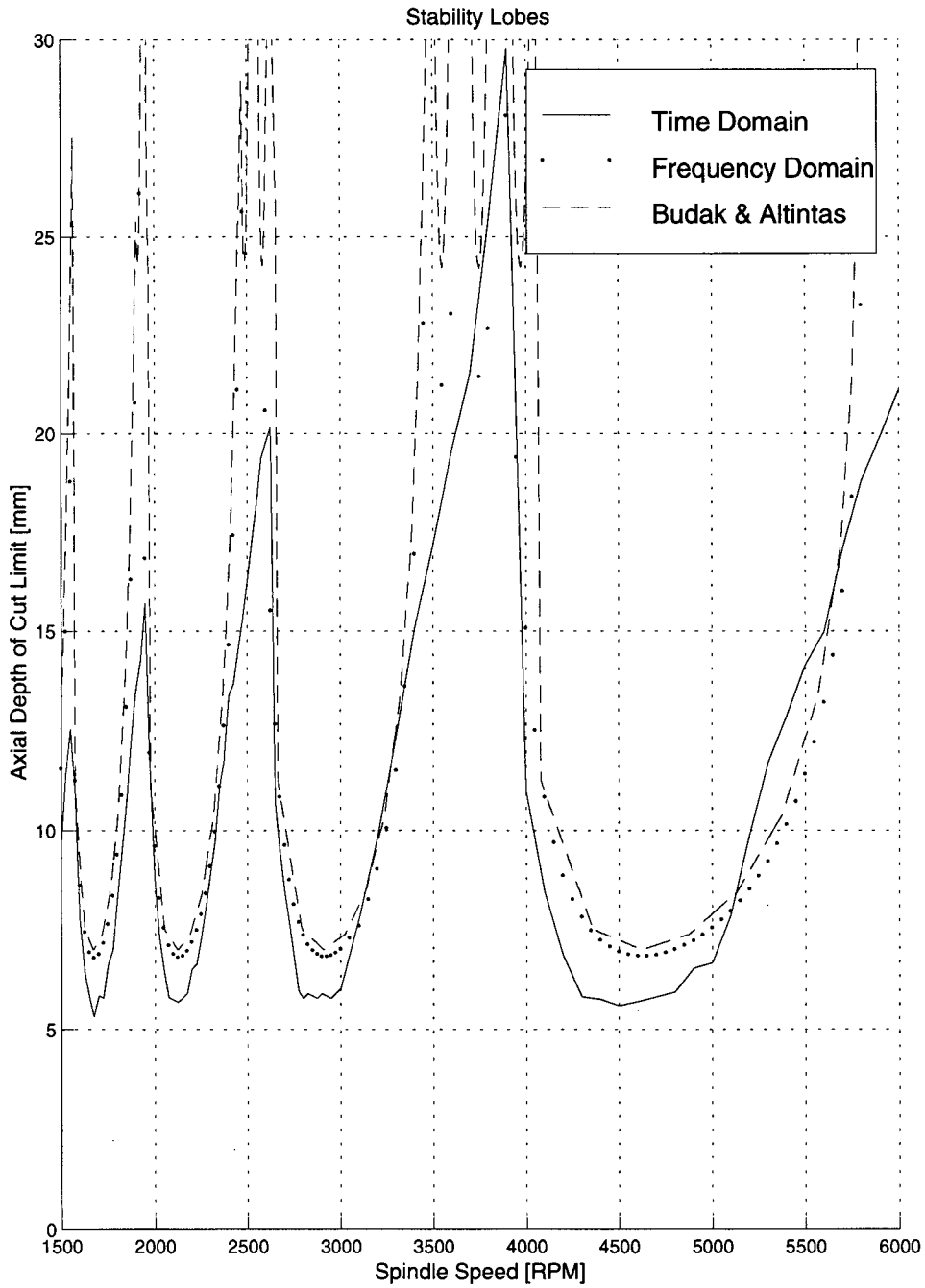

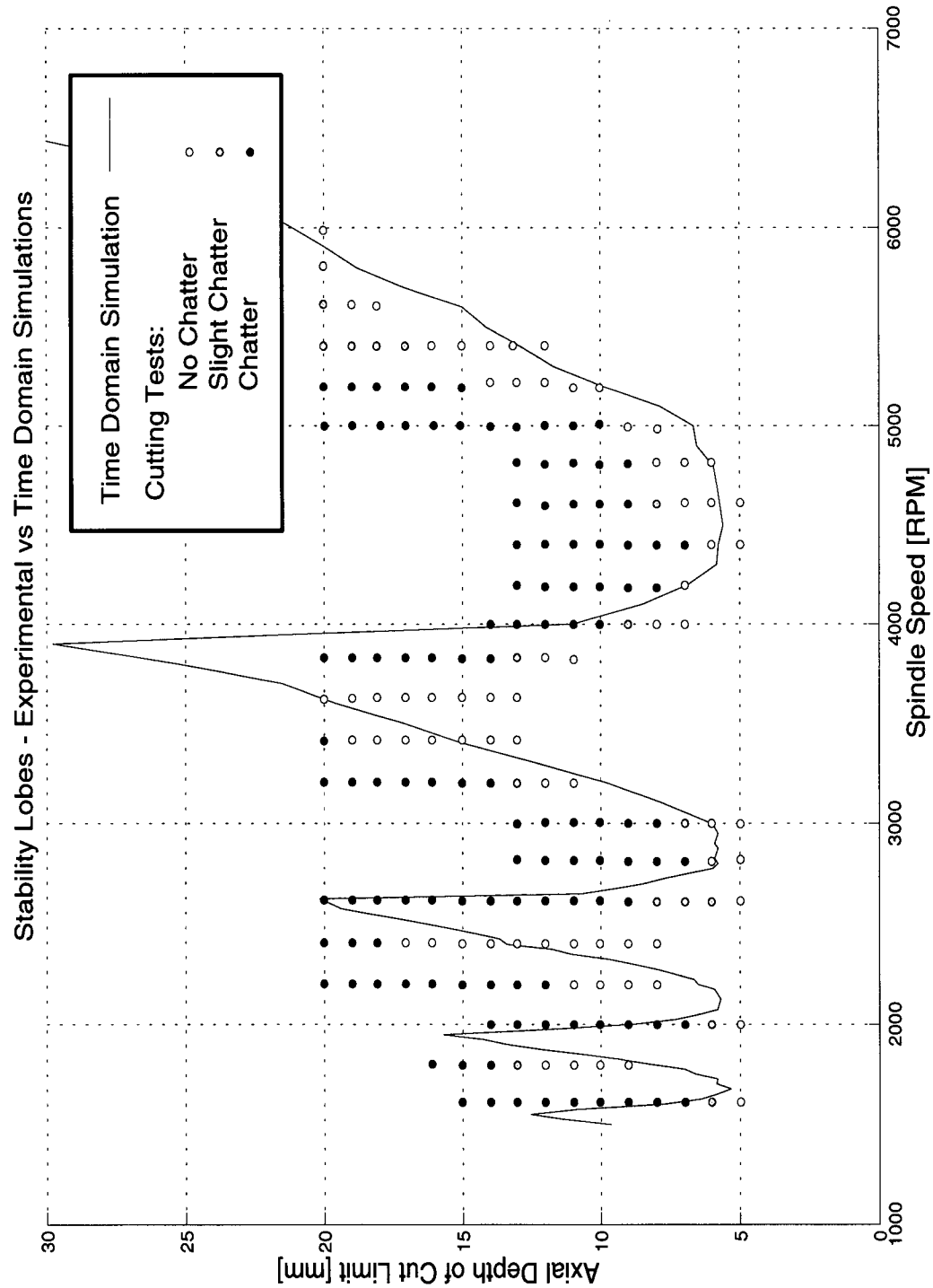

FIGURE 6-9: Experimental vs Time Domain Simulation Stability Lobes: Collet Chuck and Rigid Workpiece

6.4 Milling a Flexible Workpiece

The next set of cutting tests focus on milling in which the most flexible mode originates from the workpiece. The more rigid hydraulic chuck is used and the workpiece is a rectangular flexible aluminum plate, fixed at one edge and left free to move at the remaining three edges. A laser position sensor is mounted to measure displacement at the center tip of the plate during machining.

The cutting tests are compared with simulation results. The dynamic characteristics of the machine tool and cutter were identified above. The workpiece material is Al7075T6 with cutting coefficients determined from Chapter 4. Runout is neglected in these simulations.

The workpiece dimensions are chosen such that its most flexible mode is in the Y direction and flexibility in the X (feed) direction is negligible. The workpiece dimensions are 104mm high (Z) by 93mm (X) wide by 26mm thick (Y). Since the depth of cut will be small compared to the height of the plate, a single transfer function measurement is sufficient at the tip of the plate. A feed rate of 0.5 mm/tooth is used. The measured and identified transfer functions are shown in Figure (6-10). The identified parameters are listed in Table (6-5).

TABLE 6-5: Identified Modal Parameters of Workpiece in Y Direction

Mode	ω_n [Hz]	ζ	Mode Shape Coefficients $u_p \left[\frac{\text{m}}{\text{Nrad}^2}\right]$
			1mm from tip
1	1047.82	0.03852	1.739939

The predicted chatter stability lobes are shown in Figure (6-11). Since the dynamics of the workpiece change with the removal of material, the number of tests on the workpiece for which the above dynamics are valid, are limited. Three points are selected, labelled A, B, and C on the stability chart, showing stable and unstable milling conditions at two depths of cut and two spindle speeds. Vibrations at the tip of the flexible plate are measured during

FIGURE 6-10: Measured and Identified Transfer Function of Workpiece in Y Direction

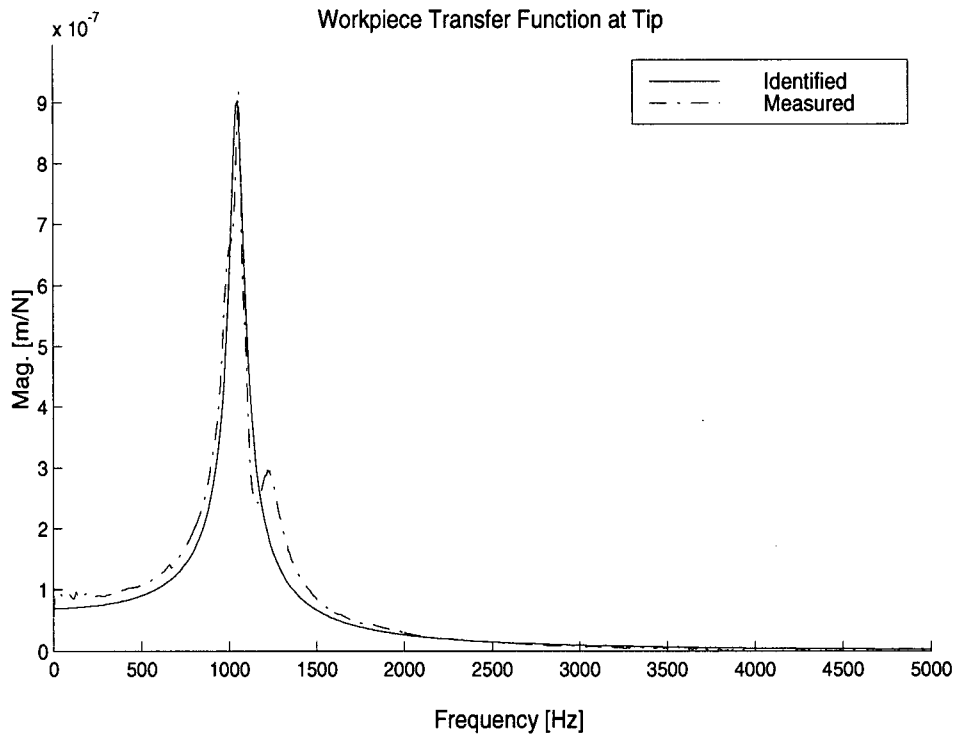

the milling tests. The measured and predicted plate displacement is plotted in time and frequency domains in Figures (6-12) through (6-17).

The results show excellent agreement between experimental and simulated workpiece vibrations, particularly in cases A and B. In case A, the tooth frequency and its harmonics are highest, with small amplitudes at the principal natural frequency of the workpiece. In case B, the conditions are unstable and vibrations grow in a similar pattern between predicted and experimental plots, until a steady state amplitude is reached at a chatter frequency very near the natural frequency of the workpiece. There is some difference in the predicted and measured steady state vibrations, but under such unstable conditions, accurately predicted steady state amplitude of vibrations should not be expected. In case C, it seems that a torsional mode at approximately 1500 Hz was excited in the experiment, which was not accounted for in the simulation. In this case, the second harmonic of the tooth frequency is at 1000 Hz, which is very close to the natural frequency of the plate. Despite the large amplitude at 1000 Hz, both the cutting test and the simulation showed clear signs stable conditions.

FIGURE 6-11: **Predicted Stability Lobes (Freq. Domain Model) - Machining Flexible Plate**

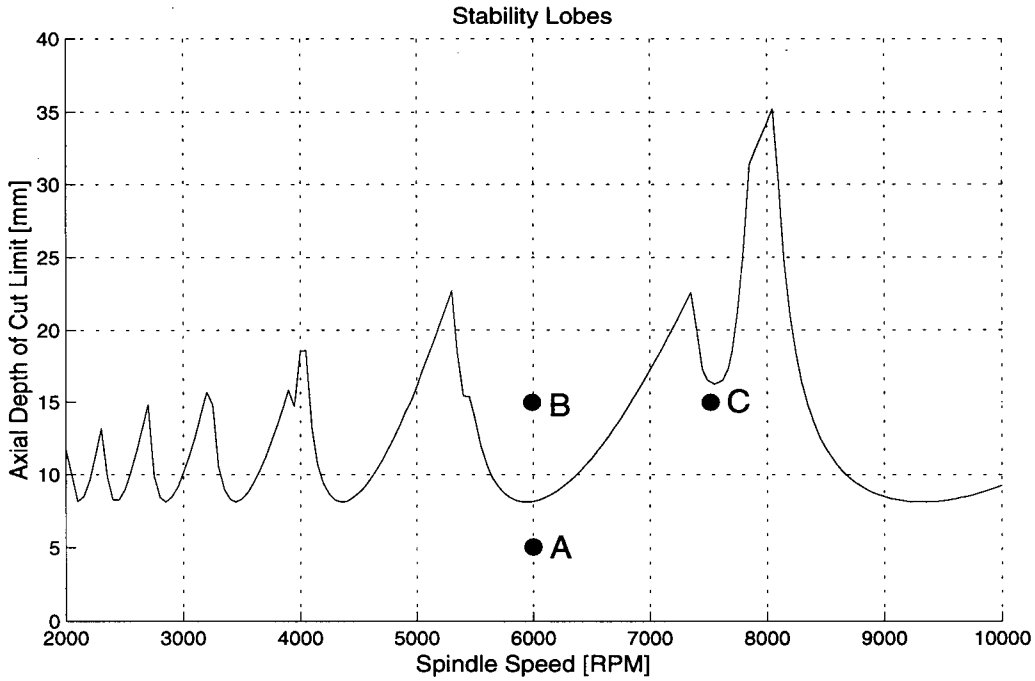

FIGURE 6-12: Workpiece Vibrations at Tip of Plate for Cutting Conditions at Point A

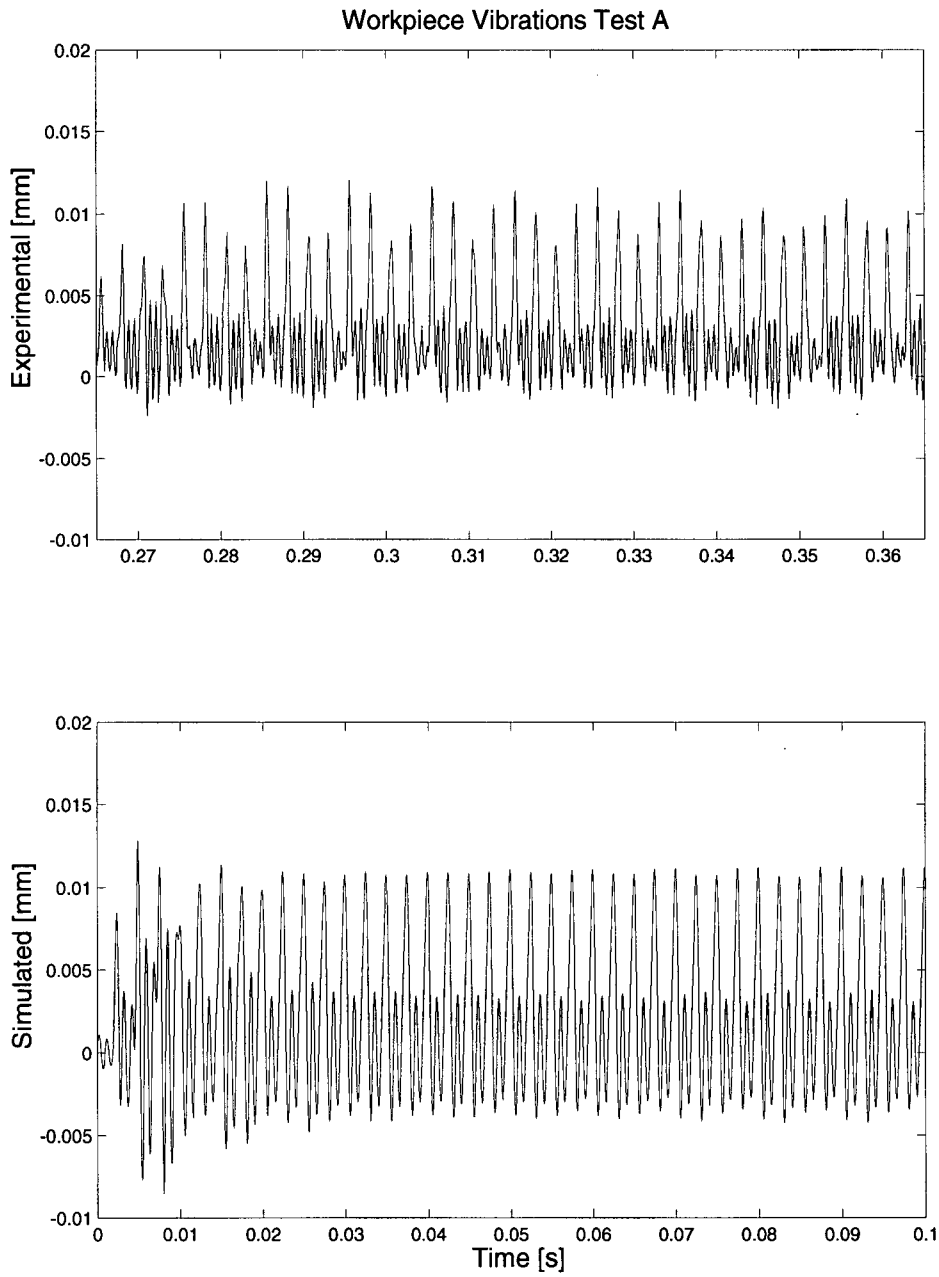

FIGURE 6-13: Frequency Spectrum of Workpiece Vibrations at Tip of Plate for Cutting Conditions at Point A

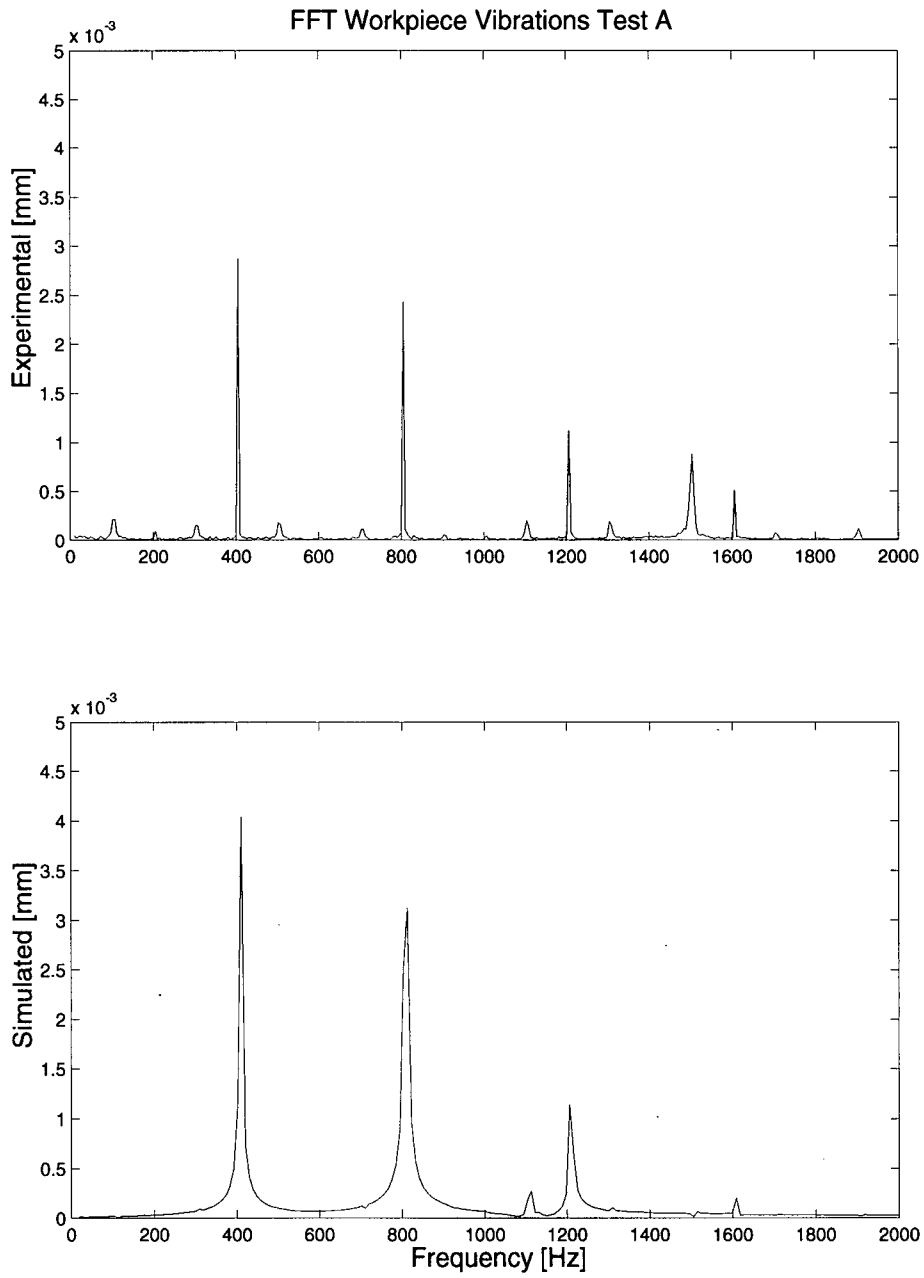

FIGURE 6-14: Workpiece Vibrations at Tip of Plate for Cutting Conditions at Point B

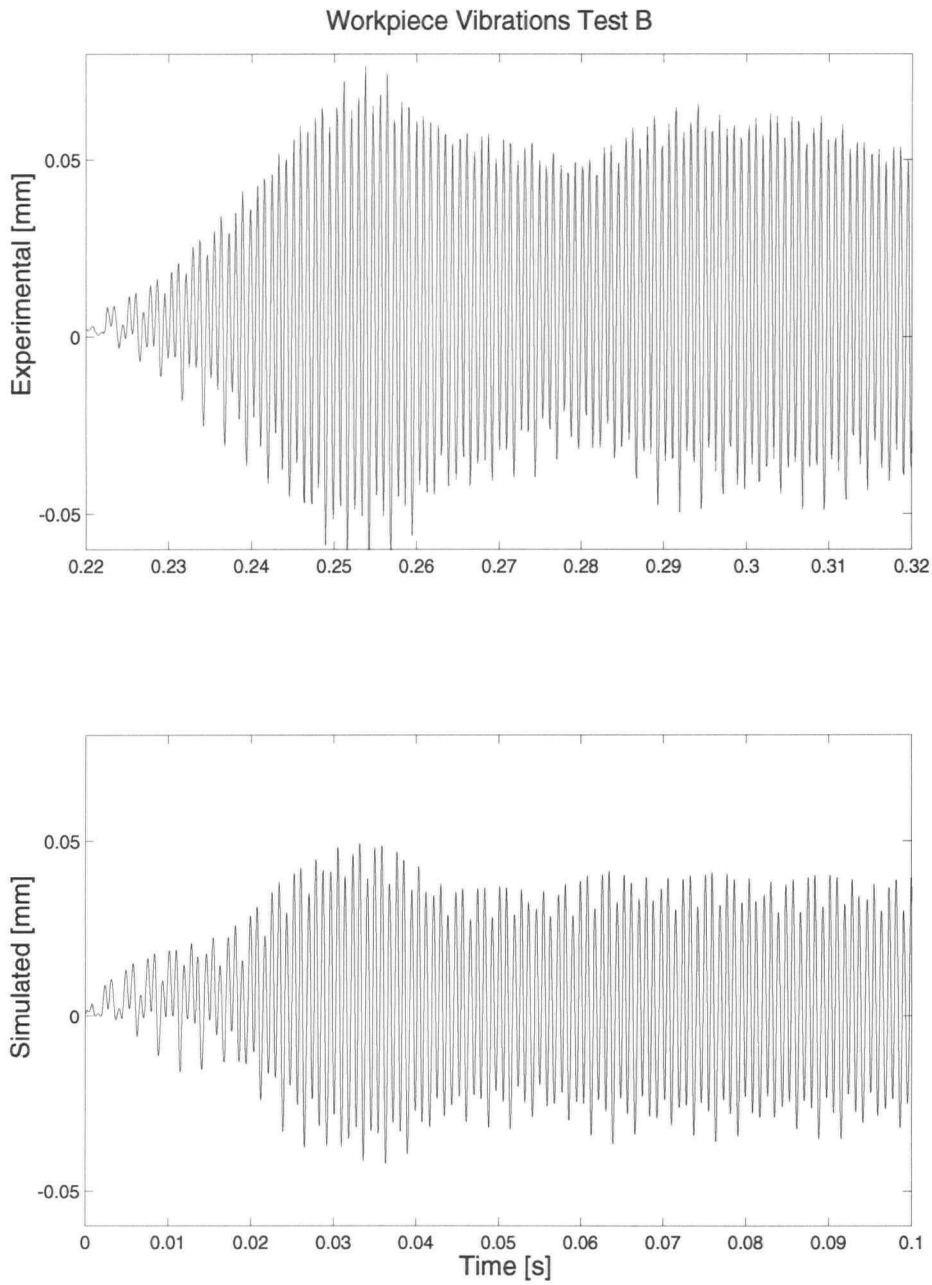

FIGURE 6-15: Frequency Spectrum of Workpiece Vibrations at Tip of Plate for Cutting Conditions at Point B

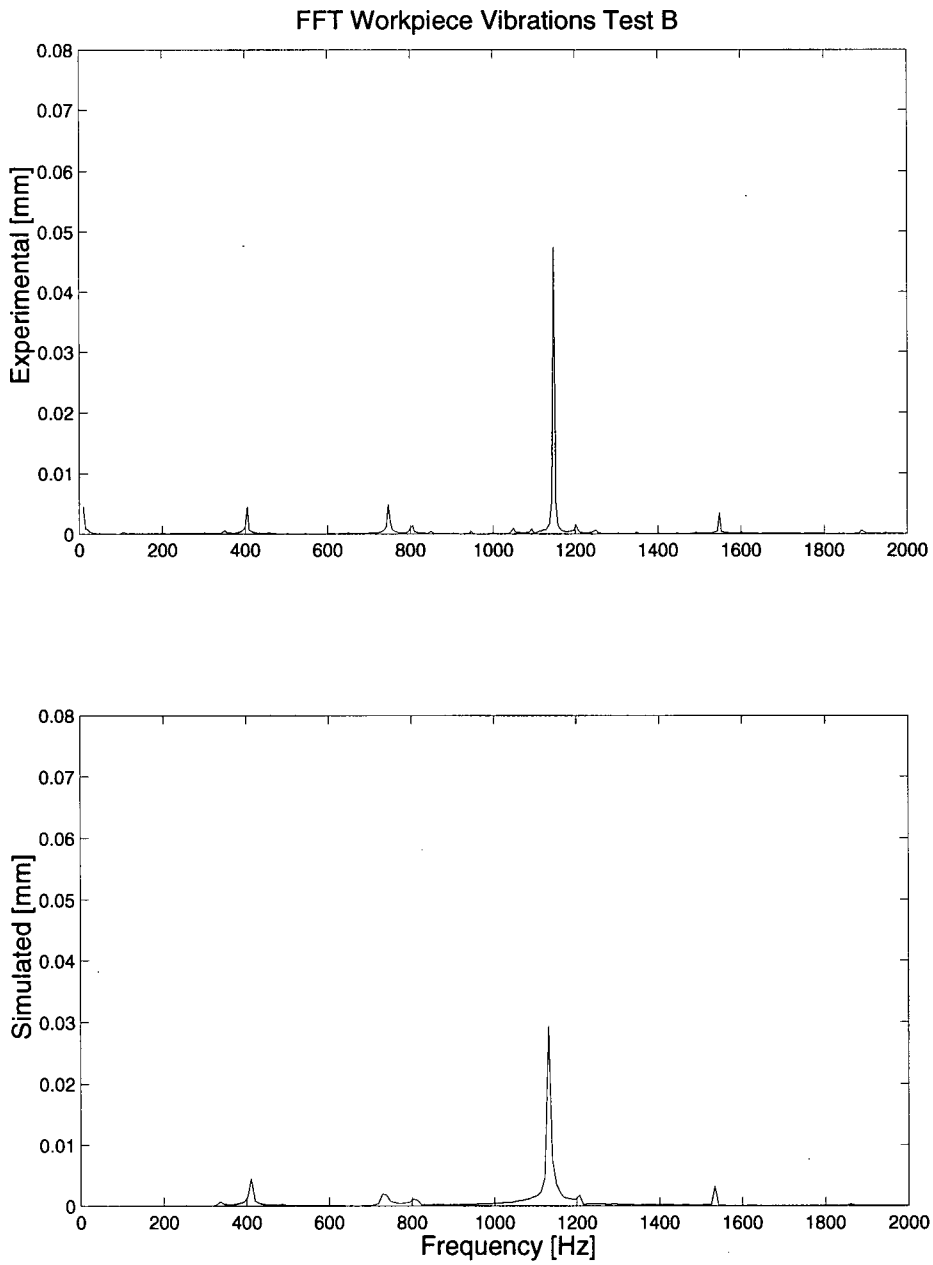

FIGURE 6-16: Workpiece Vibrations at Tip of Plate for Cutting Conditions at Point C

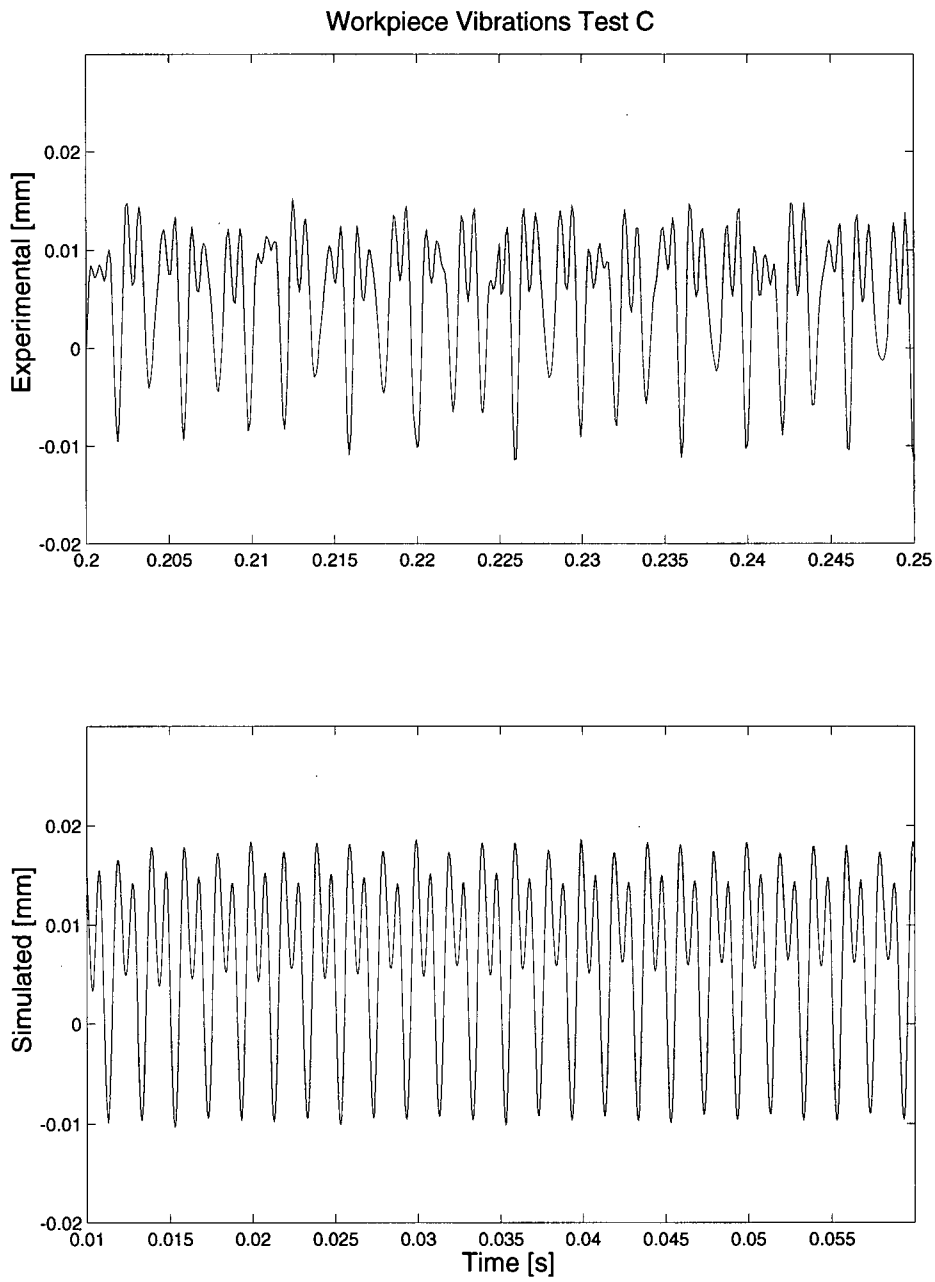

FIGURE 6-17: Frequency Spectrum of Workpiece Vibrations at Tip of Plate for Cutting Conditions at Point C

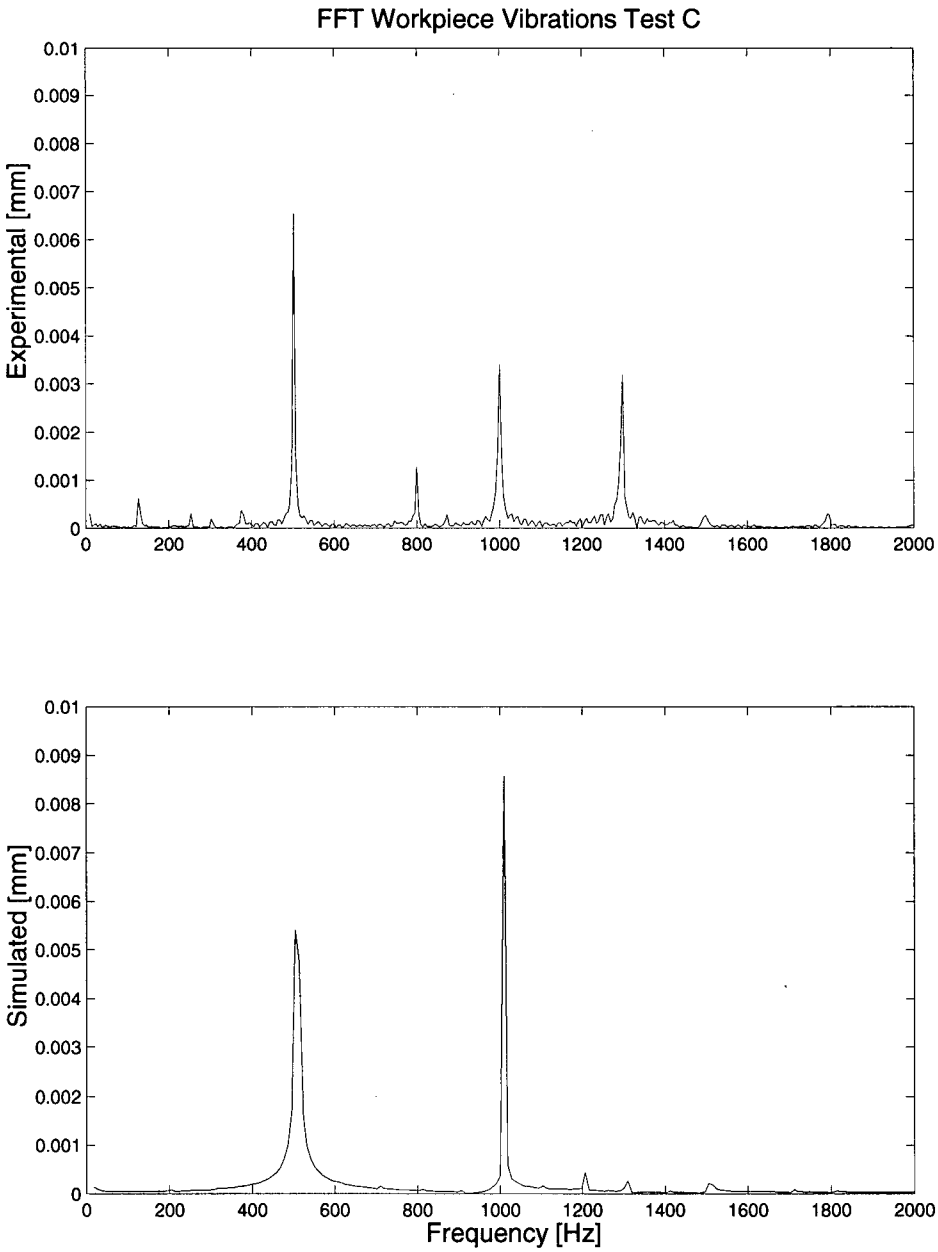

6.5 Importance of Multiple Level Dynamics with Large Depths of Cut

6.5.1 Overview

One of the advantages of the milling model used in this thesis over most other milling simulations, is the use of varying dynamics along the axial depth of cut. It is common to model the cutting tool and the workpiece with lumped dynamic parameters at the structure's most flexible point. Consider the case when machining at large depths of cut with a long slender flexible endmill, or when machining a workpiece in which the flexibility varies along the axial depth of cut, such as a flexible plate. Modelling the dynamics of these structures using a single lumped transfer function can give misleading results. The increased stiffness near the base of the plate and of the cutter near the chuck remains unaccounted for. Simulation results would give less stable conditions and erroneous finished surface profiles. Under these conditions, it becomes very important that varying dynamics are considered at different axial positions.

Ideally, the significance of using multiple level dynamics could be well illustrated by conducting cutting tests and comparing the results with those from the simulation using multiple point dynamics and from the simulation using single point dynamics. Unfortunately, given the limited available machinery at our facilities, the axial depth of cut was limited by the flexibility of the spindle. A cutter and workpiece geometry combination was not found which would create the conditions necessary to properly demonstrate the importance of this feature. In most cases, the vibrations were dominated by a mode originating from the flexibility of the spindle. This pivoting motion about the spindle bearing offered no significant variation in dynamics along the axial depth of cut. More flexible workpieces and cutters resulted in too small an allowable depth of cut before chatter occurred.

The difference in single versus multiple level dynamics are better presented with simulation results of some hypothetical cutting conditions. Chatter stability lobes are shown for both cases. Experimental verification of the model is provided by measuring vibrations at different points along a flexible workpiece. For this test, however, the depth of cut had to be kept

small relative to the height of the plate. The measured vibrations are compared to simulation results.

6.5.2 Measured Transfer Functions of Flexible Workpiece

The flexible workpiece used for tests in this section is the stepped plate shown in Figure (6-18). The workpiece is tapered at the clamped end to increase flexibility and so the torsional and higher frequency modes become less significant. The top of the plate is much thicker so the metal removed during the cutting tests does not significantly alter the structure's natural frequency.

FIGURE 6-18: Workpiece geometry

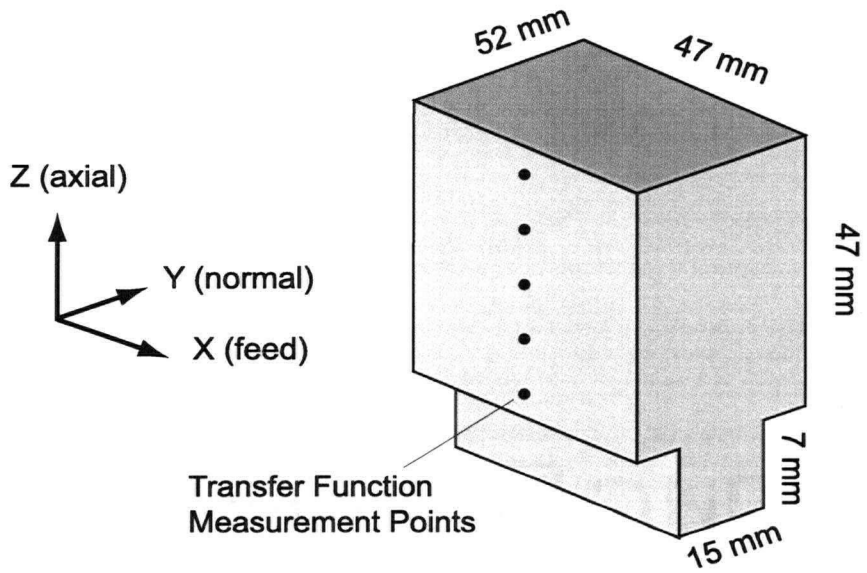

The transfer function is measured at five points along the height of the plate. The transfer functions and identified parameters are shown in Figure (6-19) and Table (6-6).

TABLE 6-6: Identified Multiple Level Dynamic Parameters of Flexible Workpiece

	ω_n = 1494 Hz, ζ = 0.0205
Location [mm] from tip	**Mode Shape Coefficients** $u_p \left[\frac{\text{m}}{\text{Nrad}^2}\right]$
5	1.735151
15	1.349193
25	1.214139
35	0.9484854
45	0.5650185

6.5.3 Simulated Chatter Stability Lobes

In the following simulations, the chatter stability limit is predicted for several cases using the flexible workpiece dynamics identified above and the cutter/machine tool dynamics with the hydraulic chuck. First, stability lobes are predicted considering both workpiece and cutter dynamics. Next, in order to better demonstrate the effect of using multiple level dynamics, the machine tool and cutter are assumed to be rigid relative to the flexibility of the workpiece.

A radial width of cut of 1.0 mm is used with a feed rate of 0.1 mm per tooth. The cutter geometry and force coefficients are the same as those used in previous simulations and experiments.

Figure (6-20) shows the predicted stability lobes using both workpiece and machine tool dynamics. The predictions are made using time domain simulations since the frequency domain model developed in this thesis only considers lumped workpiece and machine tool dynamics. In this particular case, there is not a great difference between the two simulations. At larger depths of cut, when the use of multiple point dynamics should be more significant, the allowable depth of cut is most likely limited by spindle vibrations, which are relatively constant along the length of the cutter.

FIGURE 6-19: Measured Transfer Functions of Flexible Workpiece at Multiple Axial Positions

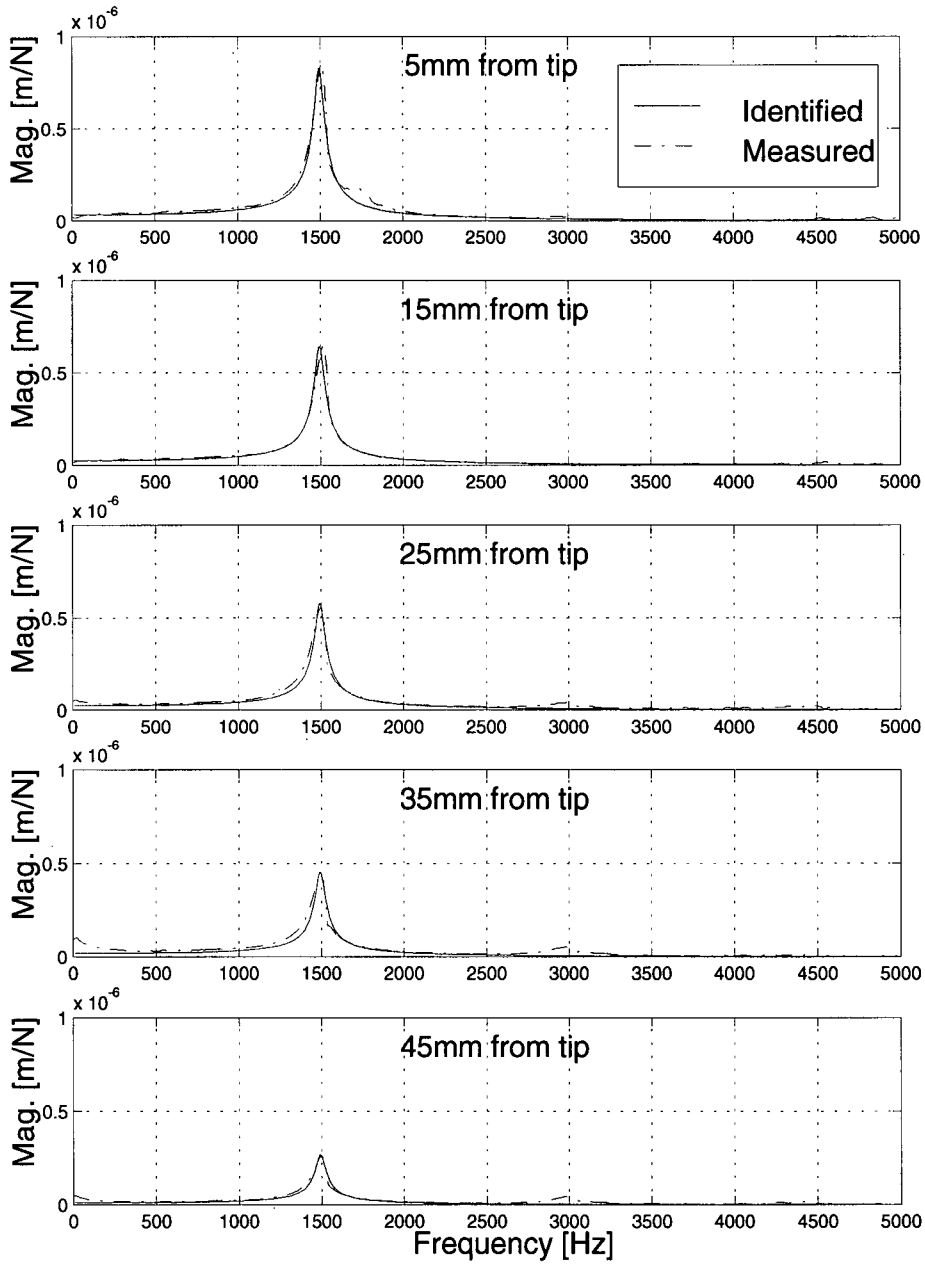

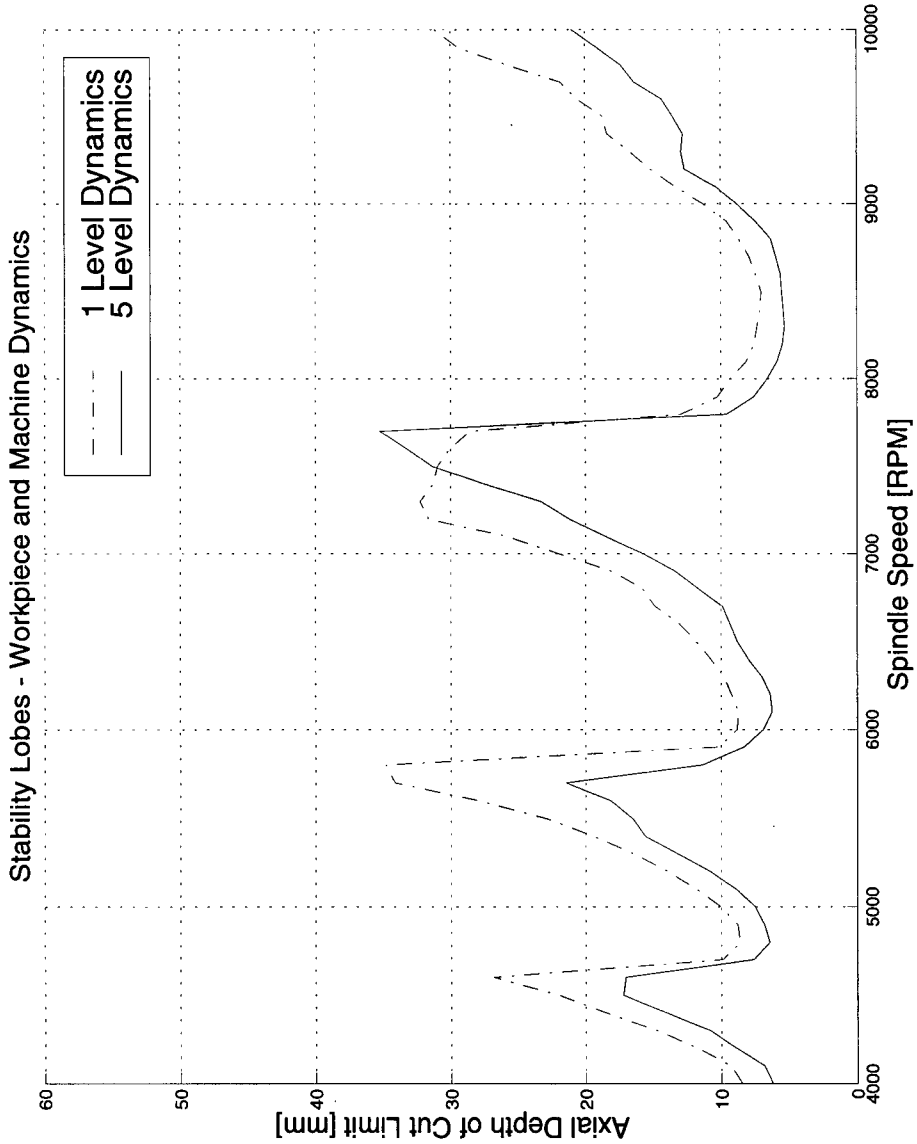

FIGURE 6-20: Stability Lobes: Flexible Machine Tool and Flexible Workpiece - Single and Multiple Level Dynamics

Notice that in this case, the stability limit is actually slightly higher when using a lumped dynamic model. Careful examination of the workpiece and cutter transfer functions would show that at the natural frequency of the spindle, the vibrations of the plate are in phase with the vibrations of the cutter. Hence, at spindle speeds where stability is limited by the spindle modes, the workpiece and cutter vibrate together, reducing their relative motion and decreasing dynamic chip thickness.

The effect of using multiple level dynamics rather than lumped dynamics becomes more evident when the machine tool is assumed to be rigid. The predicted stability lobes of this hypothetical case is shown in Figure (6-21). The increased stability at larger depths of cut is now more noticeable. The simulation limited the axial depth of cut to the length of the cutter of 52.0 mm since the workpiece dynamics are invalid beyond this depth.

6.5.4 Measured and Simulated Vibrations at Multiple Levels

In these cutting tests, the flexible stepped plate workpiece, hydraulic chuck, and endmill cutter described above are used. Since the clamped end of the workpiece is tapered, machining was done along the top-middle of the workpiece to prevent axial forces from create a bending moment not considered in the simulations. Half immersion, downmilling cuts at an axial depth of 1.0 mm were conducted. The feed rate was 0.2mm per tooth. Three separate cuts were performed, moving the laser for each test to measure workpiece vibrations at 5mm, 15mm, and 25mm from the top of the workpiece.

The results of measured and simulated workpiece vibrations are shown in Figures (6-22) through (6-24). The results show fairly good agreement between predicted and experimental vibrations. There is about a 15 percent difference at 5mm and at 15mm from the top of the workpiece. This, again, may be attributed a different cutting speed than that used to calculate cutting force coefficients, and to some measurement errors.

The measurements also shows a large amount of noise, particularly when measuring stiffer points on the workpiece where the resolution of the laser displacement sensor becomes more significant.

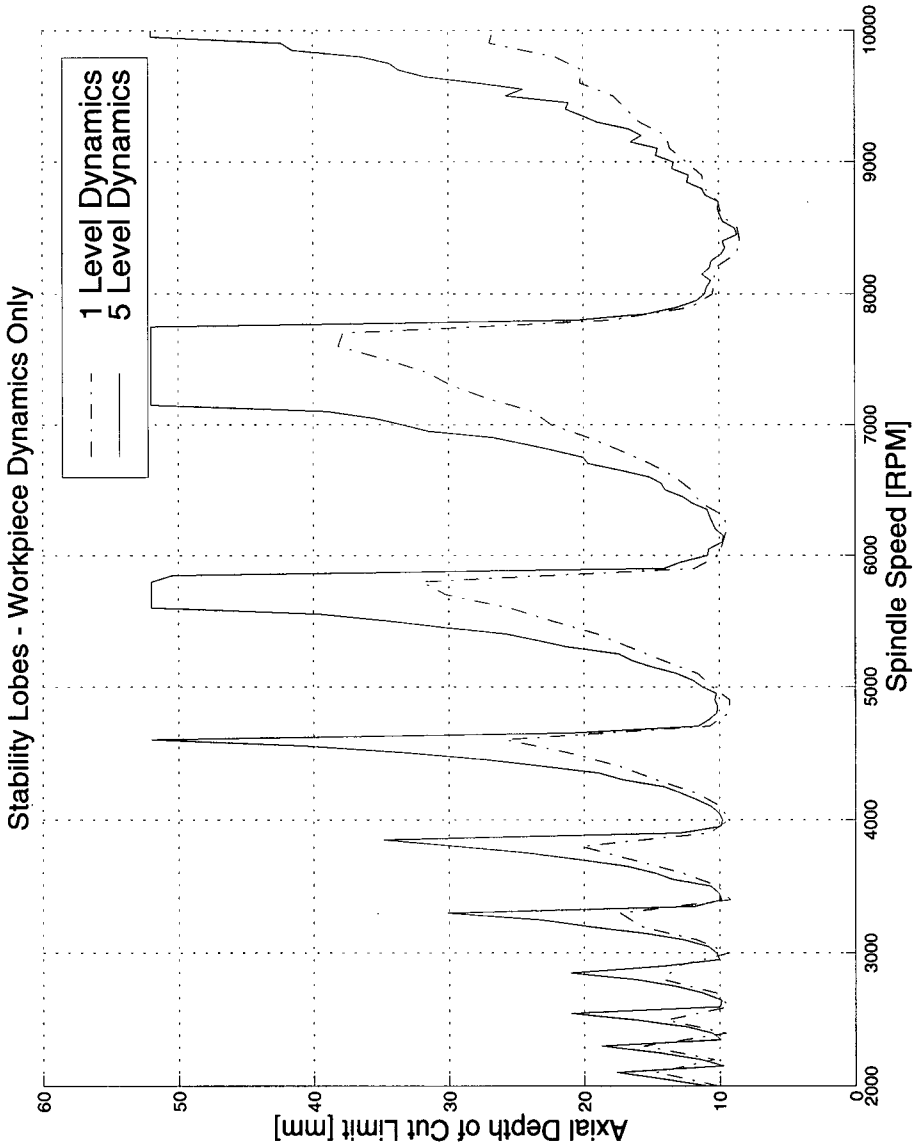

FIGURE 6-21: Stability Lobes: Rigid Machine Tool and Flexible Workpiece - Single and Multiple Level Dynamics

These set of tests are an example of how varying dynamics along the axial depth of cut can be quite significant. Both simulated and experimental results show vibrations decreasing between 30 and 40 percent from 5mm to 15mm from the tip of the workpiece.

FIGURE 6-22: Measured and Simulated Workpiece Vibrations at 5mm from Top of Workpiece

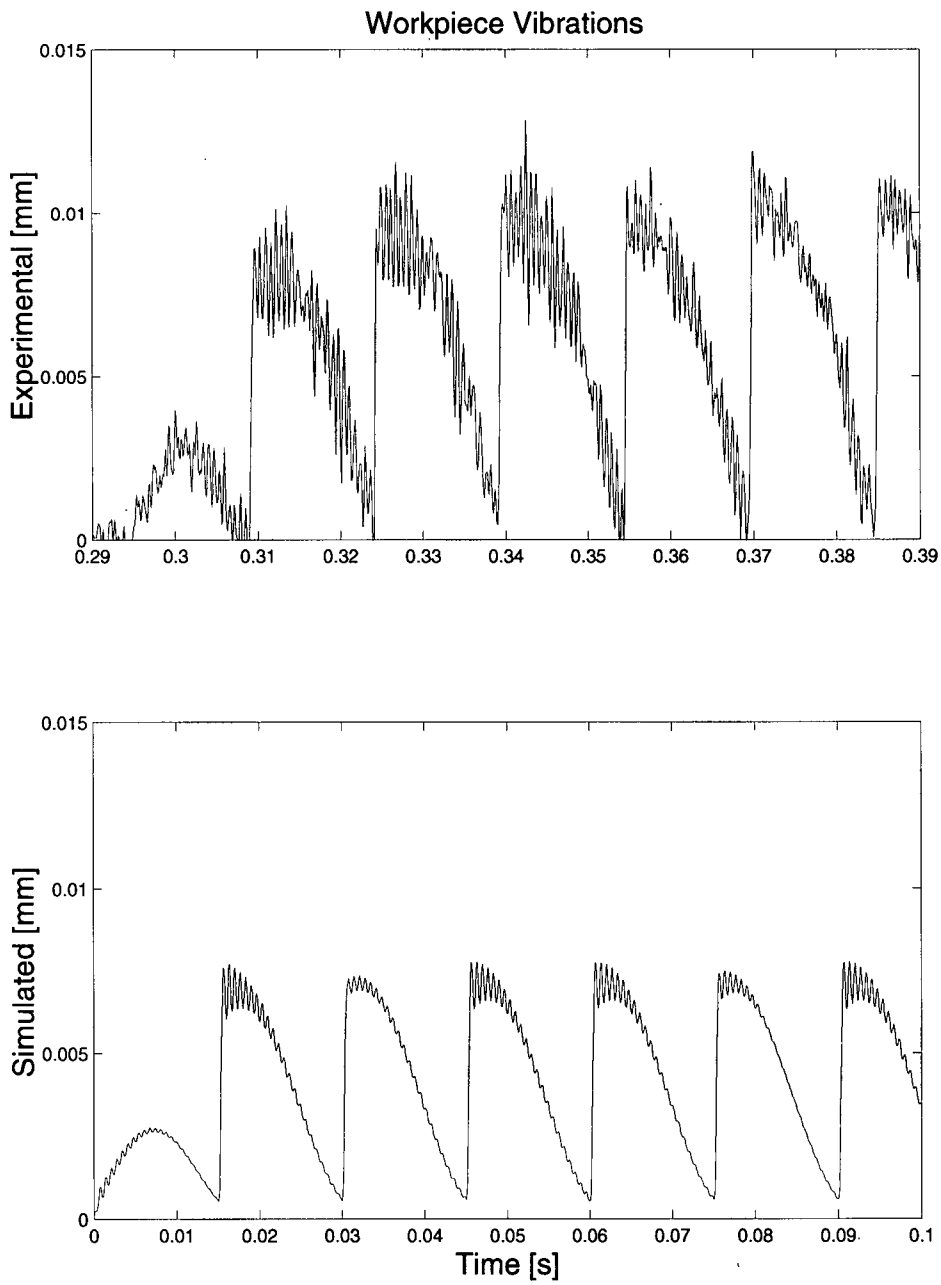

FIGURE 6-23: Measured and Simulated Workpiece Vibrations at 15mm from Top of Workpiece

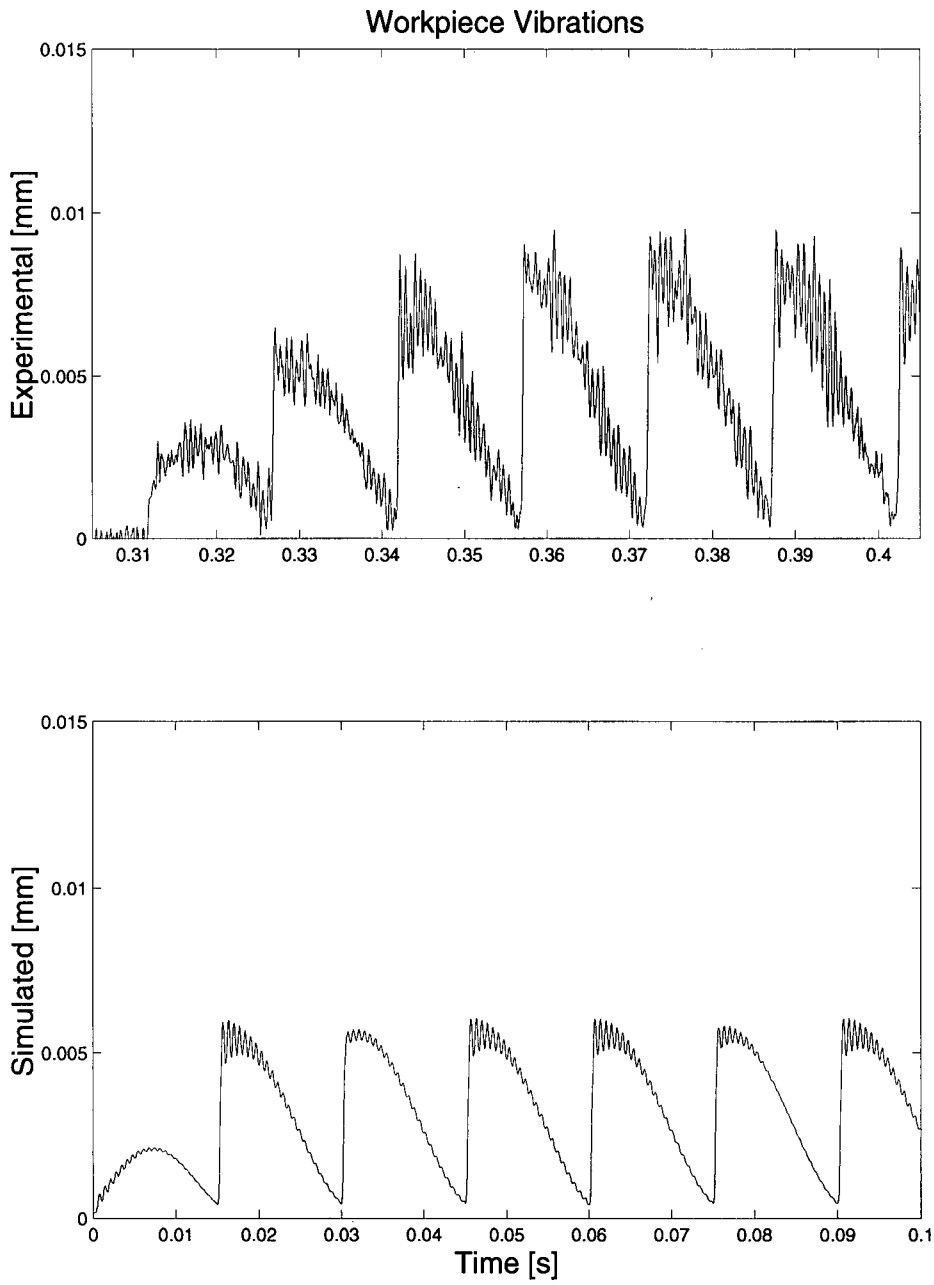

FIGURE 6-24: Measured and Simulated Workpiece Vibrations at 25mm from Top of Workpiece

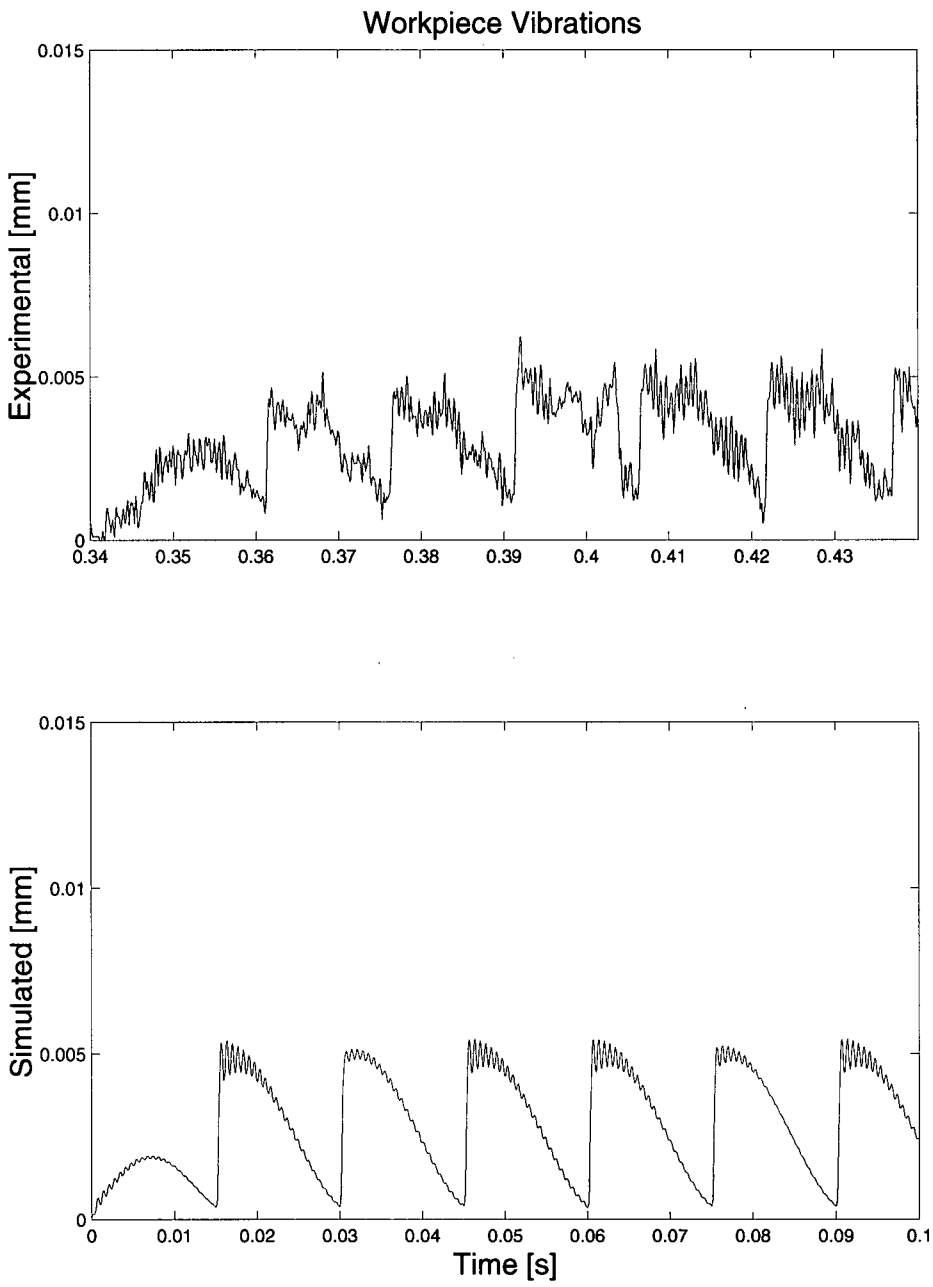

6.6 Summary of results

The experimental cutting tests shown in this chapter demonstrate that the time domain simulation developed in this thesis can be used to predict cutting forces, chatter stability limits, and vibrations with an acceptable degree of accuracy.

Generally, there was good agreement between predicted and measured results. Some discrepancies were noticed, which were most likely due to the force model which was calibrated at only one cutting speed, and difficulty in obtaining accurate measurements during milling, particularly when using sound pressure level to represent vibrations.

CHAPTER 7

Concluding Remarks

The mechanics and dynamics of peripheral milling flexible structures has been studied in this thesis. An improved time domain simulation has been developed to predict cutting forces, vibrations, surface finish, and chatter stability. In creating the model, the main focus was to allow simulation of large depths of cut and consequently very small widths of cut, as commonly encountered in milling flexible plates. Where possible, simulation results have been supported by experimental cutting tests, while other simulation output was verified through a new frequency domain stability lobe model.

The discretized chip thickness model used in the time domain simulation provides improved accuracy, particularly with very small widths of cut and near the workpiece boundaries. The model can also provide a detailed surface finish profile. This exact kinematics of milling approach to modelling chip thickness has allowed accurate prediction of chatter. Furthermore, the resulting stability lobes have demonstrated the affect of feed rate on chatter stability at lower spindle speeds, which has previously been unreported.

To accurately determine stability borders in milling, time domain and frequency domain stability algorithms were created. The new stability criteria used in the time domain simulation relies on uncut dynamic chip thickness. This best reflects chatter conditions, while filtering out most effects of forced vibrations and static deflection. The frequency domain model is

extended from the analytical model used by Budak and Altintas [50]. The newly developed influence of feed rate is added, which has been shown to significantly affect stability at lower spindle speeds in conditions of large feed rate and high frequency chatter vibrations. The stability lobes predicted from time domain simulations support this phenomenon. The time domain stability lobes are also verified through numerous cutting tests, using measured sound pressure level to detect chatter.

A more practical approach was used to model the structural dynamics of the machine tool and of the workpiece, which uses measured transfer functions at various points on the structures. The modal analysis algorithm developed in this thesis uses a two stage lineal least squares identification for each measurement, followed by a global non-linear steepest descent algorithm for optimizing the fit over all measurements. The algorithm has shown to be very effective in accurately identifying modal parameters of cutters and workpieces of arbitrary geometry. The significance of using multiple degrees of freedom along the axial direction when milling at large depths of cut has also been demonstrated. The model can properly model vibrations of long, slender endmills cutters, and very flexible workpieces.

Other results simulated in time domain, such as cutting forces, workpiece and spindle vibrations were also verified through experimental cutting tests. A laser displacement sensor, accelerometers, a force dynamometer, a force impact hammer, and an acoustic microphone were used to measure input and output variables of the milling simulation. Under these carefully controlled conditions, generally, there was good agreement between simulated and measured results. Hence, the simulation can be an extremely useful tool to identifying the optimum cutting conditions for improved productivity, meeting surface error tolerances, and to ensure physical limitations of the machine tool and cutter are not exceeded.

Continued research in this area is recommended in several areas. More complicated cutter geometries should be modelled, such as inserted cutters, which are becoming more common in industry. Vibrations only in the X and Y directions were considered in this thesis. For more than three axis machines, dynamics in the Z direction should also be considered, as well all cross transfer functions. The force model may be improved by including thermal effects, which alter cutting coefficients with changing cutting speed and immersion. The

simulation models can also be integrated to CAD/CAM software for optimizing cutter path. With some modifications, the time domain simulation can be used to test real time chatter detection methods and adaptive control algorithms.

Bibliography

[1] M.E. Martellotti. An Analysis of the Milling Process. Transactions of the ASME, 63:677-700, 1941

[2] M.E. Martellotti. An Analysis of the Milling Process. Part II: Down Milling. *Transactions of the ASME*, 67: 233-251, 1945.

[3] D. Montgomery and Y. Altintas. Mechanisms of Cutting Force and Surface Generation in Dynamic Milling. *Transactions of the ASME Journal of Engineering for Industry,* 115: 245-252, 1993.

[4] P. Lee. Mechanics and Dynamics of Ballend Milling. Master's Thesis, University of British Columbia, 1990.

[5] S. Smith and J. Tlusty. An Overview of Modeling and Simulation of the Milling Process. *Transactions of the ASME Journal of Engineering for Industry,* 113: 169-175.

[6] N. N. Sawin. Theory of Milling Cutters. *Mechanical Engineering,* 48: 1203-1209, 1926

[7] C. Salomon. Die Frasarheit. *Werksttstechnik,* 20: 469-474, 1926.

[8] A. J. P. Sabberwal. Chip Section and Cutting Force During the Milling Operation. *Annals of the CIRP,* 10: 197-203, 1961.

[9] F. Koenigsberger and A. J. P. Sabberwal. An Investigation into the Cutting Force Pulsations During Milling Operations. *International Journal of Machine Tool Design and Research,* 1: 15-33, 1961.

[10] E. J. A. Armarego and C. J. Epp. An Investigation of Zero Helix Peripheral Up-Milling. *International Journal of Machine Tool Design and Research,* 10: 273-291, 1970.

[11] J. Tlusty and P. MacNeil. Dynamics of Cutting Forces in End Milling. *Annals of the CIRP,* 24: 21-25, 1975.

[12] W. A. Kline, R. E. DeVor, and W. J. Zdeblick. A Mechanistic Model for the FOrce System in End Milling with Application to Machining Airframe Structures. *Proc. 8th North American Manufacturing Research Conference,* Dearborn, MI, 1980. Society of Manufacturing Engineers. Vol. XVIII.

[13] W. A. Kline, R. E. DeVor, and J. R. Lindberg. The Prediction of Cutting Forces in End Milling with Application to Cornering Cuts. *International Journal of Machine Tool Design and Research,* 22: 7-22, 1982.

[14] J. W. Sutherland and R. E. DeVor. An Improved Method for Cutting Force and Surface Error Prediction in Flexible End Milling Systems. *Transactions of the ASME Journal of Engineering for Industry,* 108: 269-279, 1986.

[15] E. Budak, Y. Altintas, and E. J. A. Armarego. Prediction of Milling Force Coefficients from orthogonal Cutting Data. *Transactions of the ASME Journal of Engineering Industry,* 118:216-223 1996

[16] S. A. Tobias. *Machine Tool Vibrations.* Blackie and Sons Ltd., 1965.

[17] F. Koenigsberger and J. Tlusty. *Machine Tool Structures - Vol. I: Stability Against Chatter.* Pergamon Press, 1967.

[18] J. Tlusty. Dynamics of High Speed Milling. *Transactions of the ASME Journal of Engineering for Industry,* 108: 59-67, 1986.

[19] S. Smith and J. Tlusty. Update on High Speed Milling Dynamics. *Transactions of the ASME Journal of Engineering for Industry,* 112: 142-149, 1990.

[20] J. Tlusty and F. Ismail. Basic Nonlinearity in Machining Chatter. *Annals of the CIRP,* 30: 21-25, 1981.

[21] Y. Kondo, O. Kawano, and H. Sato. Behavior of Self-Excited Chatter Due to Multiple Regenerative Effect. *Transactions of the ASME Journal of Engineering for Industry,* 103: 324-329, 1981.

[22] J. Slavicek. The Effect of Irregular Tooth Pitch on Stability of Milling. *Proceedings of the 6th Machine Tool Design and Research* Conference*: 15-23.* Pergamon Press, London, 1965.

[23] H Opitz, E. U. Dregger, and H. Roese. Improvement of the Dynamic Stability of the Milling Process by Irregular Tooth Pitch. *Proceedings of the 7th Machine Tool Design and Research Conference,* 9: 213-227, 1966.

[24] P. Vanherck. Increasing Milling Machine Productivity by Use of Cutters with Non-Constant Cutting-Edge Pitch. *Proc. Adv. Machine Tool Design and Research Conference, 8: 947-960, 1967.*

[25] J. P. Gurney. A General Analysis of Two Degree-of-Freedom Instability in Machine tools. *Journal of Mechanical Engineering Science, Vol. 4,* 1962.

[26] J. Tlusty. A Method of Analysis of Machine Tool Stability. *Proceedings of the 6th Machine tool Design and Research Conference, pp*5-14, 1965.

[27] F. Ismail and A. Bastami. Improving Stability of Slender End MIlls Against Chatter. *Transactions of the ASME Journal of Engineering for Industry,* pp1-5, 1986.

[28] F. Ismail and V. R. Vadari. Machining Chatter of End Mills With Unequal Modes. *Transactions of the ASME Journal of Engineering for Industry,* 112: 229-235, 1990.

[29] T. R. Sisson and R. L. Kegg. An Explanation of Low Speed Chatter Effects. *Transactions of the ASME Journal of Engineering for Industry,* 91: 951-955, 1969.

[30] J. Tlusty. Analysis of the State of Research in Cutting Dynamics. *Annals of the CIRP,* 27: 583-589, 1978.

[31] J. Tlusty. High-Speed Machining. *Annals of the CIRP,* 42: 733-738, 1993.

[32] D. Montgomery. Milling of Flexible Structures. Master's Thesis, University of British Columbia, 1990.

[33] M. K. Das and S. A. Tobias. The Relation Between the Static and the Dynamic Cutting of Metals. *Machine Tool Design and Research*, 7: 63-89, 1967.

[34] P. W. Wallace and C. Andrew. Machining Forces: Some Effects of removing a Wavy Surface. *Journal of Mechanical Engineering Science*, 8: 129, 1966.

[35] H. Van Brussel and P. Vanherck. A New Method for the Determination of the Dynamic Cutting Coefficient. *Proceedings of the 12th Machine tool Design and Research Conference,* pp129-136, 1971.

[36] D. W. Wu. A New Approach for Formulating the Transfer Function for Dynamic Cutting Process. *Transactions of the ASME Journal of Engineering for Industry,* 111: 37-47, 1989.

[37] M. A. Elbestawi, F. Ismail, R. Du, and B. C. Ullagaddi. Modelling Machine Dynamics Including Damping in the Tool-Workpiece Interface. *Transactions of the ASME Journal of Engineering for Industry*, 116: 435-439, 1994.

[38] J. Tlusty and M. Polacek. The Stability of Machine Tools Against Self Excited Vibrations in Machining. *International Research in Production Engineering, ASME*, pp465-474, 1963.

[39] S. A. Tobias and W. Fishwick. A Theory of Regenerative Chatter. *The Engineer*, London, 1958.

[40] H. E. Merritt. Theory of Self-Excited Machine-Tool Chatter: Contribution to Machine-Tool Chatter Research Part 1. *Transactions of the ASME Journal of Engineering for Industry*, pp447-454, 1965.

[41] R. Sridhar, R. E. Hohn, and G. W. Long. A General Formulation of the Milling Process Equation: Contribution to Machine Tool Chatter Research Part 5. *Transactions of the ASME Journal of Engineering for Industry*, pp317-324, 1968.

[42] R. E. Hohn, R. Sridhar, and G. W. Long. A Stability Algorithm for a Special Case of the Milling Process: Contribution to Machine Tool Chatter Research Part 6. *Transactions of the ASME Journal of Engineering for Industry*, pp325-329, 1968.

[43] R. Sridhar, R. E. Hohn, and G. W. Long. A Stability Algorithm for the General Milling Process: Contribution to Machine Tool Chatter Research Part 7. *Transactions of the ASME Journal of Engineering for Industry*, pp330-334, 1968.

[44] H. Opitz and F. Bernardi. Investigation and Calculation of the Chatter Behaviour of Lathes and Milling Machines. *Annals of the CIRP*, 18: 335-343, 1970.

[45] S. Smith and J. Tlusty. Efficient Simulation Programs for Chatter in Milling. *Annals of the CIRP*, 42: 463-466, 1993.

[46] M. Weck, Y. Altintas, and C. Beer. CAD Assisted Chatter-Free NC Tool Path Generation in Milling. *International Journal of Machine Tools Manufacturing*, 34: 879-891, 1994.

[47] I. Minins, R. Yanushevsky, and A. Tembo. Analysis of Linear and Nonlinear Chatter in Milling. *Annals of the CIRP*, 39: 459-462, 1990.

[48] I. Minis and R. Yanushevsky. A New Theoretical Approach for the Prediction of Machine Tool Chatter in Milling. *Transactions of the ASME Journal of Engineering for Industry*, 115:1-8, 1993.

[49] Y. Altintas and E. Budak. Analytical Prediction of Stability Lobes in Milling. *Annals of the CIRP*, 44: 357-362, 1995.

[50] E. Budak and Y. Altintas. Analytical Prediction of Chatter Stability in Milling: Part I: General Formulation. *Proceedings of the ASME Dynamics and Controls Division*, 57: 545-556, 1995.

[51] E. Budak and Y. Altintas. Analytical Prediction of Chatter Stability in Milling: Part II: Application of the General Formulation to Common Milling Systems. *Proceedings of the ASME Dynamics and Controls Division*, 57: 557-565, 1995.

[52] W. A. Kline, R. E. DeVor, and I. A. Shareef. The Prediction of Surface Accuracy in End Milling. *Transactions of the ASME Journal of Engineering for Industry*, 104: 272-278, 1982.

[53] W. A. Kline and R. E. DeVor. The Effect of Runout on Cutting Geometry and Forces in End Milling. *International Journal of Machine Tool Design and Research*, 23: 123-140, 1983.

[54] M. A. Elbestawi and R. Sagherian. Dynamic Modeling for the Prediction of Surface Errors in Milling of thin-Walled Sections. *Journal of Materials Processing Technology*, 25: 215-228, 1991.

[55] R. Sagherian and M. A. Elbestawi. A Simulation System for Improving Machining Accuracy in Milling. *Computers in Industry*, 14: 293-305, 1990.

[56] E. Balmes. Frequency Domain Identification of Structural Dynamics Using Pole/Residue Parameterization. *Proceedings of the 14th International Modal Analysis Conference,* pp540-546, 1996.

[57] R. J. Allemang and D. L. Brown. A Review of Modal Parameter Estimation Concepts. Modal Analysis - Short Course Notes, Department of Mechanical and Industrial Engineering, University of Cincinati, Cincinati, Ohio, 1980.

[58] U. Fullekrug. Survey of Parameter Estimation Methods in Experimental Modal Analysis. *International Modal Analysis Conference*, 1987.

[59] R. J. Allemang and D. L. Brown. Multiple-Input Experimental Modal Analysis - A Survey. International Journal of Analytical and Experimental Modal Analysis, 1:37-44, 1986.

[60] Pandit and M. Sudhakar. Modal and spectrum analysis: data dependent systems in state space. New York, Wiley, 1991.

[61] J. S. Arora. Introduction to Optimum Design. *McGraw Hill Book Co.*, New York, 1986.

[62] R. Jones and Y. Kobayashi. Global Parameter Estimation Using Rational Fraction Polynomials. *Proceedings of 4th International Modal Analysis Conference*, pp864-869, 1986.

[63] K. Ogata. Modern Control Engineering, Third Edition. *Prentice-Hall, Inc.*, London, 1997.

[64] W. H. Press et al. Numerical Recipes in C: The Art of Scientific Computing. *Cambridge University Press*, Cambridge, 1988.

[65] S. C. Charpa and R. P. Canale. Numerical Methods for Engineers, Second Edition. *McGraw-Hill, Inc.* New York, 1988.